UNIVERSITY OF POTSDAM
Institute of Physics and Astronomy
APPLIED CONDENSED MATTER PHYSICS

P H D – T H E S I S

Scattering Effects in the Sound Wave Propagation of Instrument Soundboards

Presented by
Marcel KAPPEL

Thesis Supervisor: Prof. Dr.-Ing. Reimund GERHARD

Second Supervisor: Prof. Dr. rer. nat. Markus ABEL

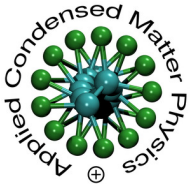

Published online at the
Institutional Repository of the University of Potsdam:
URL http://opus.kobv.de/ubp/volltexte/2012/6267/
URN urn:nbn:de:kobv:517-opus-62676
http://nbn-resolving.de/urn:nbn:de:kobv:517-opus-62676

Die Normalität ist eine gepflasterte Straße;
man kann gut darauf laufen,
doch es wachsen keine Blumen auf ihr.

(Vincent van Gogh)

Acknowledgments

Firstly, I would like to express my thanks to everyone who supported me during my PhD time.

Most of all I want to thank my supervisor Prof. Dr. Reimund Gerhard for the great opportunity to write my PhD thesis at the Applied Condensed-Matter Physics (ACMP) group and all the support he gave me during my work. Also I want to thank my advisor Prof. Dr. Markus Abel as he always took the time for me, even if he had no time due to his various other duties.
I am truly indebted to the piano manufacturer 'C. Bechstein Pianofortefabrik' for the opportunity to perfom measurements on one of their upright pianos. In particular, I would like to give special thanks to Werner Albrecht, for giving me a lot of his attention and time during these measurements.
I also thank Michael Winkler and Jost Fischer for the good teamwork regarding the Schuke project.
Many thanks to the people from the ACMP, who increased my understanding, by valuable talks and discussions during the last three years, not only in polymer physics but also in acoustics. In particular, I thank Gunnar, René, Matthias, Lars, Werner, Alex and Peter for all the great support they gave me and I apologize for the time they spent with me to discuss various problems. Also many thanks to Steffen, Marc, Mareike, Daniel, André, Peter, Lena, Sebastian, Alena, Nika for enriching my life with their friendship. My deepest thanks and respect go to Matthias and Andreas who have been good friends all the time at the university.

Finally, I want to thank and acknowledge my parents and my brother for their support by any means. Without their help I would not have been where I am now.

... many, many thanks to Konstanze for everything ...

Abstract

In the western hemisphere, the piano is one of the most important instruments. While its evolution lasted for more than three centuries, and the most important physical aspects have already been investigated, some parts in the characterization of the piano remain not well understood. Considering the pivotal piano soundboard, the effect of ribs mounted on the board exerted on the sound radiation and propagation in particular, is mostly neglegted in the literature. The present investigation deals exactly with the sound wave propagation effects that emerge in the presence of an array of equally-distant mounted ribs at a soundboard. Solid-state theory [Ziman 1972, Ashcroft 1976] proposes particular eigenmodes and -frequencies for such arrangements, which are comparable to single units in a crystal. Following this 'linear chain model' (LCM), differences in the frequency spectrum are observable as a distinct band structure. Also, the amplitudes of the modes are changed, due to differences of the damping factor.

These scattering effects were not only investigated for a well-understood conceptional rectangular soundboard (multichord), but also for a genuine piano resonance board manufactured by the piano maker company 'C. Bechstein Pianofortefabrik'. To obtain the possibility to distinguish between the characterizing spectra both with and without mounted ribs, the typical assembly plan for the Bechstein instrument was specially customized. Spectral similarities and differences between both boards are found in terms of damping and tone.

Furthermore, specially prepared minimal-invasive piezoelectric polymer sensors made from polyvinylidene fluoride (PVDF) [Kappel 2011] were used to record solid-state vibrations of the investigated system. The essential calibration and characterization of these polymer sensors was performed by determining the electromechanical conversion, which is represented by the piezoelectric coefficient d_{33}. Therefore, the robust 'sinusoidally varying external force' method [Altafim 2009, Kressmann 2001] was applied, where a dynamic force perpendicular to the sensor's surface, generates movable charge charriers. Crucial parameters were monitored, with the frequency response function as the most important one for acousticians.

Along with conventional condenser microphones, the sound was measured as solid-state vibration as well as airborne wave. On this basis, statements can be made about emergence, propagation, and also the overall radiation

of the generated modes of the vibrating system. Ultimately, these results acoustically characterize the entire system.

Deutsche Zusammenfassung

Betrachtet man den westlichen Kulturkreis, ist der Flügel bzw. das Klavier wohl eines der bedeutendsten Instrumente. Trotz einer stetigen, empirischen Weiterentwicklung dieses Instrumentes in den letzten drei Jahrhunderten und des Wissens um die wichtigsten physikalischen Effekte, sind viele Teile der Charakterisierung des Klaviers (sowohl akustisch als auch physikalisch) immer noch nicht vollständig verstanden. Nehmen wir nur den Resonanzboden – *das* entscheidende Bauteil für die Akustik eines Klaviers – und betrachten die Auswirkung, den die Berippung auf die Schallausbreitung des Instruments hat. Bis auf wenige Ausnahmen ([Wogram 1980, Giordano 1997]) wird dieser Struktur-Aspekt in der Literatur weitestgehend übergangen. Die vorliegende Arbeit untersucht genau diese Ausbreitungscharakteristiken und Streueffekte, welche dadurch entstehen, dass Rippen, die denselben Abstand zueinander haben, auf dem Resonanzboden angebracht werden. Die Festkörperphysik stellt ein einfaches Modell ([Ziman 1972, Ashcroft 1976]) über die Eigenfrequenzen für solche Anordnungen bereit. Dafür werden die Rippen und deren Abstände wie Einheitszellen eines Kristalls betrachtet. Ausgehend vom sogenannten 'Modell der linearen Ketten', werden gemessene Frequenzbänder im Spektrum erklärbar. Zusätzlich ändern sich auch die spektralen Amplituden des Resonanzbodens durch das Anbringen der Rippen.

Diese Streueffekte wurden nicht nur an einem konzeptionellen rechteckigen Resonanzboden untersucht, sondern auch an einem originalen Klavier-Resonanzboden, welcher von dem Klavierbauer 'C. Bechstein Pianofortefabrik' hergestellt wurde und auch später in einem fertigen Klavier zum Einsatz kommen wird. Der traditionelle Zusammenbau des Klaviers wurde speziell für diese Untersuchung abgeändert, um die Möglichkeit zu haben, die Berippung des Resonanzbodens spektral zu charakterisieren. Alle gefundenen Eigenschaften des konzeptionellen und des originalen Bodens wurden verglichen. Für die Dämpfung und für die Brillianz des Tons wurden Übereinstimmungen, aber auch Unterschiede gefunden.

Ein großer Teil dieser Untersuchung erforderte den Einsatz von speziell angefertigten piezoelektrischen Polymer-Beschleunigungsaufnehmern aus Polyvinylidenfluorid [Kawai 1969]. Direkt fest eingeklebt im Instrument, wurden diese eingesetzt, um die Körperschwingungen des vibrierenden Systems aufzunehmen [Kappel 2011]. Die essentielle Kalibrierung und Charakterisierung dieser Sensoren wurde durchgeführt,

indem die elektromechanische Umwandlung bestimmt wurde, die durch den piezoelektrischen Koeffizienten d_{33} gegeben ist. Durch eine sinusförmig variierende, externe Kraft und die dadurch entstehenden Ladungsträger an den Oberflächen des Sensormaterials kann d_{33} sehr genau bestimmt werden. In Abhängigkeit entscheidender physikalischer Größen, z.B. der Frequenz-Antwort-Funktion, wurde das Verhalten des piezoelektrischen Koeffizienten untersucht.

Die erzeugten Vibrationen als Körperschall (aufgenommen durch die Piezopolymere) und als Luftschallwelle (aufgenommen durch konventionelle Kondensator-Mikrophone) wurden simultan gemessen und dann untersucht. Daraus kann man Aussagen über Entstehung, Ausbreitung und Abstrahlung der erzeugten Moden in das umgebende Medium ableiten. Letztlich charakterisieren diese Ergebnisse das gesamte vibrierende System akustisch.

Contents

Chapter 1
Introduction

'Gravicembalo col piano e forte', translated from Italian as 'soft and loud harpsichord', is the original name of the piano, which is one of the most relevant western instruments today [Fletcher 1993]. Its functioning and characteristics were investigated and theoretically understood to a reasonable level. However, tonal differences between manufacturers and even between same types exist [Conklin Jr. 1996c], which are hard to explain. Regarding the physical aspects of the instrument, many details and effects remain poorly understood. From the perspective of sound wave radiation, the most delicate part of the instrument is certainly its 'loudspeaker' – the resonance board or rather the soundboard[1] [Wogram 1980, Giordano 1997]. But why is it necessary to include such a board, when there are already vibrating piano strings? The strings are not able to radiate a loud airborne sound wave directly by themselves. A larger object – the soundboard – is needed for an efficient sound radiation. The vibrational energy generated by the strings is transferred through the piano bridge into the soundboard, which is, compared to piano strings, much more efficient in the airborne sound radiation[2] [Suzuki 1986, Giordano 1998a, Conklin Jr. 1990].

Apart from pianos, the sound radiation of surfaces and the sound wave propagation within a material are important to a wider class of instruments. They are also among the most important research issues considering the acoustics, because almost every stringed instrument follows the same process in the generation of a sound tone. The string vibrations are transmitted through a bridge to a vibrational amplification structure. Ever since the inauguration of stringed instruments, uncountable modifications from instrument makers evolved these radiation bodies to the very special forms that we know today. There are basically two amplification principles: either the radiation structure exhibits a particulary complicated setup where the whole instrument is part of the amplification surface, which is the case for violins and guitars [Bissinger 2008, Gren 2006]. Or only few parts of the

[1] Both terms will be used as synonyms throughout this study.

[2] Due to the high difference between the mass of the strings and the soundboard, which is marked by a large mismatch of their respective impedances, the vibration is 'trapped' within the string and is slowly leaking into the soundboard [Wogram 1980]. In detail, this will be explained later.

instrument will contribute to that, which is the case for pianos. Considering the latter type, a specially shaped and flat resonance board amplifies the string vibrations. In most cases, ribs are attached to the instrument soundboard. The ribs of the piano construction will have a dual function. On the one hand, they enhance the mechanical stability of the soundboard. On the other hand, they prestress the board and thus act as an energy reservoir ready to release. Although some studies on the ribs and their radiation effects have been carried out in the past (e.g. [Wogram 1980, Giordano 1997]), the physical impact of this specific mechanical construction on sound radiation and propagation has mainly been neglected in the literature.

The present investigation deals with these soundboards, their spectral radiation, and the propagation of the generated sound waves. In particular, the scattering effects originating from the ribs are studied. It is well-known that regular arrays of scattering obstacles, which are comparable to single units in a crystal, result in a band structure in the frequency spectrum (see section 2.1.4). Solid state theory [Ziman 1972, Ashcroft 1976] proposes eigenmodes and -frequencies for such arrangements. Actually only having coupled ocillators will also yield these band structures [Goldstein 1980]. The individual scatterers for the soundboard construction are the ribs and the board itself, featuring different cross sections (due to the ribs and other mountings), will represent the soundwave path. Given the scattering characteristics of the soundboard (or crystal), the 'passing' frequencies will arrange each other in a recognizable band structure in the frequency spectrum.

But investigation of these special effects is difficult, when the particularly shaped resonance board of a piano is considered: the emerging eigenmodes heavily depend on the specific shape. Nevertheless, a theoretical configuration of a surface structured with ribs in a regular array, can be mapped to the real soundboard. Under mild restrictions, the frequency spectrum between theory and experiment will be similar. Consequently, it was decided to additionally build rectangular conceptual soundboard [Kappel 2010] as a dedicated setup, which topologically mimicks a piano soundboard. It is easily understood, cheap, and well controllable. The impact of the mounted ribs on the radiated spectrum of a multichord (chapter 4) *and* on a real piano soundboard manufactured by Bechstein (chapter 5) is systematically studied. Regarding the measurements on the real Bechstein soundboard, the traditional assembly sequence of the piano was customized[3]. Similarities and differences between both boards (multichord and Bechstein soundboard) will be represented in

[3]Usually, the bridge and the ribs of the piano are mounted onto the soundboard at once. In order to distinguish between the characteristic spectra both with and without mounted ribs, this step was subdivided.

terms of damping and tone.

At this point, the question arises, what is the best way to measure the sound wave propagation and the scattering effects? To distinguish between radiated airborne sound and sound waves propagated inside the board, piezoelectric accelerometers were used throughout this investigation. These specially prepared solid-state vibrational sensors represent a class of innovative and minimal-invasive recording sensors, which are also highly flexible and relatively inexpensive. The complete preparation and the characterization process of these measurement devices are documented and discussed (see Sec. 3.2 and [Kappel 2011]). Under external force, the calibration of the polymer relaxation was of major concern over short and long term scales. The main procedure utilized for the probe characterization and calibration is the determination of the piezoelectric coefficient d_{33} as described by [Altafim 2009, Kressmann 2001] and also in Sec. 3.2. From the perspective of vibrational measurements, the most important parameters from the *inside* of a setup were monitored, namely the static force, the amplitude of the dynamic force, the frequency response, and the long-term stability. Moreover, it will be shown in this study that it is possible to compensate these effects of the parameter drift resulting from external stress.

Additionally, a new acoustic recording procedure will be presented. It is a result of the combination of measurements of solid-state vibrations (piezoelectric polymer) and radiated airborne sound (conventional condenser microphones). Both data acquisitions will be performed simultaneously. This procedure can be recommended as an optimal method for investigation of the temporal distribution of vibrational energy in a system to be measured.

The presented thesis consists of three main parts:

- The detailed description of the piano tone generating mechanism as well as the commonly used theory of piano physics is summarized in the first chapter. Furthermore, the 'linear chain model' (LCM), a 'mass-spring' scattering model, is provided from the solid state physics explaining the rib influence on sound wave propagation.

- In the second chapter the measurements of the room characteristics of the recording room in which the multichord measurements had taken place are provided. Also, the detailed preparation, calibration, and characterization of the piezoelectric polymer devices are given here.

- The main part of the study will be presented in chapters 4 and 5, which finally explain the investigations performed at the conceptual soundboard and the Bechstein upright piano 'Z.3/116' soundboard.

The obtained results, spectral differences and similarities as well as the comparison to the LCM are presented and discussed in these chapters.

The thesis concludes with the summary and outlook.

Chapter 2

Background

In section 2.1 the piano evolution, the mechanical sequence of the tone generation and the underlying physics are introduced. Different piano manufacturers produce different instruments, which can result in missing brilliance or increased sound radiation for certain frequencies. These differences may be attributed to the geometry and restrictions in the construction of the soundboard which acts as the last acoustical filter before the sound is radiated towards the audience listening. Because it is one of the major investigation part of the thesis, the role of the soundboard and the ribs for the sound wave propagation of the piano is highlighted in particular. A model (see Sec. 2.1.4) proposed by solid-state-physics, the 'linear chain model' (LCM), can be applied for the frequency radiation and propagation pattern of the soundboard, dependent on the mounted ribs of the resonance board.

Since it is used as sensor material throughout this investigation, the second part of this chapter describes the morphology and related material properties of polyvinylindene fluoride (PVDF). For the understanding of the piezoelectricity of PVDF it is important to distinguish between the different crystal phases and the amorphous phase, because they directly affect pivotal parameters of the material. Knowing that, the piezoelectric coefficient perpendicular to the surface of the polymer material and the stability are investigated.

2.1 The Piano

2.1.1 Short History of Evolution

The evolution of the piano (see Fig. 2.1 for the two common types nowadays) originates back to the beginning of the 18th century. 1709 is commonly accepted as the pianos' year of birth as Bartolomeo Cristofori [Pollens 1995, Parakilas 1999], an italian instrument maker, was able to construct a hammer action, which initially enables the piano making. The advantage of the hammer technique compared to the existing harpsichord mechanism was represented by the sensitivity of the momentum amplitude given to the piano keys. Independent of the way one excites the harpsichord keys, the string will

Figure 2.1: The two common piano types nowadays: the upright (*left*: Zimmermann Z1/125) and the grand piano (*right*: C. Bechstein D 282 concert grand piano). (Pictures by courtesy of C. Bechstein Berlin).

be plucked with the same initial displacement, resulting in the same sound volume for every played tone. Contrary to that, pianos are able to vary the tone volume with the speed of the striking hammer by the modulation of the key excitation. The new Cristofori invention was the prototype of a grand piano, but it takes many intermediate steps and almost two additional centuries until the grand piano received the form we know today. Some decades after the development of the Cristofori piano another construction alternative was evolved – the first satisfactory upright pianos were introduced around 1800. This compact form had the advantage, that the strings ran vertical to the floor and therefore the utility space was reduced to a minimum compared to the broad design of a grand piano. The two types common in our days are displayed in Fig. 2.1, with an upright piano on the left (Bechstein 'Z1/125') and a grand piano on the right (Bechstein 'D 282'). One important step in the evolution of the piano affecting the stability of the tone frequency was the introduction of the full cast iron plate, which was able to withstand higher tension of the strings over longer time. In this way, the big problem of the tuning stability of the strings in early wood constructions was reduced to a minimum [Conklin Jr. 1996c].

A typical modern grand piano (and also an upright piano) covers more than seven octaves and comprises 88 keys (from A0 = 27.5Hz to C8 = 4186Hz)[1], comparing to about 4 and a half octaves and 54 keys (C2 = 65.4Hz to C6 = 1046.5Hz) for the Cristofori piano [Conklin Jr. 1996a]. Also the sound of the Cristofori piano differs significantly from the modern instrument, having a timbre, which is closer to the harpsicord than a grand piano [Conklin Jr. 1996c]. Generally, a piano tone can be described to some extent by its spectrum, comprising the frequencies of the fundamental string

[1] There are special piano types, which have more than the common 88 keys. For example, extended-range pianos with 102 keys (tonal range from C0 to F8) are manufactured more recently. But also lightweight upright acoustical pianos with less than 88 keys are produced these days.

vibration and its respective harmonics and their amplitudes (see A.2.3 for the governing equations of the Fourier Transform). The specific relations between the harmonic amplitudes and their decay behavior is important for the special perception of the piano tone.

2.1.2 General Functioning

The functioning of the piano and the physics behind it [Fletcher 1993] are tightly correlated and always need to be explained side by side.

The birth of the piano is commonly accepted with the construction of the Cristofori piano as already mentioned earlier in this chapter. But the beginning of the investigation of the piano acoustics goes back to the second part of the 19th century with the scientific studies of Hermann von Helmholtz (1821 – 1894). At this time the overall piano evolution was mainly finished, except for details concerning the tonal perception[2]. Based on his hearing impressions and the usage of so-called Helmholtz resonators[3], he contributed significantly to the understanding of the tonal characteristics of musical instruments and he was able to develop theoretical studies, for example the interaction between the hammer and the strings of the piano [v. Helmholtz 1863]. Follow-up studies were made around the beginning and middle of the 20th century about further individual aspects of the tone generation and its physics [Schuck 1943].

To generate a piano tone, a sequence of individual steps needs to be carried out successively [Fletcher 1993, Conklin Jr. 1990] (schematic view of a piano is shown in Fig. 2.2): The initial step is pressing down one of the piano keys. Since it is pressed, the string damper is raised and a hammer is directly accelerated to the string [Askenfelt 1993, Hall 1992a, Chaigne 1994b]. When it is thrown against the string [Suzuki 1987], a large amount of force in a short time is transferred to excite the string by that single pulse. That means, the delivery of momentum from the hammer to the strings initializes the chain of processes, which is needed for the generation of a piano tone. Not to interfere with the vibration, the hammer quickly departs from the string and if the piano player wants to end the tone, he simply releases the key to drop the damper against the string again, stopping the vibration and the respective radiation. Striking the key harder (i.e. increasing the force) over the same time, the momentum and the vibration amplitude will increase. On the other hand, a softer key excitation will result in a lower momentum and therefore a smaller amplitude of the string vibration. Because of that, the piano tone

[2] [Conklin Jr. 1996b] investigated tonal differences of historic and present soundboards.

[3] With Helmholtz resonators one can investigate spectral fractions of a tone [v. Helmholtz 1863].

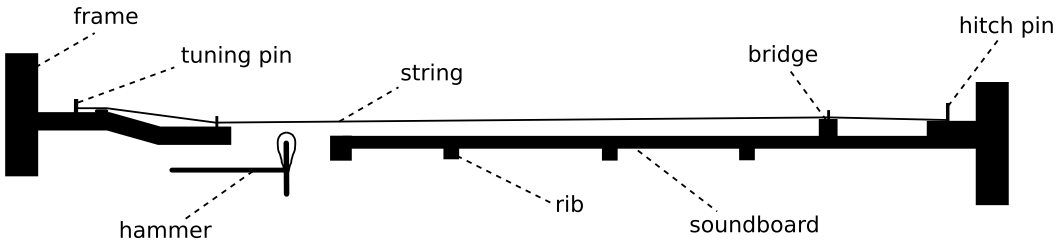

Figure 2.2: Cross Section of a Piano with its most important parts for the sound generation [Conklin Jr. 1990].

becomes minor and softer [Suzuki 2007]. The loudest acoustic output of a piano in units of power P is in the order of $P = 0.1$W, which seems to be relatively small, but is nevertheless the most of all compared to the majority of all stringed instruments.

Depending on the frequency, a certain number of strings with (almost) the same tuning contribute to one tone [Weinreich 1977, Fletcher 1993]. These strings are hit by the same felt hammer. The higher the fundamental frequency of the piano tone, the higher the number of excited strings; ranging from one string for the low pitched sound, over two strings for the middle range to three strings for the high pitch range. As indicated above, the strings for the same tone are slightly detuned in order to extend the tone decay [Weinreich 1977]. Once the momentum is transfered, the strings begin to couple their vibrations using the bridge for the connection. The gentle tone generated by the string has to be magnified, because it is just uneffective concerning the sound radiation. When the string is actually excited, the vibration is transfered from the string via the piano bridge to the resonance board, which is a more efficient radiator of sound and acts as a loudspeaker for the string vibrations [Conklin Jr. 1996b, Giordano 1996, Giordano 1998b]. But during this process, another problem occurs: there is a significant difference in the mechanical impedance[4] between the string and the soundboard [Giordano 1998a]. From the perspective of the string, the soundboard is just to heavy to be moved – the string vibrations are repeatedly reflected at the bridge and they are slowly leaking into the soundboard. But this mismatch can be reduced by increasing the weight or the tension of the strings [Conklin Jr. 1996d], which is practically being done by the common copper wrapping of the steel core strings (increasing the weight) and also by the above mentioned 'multiple stringing' per tone (increasing the tension). With these design modifications the transfer of the vibrations towards the resonance board becomes more efficient.

[4]The mechanical impedance describes the level of motional resistance of an object exposed to an external force (see A.2.9.1).

The sound radiation and the characteristics of a vibrating resonance board, which is one of the main parts of this investigation, is described in [Moore 2006, Conklin Jr. 1996b, Giordano 1998a, Suzuki 1986, Wogram 1980, Bork 1993, Giordano 2006] and will be he highlighted in the next section.

Another important aspect and a further longstanding goal in the piano physics was the development of theoretical models, which are able to compute the sound characteristics or even mimicking the radiation. These models typically cover single individual steps in the tone generation sequence: the hammer motion [Hayashi 1999], the hammer-string interaction [Hall 1992b, Vyasarayani 2009, Komano 1994, Chaigne 1994a, Chaigne 1994c], the string vibration [Young 1952, Tufillaro 1995, Tufillaro 1989, Tanaka 1996, Ducasse 2005, Bensa 2003], and the soundboard vibration [Mamou-Mani 2008, Bensa 2005]. In the end, they help to provide important understanding of how the performance of the piano is changed by different modifications of individual instrument parameters.

2.1.3 Soundboard and Ribs

The soundboard is typically a thin panel (thickness between 6 – 10mm) made out of Norway spruce or Sitka spruce [Conklin Jr. 1996c, Yoshikawa 2007], underlying the piano strings and resting upon the wooden frame of the piano. Dried to a very low moisture content [Fukada 1950], the wood is cut type-dependently into strips with a width from 5cm to 15cm. Then the edges of the stripes are glued together, preferring one direction for the wood grain.

The whole soundboard comprises not only the thin wooden panel, but also the supporting ribs mounted on its rear side and the two bridges (treble and bass) on the front side, which are the connections between the board and the strings [Fletcher 1993, Conklin Jr. 1996b]. Acting as a natural resonator, the material and the design of the soundboard makes it very stiff concerning its weight, and therefore it can be excited by the strings due to its lightness [Giordano 1998a]. Typically, the soundboard is curved with the highest point in the middle of the board; the form is then called 'the crown of the soundboard' [Mamou-Mani 2008]. Also made out of spruce and cut along the wood grain, the specially fitted ribs are the reason for this curvature. They are mounted perpendicular to the wood grain of the soundboard and glued to the board with a rib press, which also accurately fixes their positions during this procedure. Finally mounted, they force the board into the above mentioned crown form. Furthermore, the placed ribs will not only have the effect of an increase of stiffness of the board [Giordano 1997]. They also pre-stress the soundboard, which acts as an energy reservoir, releasing the vibrational

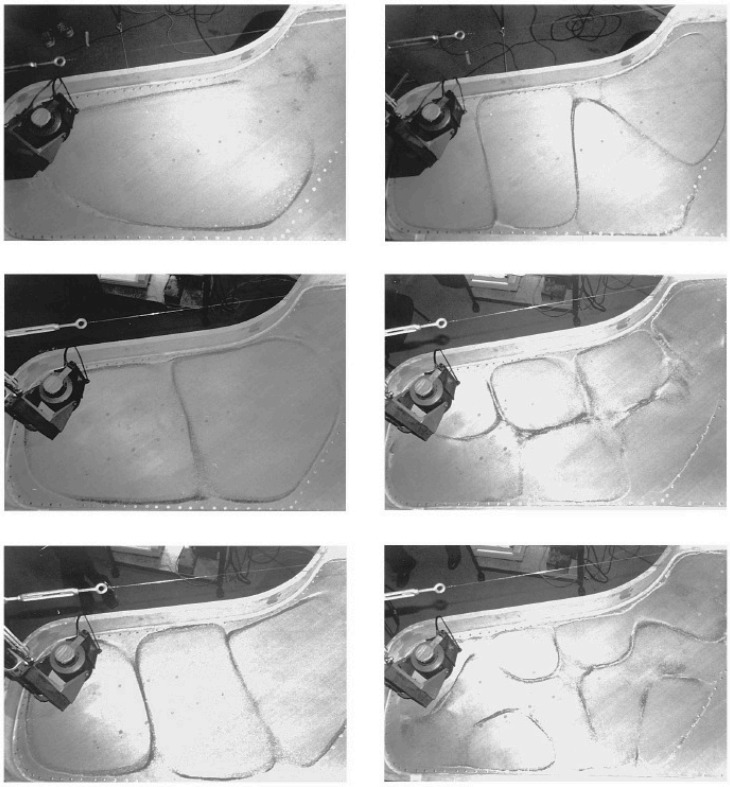

Figure 2.3: (Graph taken from [Conklin Jr. 1996c].) Six different vibration modes nicely presented as Chladni figures on a grand piano soundboard. From top left to bottom left: *first* mode (49 Hz), *second mode* (66.7 Hz) and *third* mode (89.4 Hz). From top right to bottom right: *fourth* mode (112.8 Hz), *eighth* mode (184 Hz) and *eleventh* mode (306 Hz).

energy in case. They additionally have the purpose to 'homogenize' the board in terms of stiffness parallel and perpendicular to the grain. The increasing of the stiffness will typically happen in two different ways: If the ribs' Young's modulus is larger than that of the soundboard, the overall modulus will enhance. Secondly, they increase the thickness of the soundboard h, which yields a higher rigidity (see Eq. 2.1) and therefore the stiffness.

The treble and bass bridges transmit the string vibrations along their whole lengths to the soundboard. While the long treble bridge crosses the high pitch strings, the bass bridge connects the bass strings with the soundboard. The requirements for the bridges comprise a wide field: Going parallel to the grain of the soundboard, they also have to follow the crown form of the board. Moreover, the level of the upper end of the bridge is slightly higher than the string niveau, because the bridges have to support the strings in the down-bearing process of the soundboard crown [Mamou-Mani 2008, Moore 2006]. Otherwise the tone produced by the strings would drop. Therefore, to withstand the generated pressure between strings and board, the bridge material is made of rigid solid blocks of wood, typically maple or beech.

The structure of the soundboard, considering the wood grain and its directions, is highly anisotropic and the equations of motion of a simple

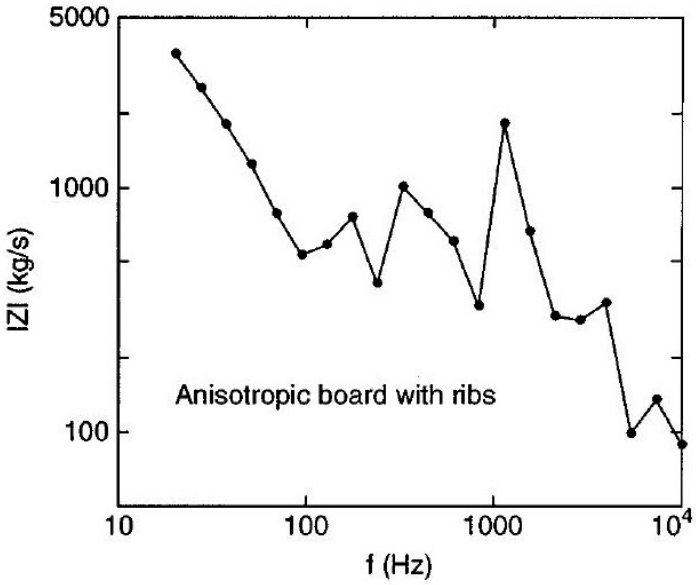

Figure 2.4: (Graph taken from [Giordano 1997].) Mechanical impedance Z of a soundboard + ribs within the Giordano model. The high value of Z at low frequencies mean a low radiation efficiency and therefore also a low sound radiation pressure L_p, which is the typical case for a 'ribbed' soundboard.

rectangular soundboard, including the mounted ribs and excluding the bridges, can be written as [Giordano 1997]:

$$\rho h \frac{\partial^2 z}{\partial t^2} = -D_x \frac{\partial^4 z}{\partial x^4} - (D_x \nu_y + D_y \nu_x + 4D_{xy}) \frac{\partial^4 z}{\partial x^2 \partial y^2} - D_y \frac{\partial^4 z}{\partial y^4}, \tag{2.1}$$

with the respective rigidity factors D:

$$D_x = \frac{h^3 E_x}{12(1-\nu_x \nu_y)}, \quad D_y = \frac{(h+h_{rib})^3 E_{rib}}{12(1-\nu_x \nu_y)}, \quad D_{xy} = \frac{(h+h_{rib})^3 G_{xy}}{12}. \tag{2.2}$$

E_x, ν_x and ρ represent the Young's modulus, Poisson's ratio and the density of the propagating material, respectively, while G_{xy} stands for the shear modulus. h means the board thickness, h_{rib} the rib thickness (in case of $h_{rib} = 0$ no ribs were mounted on the board), x, y and z the coordinates, where z is perpendicular to the soundboard plane. Eq.2.1 describes the transversal motion of the soundboard. Assuming the Giordano model for the sound production [Giordano 1997], the mechanical impedance Z (see A.2.9.1) can be plotted against the frequency (see Fig. 2.4), showing that the presence of ribs on an orthotropic board will not only increase the stiffening of the board, but also the impedance at *low* frequencies rises drastically, while the higher range of the spectrum remain at about the same intensity compared to the simple rectangular board without ribs. A high mechanical impedance Z means a low radiation efficiency and therefore also a low sound radiation pressure L_p. This effect describes exactly the typical case for a real piano soundboard.

But how does the small radiation efficiency for the low spectral range come from, when it was already mentioned in the last section that a soundboard can be a significantly efficient radiator of airborne sound waves? The reason can be found indeed by the frequency dependence of the efficiency. Typically, low frequencies (see Fig 2.4) are less efficiently radiated, because the wavelength is just long enough to be acoustically 'short-circuited' around the board [Bork 1993, Fletcher 1999, Wogram 1980], i.e. the compressed air on one side of the soundboard has enough time to be moved to the other side of the board with the reduced pressure. By neutralizing this difference through the exchange of air, the radiation efficiency drops drastically[5]. But even at higher frequencies a similar effect can occur when certain vibrational modes (See Fig. 2.3 for exemplary modes) cancel out each other [Wogram 1980]. These eigenmodes vibrate in an opposite phase, i.e. one area of the soundboard is moving upwards, while a neighbour region is moving downwards. Hence, the radiation efficiency at these specific modes, which are the 'valleys' in the spectrum, are significantly reduced by the air exchange of the neighbouring regions. However, if the vibrational transfer is too efficient, the piano tone will decay too early. That would mean the tone is too loud and too short. To achieve a compromise, a relatively large part of the vibrational energy needs to be reflected back into the strings.

There are certain rib parameters concerning the spectral radiation, which can be varied. [Wogram 1980] performed investigations on the influence of the rib height and their numbers on the soundboard. When the rib height was reduced gradually, he found at the upper end of the treble bridge no significant change in the input impedance. However, the central region of the soundboard revealed the evolution of pronounced resonances of the impedance below 200 Hz. Also the resonant frequencies are shifted downwards when the rib height was decreased, while their extrema become more sharply defined. Nevertheless, no uniform correlation relating the rib height and the impedance variation was found. He finally concluded, that the bending stiffness exerts a greater influence on the sound radiation than the mass of the ribs and therefore it is more fortunate for the radiation characteristic of a soundboard to use narrow, high ribs than low and broad ones (i.e. increasing the stiffness without increasing the mass in the same magnitude). He also investigated the occuring differences if the rib number on the rear side of the soundboard varies and concluded that a change in the number of ribs has less influence on the input impedance and the sound radiation than a change in rib height.

[Chaigne 2011] presented results at the 'Acoustical Society of America'

[5]This specific effect can be reduced by a closed sound box, which is realized for the guitar and the violine [Fletcher 1999, Elejabarrieta 2002]

(ASA) meeting 2011 about the ribbing influence of the soundboard radiation. He found that an aperiodicity of the ribs would result in a reduction of the spectral peak sharpness. The presence of the ribs would also result in a directivity of the sound radiation, but the main findings are again that the ribs will enhance the stiffening of the soundboard.

2.1.4 Scattering generated by the Ribs

In the course of this investigation ribs will be placed onto a radiating soundboard, i.e. a regular assembly is added to the radiator. Considering these specific add-ons, a model about the sound radiation and the frequency selection by scattering will be necessary. The solid-state physics can hold for such a model – the so-called linear chain model (LCM). Since it is very important for the explanation of the later occuring scattering effects, the LCM model will be presented in this section. It highlights the evolving dispersion relation and distinguishes between 'allowed' and 'forbidden' frequencies (In this case 'allowed' means the frequencies are part of the solution of the LCM model; 'forbidden' refers to no solution), if a given setup is excited. The propagating 'pass band' frequencies, allowed by the external scattering circumstances, are travelling waves. One of the pivotal advantages to referring to this model is that in constrast to surface vibrations, which follow a fourth order wave equation (see Eq. 2.1), body vibrations along a certain direction can be described by a second order wave equation, reducing the complexity of the problem significantly. A description of that scattering model, which sets each individual rib as a scatterer is described in this section. A more profund description is provided in [Ashcroft 1976, Morse 1987, Ziman 1972, Kittel 1953].

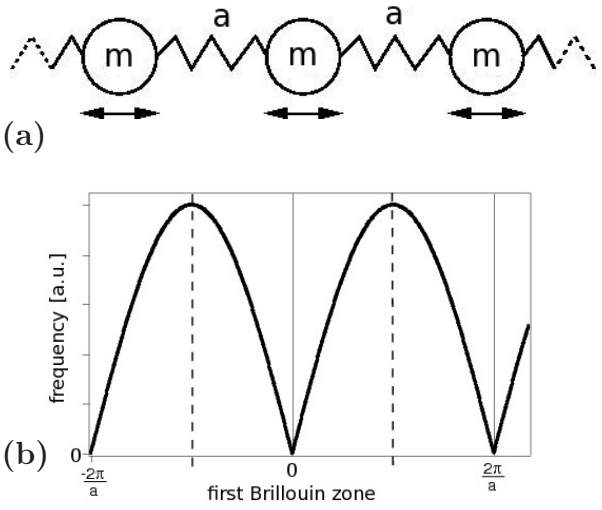

Figure 2.5: **(a)**: 1-dim infinitely extended linear chain of masses with the respective dispersion relation in **(b)**. This represents the basis for the LCM model, where only the nearest-neighbor forces are considered.

2.1.4.1 Linear Chain Model (LCM)

The model comprises an infinite chain of equal masses[6] and perfect springs (see Fig. 2.5a) arranged laterally. Having all masses in their equilibrium point, they have a constant distance a to their next neighbors. The masses further apart are at distances $n \cdot a$, with $n \in \mathbb{Z}$. The sign of n refers to the direction of the chain ('-' $\rightarrow$ left from the actual mass; '+' $\rightarrow$ right from the actual mass). Subsequently, the displacement from its equilibrium point of each mass will be introduced as $u(n\,a)$. To simplify the model considerably, only the interaction between the direct neighbors (one left, one right) is incorporated. Hence, the equation of motion reads:

$$\begin{aligned} & m \cdot \ddot{u}(n\,a) = \quad -\varepsilon[u(n\,a) - u((n-1)\,a)] - \varepsilon[u(n\,a) - u((n+1)\,a)] \\ \Rightarrow \quad & m \cdot \ddot{u}(n\,a) = \quad -\varepsilon[2u(n\,a) - u((n-1)\,a) - u((n+1)\,a)]. \end{aligned}$$

The mass of one single scatterer is represented by m, ε is the spring constant. Both parameters are naturally connected through $\omega = \sqrt{\frac{\varepsilon}{m}}$, with ω as the frequency.

The next step in the model evolution is to set the amount of masses to a finite number N with $n = 1, 2, 3, ..., N$. Knowing that, the boundary condition for the chain has to be clarified. One way would be to let the end masses interact only with the inner side of the chain, but that would end up in complicating the solution unnecessarily. The Born-von Karman periodic boundary condition is by far the most convinient one, where both chain ends are connected to each other with an additional spring of constant ε. The Born-von Karman condition can be written down as:

$$u([N+1] \cdot a) = u(a); \qquad u(0) = u(N \cdot a). \tag{2.3}$$

This approach implies a circle chain of masses, not matching physical intuition from the perspective of a soundboard with placed ribs on it. An alternative view of this boundary condition is an additional massless rigid bar (with a length of $L = N \cdot a$), connecting the outer left with the outer right (cf. Fig. 2.6). Also, the bar representation fits better the conception of a soundboard with placed ribs on it, which will be the case for the following investigations. After the determination of the initial conditions and the equation of motion, one can proceed with the ansatz:

$$u(na, t) \sim e^{i(kna - \omega t)}, \tag{2.4}$$

[6] A common model extension utilizes different masses, which yields the optical branch of the dispersion relation. But only the acoustic branch will be needed in this investigation [Ashcroft 1976].

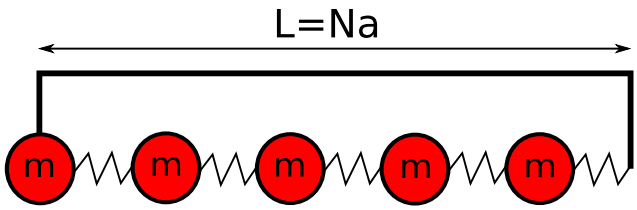

Figure 2.6: Born-von Karman boundary condition: A rigid massless bar connects both ends of the mass chain, which fits the conception of a soundboard with mounted ribs in a better way.

having in mind that the periodic[7] boundary condition needs to fulfill:

$$e^{ikNa} = 1. \tag{2.5}$$

That, on the other hand, restricts k to

$$k = \frac{2\pi}{a} \cdot \frac{n}{N}, \tag{2.6}$$

where n has to be an integer. The range of $-\pi/a < k < \pi/a$ fully comprises the first Brillouin zone. Any change by $2\pi/a$ has no effect on the displacement $u(na)$. Therefore, only N distinguishable solutions exist for this equation of motion.

The following step is to insert the ansatz into the equation of motion. Hence,

$$\begin{aligned} -m\omega^2 e^{i(kna-\omega t)} &= -\varepsilon[2 - e^{-ika} - e^{ika}] \cdot e^{i(kna-\omega t)} \\ \Rightarrow \quad \omega^2 &= \frac{\varepsilon}{m} \cdot [2 - 2\cos(ka)] \\ \Rightarrow \quad \omega(k) &= 2 \cdot \sqrt{\frac{\varepsilon}{m}} \cdot |\sin(ka/2)|. \end{aligned}$$

The 'acoustic branch' solution for the eigenmodes will emerge (see [Ziman 1972, Ashcroft 1976]), if k (Eq. 2.6) is considered:

$$\omega(n) = 2 \cdot \sqrt{\frac{\varepsilon}{m}} \cdot |\sin(\pi \cdot n/N)|. \tag{2.7}$$

The frequency ω vs. wave vektor k is plotted in the range of the first Brillouin zone (cf. Fig. 2.7), showing the frequency distribution of the allowed 'pass bands'.

[7] Despite the bar repesentation of the chain, there is of course a *periodic* boundary condition.

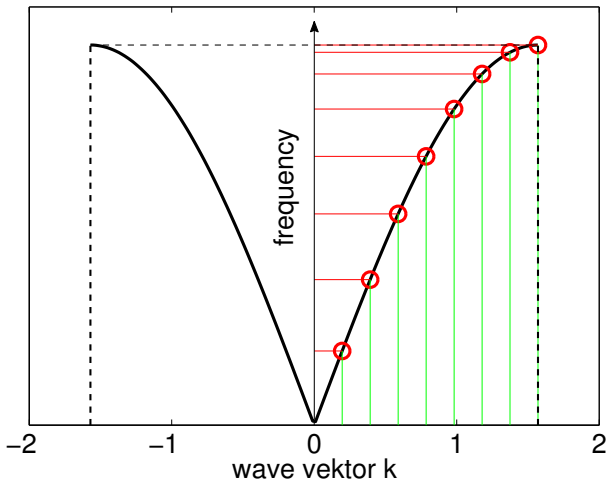

Figure 2.7: Theoretical dispersion relation with a given number of 8 scatterers. The green lines show the equidistant wave vectors k, while the red lines represent the respective frequencies $\omega(n)$.

2.1.4.2 Dispersion Relation: Optical Branch

What about the optical branch of the dispersion relation? Could it be of any significance for the experiments? The optical part of the dispersion relation originates from two different types of scatterers; different in weight and correlation to the neighboor [Ziman 1972, Ashcroft 1976]. Since the weight of the ribs and the correlation to the next neighboor is equal for each scatterer, the optical branch needs no consideration.

2.2 Piezoelectric Polymer Sensors

Piezoelectric materials are widely used as the basis for sensor and actuator technology [Möser 2010]. A special type among these piezoelectrics are polymer-based materials, which not only have the advantage of being flexible in geometry; they also have a superior bending ability compared to piezoelectric ceramics. Some of the most important piezopolymers are polyvinylidene fluoride (PVDF), its copolymer poly(vinylidene fluoride-trifluoroethylene) (PVDF-TrFe), polyamid (also known as nylon) [Newman 1980] and polyurea [Takahashi 1987, Takahashi 1989]; all of them showing different piezoelectric behavior. The following sections will cover the theory of the piezoelectricity and the main characteristics of the sensor polymer used.

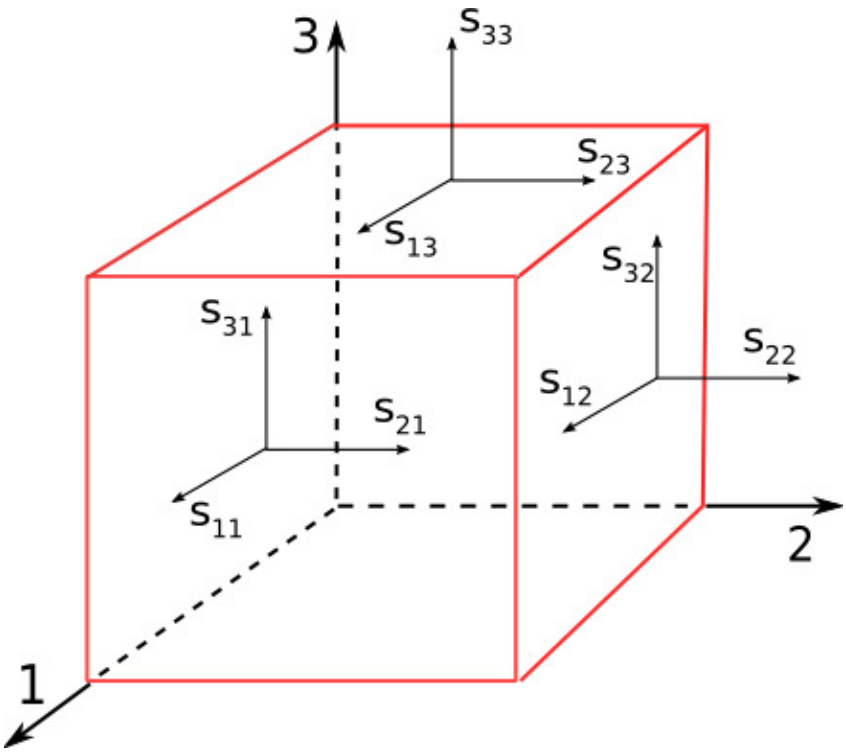

Figure 2.8: Scheme view of the direction-dependent components of the stress tensor s_{ij} depicted on a cube.

2.2.1 Piezoelectricity

The discovery of the direct piezoelectric effect dates back to the 19th century: In 1880 Jacques and Pierre Curie found piezoelectricity in Tourmaline crystals [Curie 1880]. In particular, they found a linear correlation between the external mechanical stress and the developing charge at the surface of the crystal. Through a directed deformation of a piezoelectric material microscopic dipoles within a unit cell evolve, i.e. a shift of the internal charge occurs. The summation of these emerging microscopic dipoles of all unit cells yield a macroscopic electric field and therefore a measureable voltage at the sensor surface. On the other hand, an external applied voltage will end up in a deformation of the piezoelectric material – this is the so-called inverse piezoelectric effect [Landolt 2006].

Since the piezoelectric coefficient plays an outstanding role in this investigation, it is worth taking a look at its origin. By means of thermodynamics, the coefficient d_{mi} can be derived from the enthalpy H [Mellinger 2003]:

$$H = U - \tau_i s_i - D_m E_m;\ i = 1...6;\ m = 1...3 \tag{2.8}$$

where U is the internal energy per unit volume; τ the strain and s the stress tensors depicted in component notation. D_m and E_m are the components of

the electric displacement D and the electric field E. The full representation for τ and s are 3 x 3 matrices τ_{kl} and s_{kl} with all components of the stress tensor depicted on a cube in Fig. 2.8. Both tensors are symmetric with only 6 independent components: $s = (s_{11}, s_{22}, s_{33}, s_{23}, s_{12}, s_{12})$. The notation can be simplifyed by the so-called 1-dimensional Voigt notation: s_i with $i = 1...6$. Thus, the adiabatic piezoelectric strain coefficient d_{mi} reads:

$$d_{mi} = -\left(\frac{\partial^2 H}{\partial E_m \partial s_i}\right)_S \tag{2.9}$$

The index S denotes that the entropy remains constant. The derivation of the enthalpy is complete and can be written as:

$$\mathrm{d}H = -\tau_i \mathrm{d}s_i - D_m \mathrm{d}E_m + T\mathrm{d}S \tag{2.10}$$

Since this differential can be taken in arbitrary order, the adiabatic piezoelectric strain coefficient d_{mi} is represented by:

$$d_{mi} = \left(\frac{\partial D_m}{\partial s_i}\right)_{E,S} = \left(\frac{\partial \tau_i}{\partial E_m}\right)_{s,S} \tag{2.11}$$

The left-hand side of Eq. 2.11 describes the direct piezoelectric effect, i.e. an electric displacement caused by mechanical stress. The $(\frac{\partial \tau_i}{\partial E_m})_{s,S}$ term shows the inverse piezoelectric effect, where a dimensional change is caused by an electric field.

2.2.2 Material: Why Polyvinylidene Fluoride?

Polyvinylidene fluoride (PVDF) (see Fig. 2.9) has a wide range of applications due to its specific mechanical and electrical properties ([Sessler 1999b, Bauer 2004, Zhang 2002, Vinogradov 2002, Tasaka 1981, Nix 1986]). It consists of a repeat unit with the molecular formula $(CH_2 - CF_2)_n$ and exibits, after external poling (see Fig. 2.11c.), one of the strongest piezoelectric behavior within all known polymers (Tab. 2.1 shows several characteristics compared with other materials) [Sessler 1981]. Since the discovery of its piezoelectricity [Kawai 1969], PVDF has become one of the working horses in sensor applications as acoustic transducer and electromechanical actuator. Other crucial advantages for using PVDF are based on its bending ability, ultra-thin dimensions (few micrometers; typical thickness of 30μm) and the high geometric flexibility to fit in every desired form.

Sensor material	ϱ [g/cm^3]	v [m/s]	d [pC/N]	Z [$10^3 \cdot$ Ns/m^3]
PVDF (β-phase)	1.78	2300	$d_{33} = 20 - 30$	~ 4
PVDF (δ-phase)	1.78	2300	$d_{33} = 10 - 15$	~ 4
PZT	7.5	2700	$d_{31} = 100 - 300$	~ 20
barium titanate	6.0	3200	$d_{31} = 80$	~ 19
quartz	2.7	3750	$d_{31} = 2$	~ 10

Table 2.1: Typical characteristics (physical and piezoelectric) for common sensor materials [MSI 2006]. Density ϱ, longitudinal velocity v_c, piezoelectric coefficient d and the acoustic impedance Z (see Sec. A.2.9.1, enlisted respectively. PZT refers to lead zirconate titanate, a commonly used piezoelectric ceramic.

In addition, PVDF is predestined to be used for measuring solid-state sound vibrations in wood and synthetics due to the specific acoustic impedance Z (see Sec. A.2.9.1 and Tab. 2.1 for the specific values) because Z_{wood} is just a half magnitude below Z_{PVDF} [Bucur 2006, MSI 2006]. Z_{PVDF} is closer to Z_{wood} compared to the acoustic impedance of other typical piezoelectric materials (see again Tab. 2.1). Therefore, internal sound wave reflections at the material interfaces are reduced to a minimum and these effects can be safely neglected for the small obstacles used in this investigation. It should be noted here, that PVDF has a negative piezoelectric effect, meaning that it will compress instead of expand when exposed to the same electric field [Pu 2010]. This behavior is different in contrast to other piezoelectric materials like PZT, which have a positive piezoelectric effect.

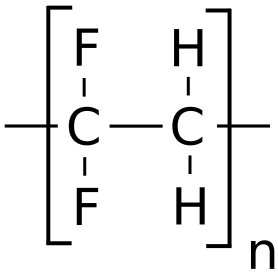

Figure 2.9: Chemical formula of polyvinylidene fluoride as a repeat unit [Kawai 1969].

2.2.3 PVDF Morphology & Piezoelectricity

PVDF is one of the most important fluoropolymers, having four different crystallite modifications, know as the α, β, γ and δ phase, which are additionally referred as form I (β phase), form II (α phase), form II$_p$ (δ phase, which is actually the polar form II) and form III (γ phase) (see Fig. 2.10a & b). Since it is the thermodynamically most stable form of PVDF, the non-polar α phase makes up the biggest share in melt-processed films. The phases α and δ actually have the same molecular configuration, but they crystallize in a different manner. While the α phase is arranged such that the dipole moment of the different molecular chains is zero (cf. Fig. 2.10b

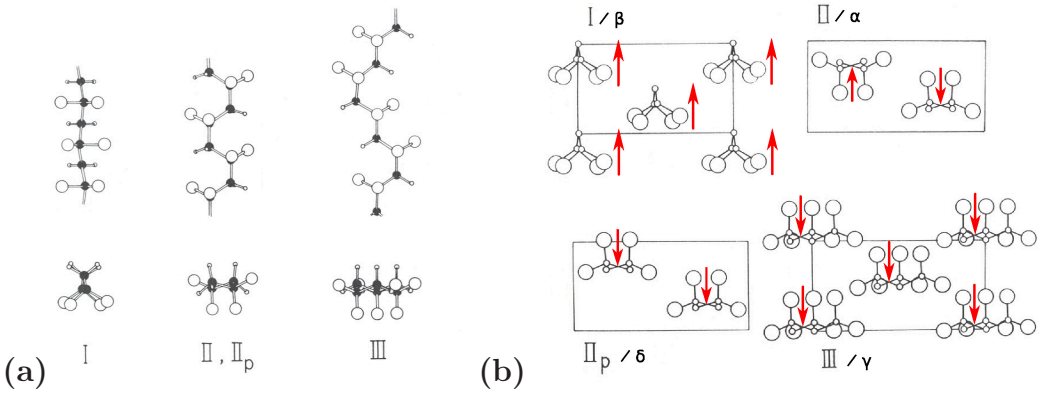

Figure 2.10: The three different molecular modifications of PVDF (**(a)**) and their four respective crystallization forms (**(b)**). Commonly known as form I (β-phase), form II (α-phase), form II$_p$ (δ-phase) and form III (γ-phase). The red arrows represent the net dipole moment for each individual molecule variation. (Graphs taken from [Tashiro 1981]).

(II(α)); the dipole moments for each chain are indicated by red arrows), the dipole moment for all molecular chains in the δ phase have the same direction resulting in a non-zero overall polarization for this configuration. Also the γ phase crystallization has a non-zero overall polarization, since the molecular chain orientation for this configuration also has the same direction.

For the sensor technology, the β phase PVDF (cf. Fig. 2.10b (I(β)) is the most interesting. Having the largest vacuum dipole moment of $\mu = 7 \cdot 10^{-30}$Cm, which is associated with the negatively charged fluor atoms and the positively charged hydrogen atoms, it is predestined for sensor construction and piezoelectric applications of any kind. Creating the β phase PVDF, one typically needs to stretch α PVDF melt cast (cf. Fig. 2.11a & b). With a strong external poling an overall net dipole moment is introduced into the PVDF film. The electric field for the case shown in Fig. 2.11b is perpendicular to the stretch direction.

Being in the solid state, PVDF has a typical cristallinity of about 50% [Furukawa 1981, Das-Gupta 1991]. At the crystalline / amorphous phase interface charge traps are formed by the oriented molecular dipoles. The trapped charges at the transition stabilize the remanent polarization within the PVDF [Sessler 1999b, Rollik 1999]. The dipole density and hence the overall polymer polarization can be changed by an external force. That means, in the presence of a variable external stress, movable compensation charges are generated at the surfaces of the piezopolymer and yield a measurable signal. By the recording of this signal, the precise amplitude of the external force on the polymer surface can be investigated by the direct piezoelectric effect.

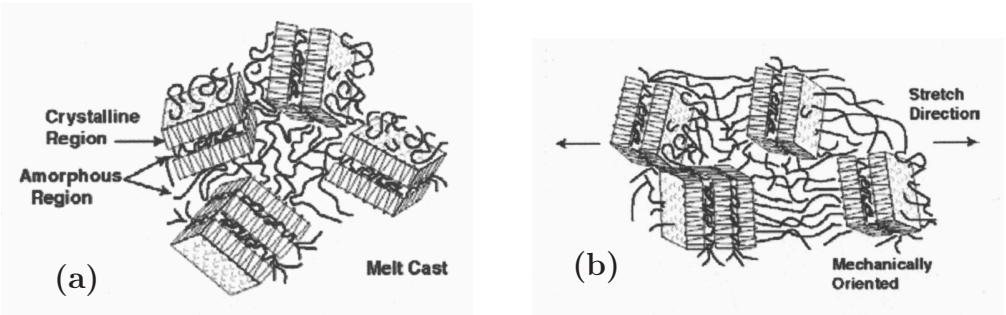

Figure 2.11: (Figures taken from [Harrison 2001]) Schematic overview of the creation of β phase PVDF from the α phase melt cast PVDF. **(a)**: The morphology of the melt cast film. Also the amorphous and crystal lamellae within the PVDF polymer are shown. **(b)**: The configuration of the mechanically stetched polymer film. By poling with an external electric field, a macroscopic dipole moment is established in the polymer (The electric field in this case is perpendicular to the stretch direction.).

Chapter 3

Measurement Techniques

The present chapter consists of two sections. The conceptional soundboard measurements (described in chapter 4) were carried out inside an anechoic chamber. Therefore, the characterization and classification of the recording room will be discussed in the first part of this chapter. The second part is about specially prepared piezoelectric polymer sensors, which are able to record solid-state vibrations. This section comprises the full description and the pivotal calibration and characterization. Finally, there is a brief section at the end of this chapter about condenser microphones, which were used for the airborne sound measurements throughout this investigation.

3.1 Characterization of the Measurement Room

Within a measurement room an acoustic wave can be perturbated by two effects [Möser 2007]: Interferences with ambient noise from outside the room and reflected sound waves within the room are possible. Both effects should be minimized, because they can have a huge impact on the time signal and the spectrum. Naturally, it is impossible to eliminate these perturbation effects completely, but they should be limited to a certain niveau within the spectral data acquisition range. Only in this case one can obtain scientific statements about the investigated signal with some certainty.

For the reduction of the reflected sound waves [Möser 2007] we need an attenuation material on the inner surface of the measurement chamber, which was done by a layer of mineral wool and additional specially manufactured pyramid foam, which is described below. Special material at the outer wall of the room reduces the influence of the external ambient noise by soundproofing. Both mechanisms rely on different physical principles: While by soundproofing the external perturbation sound waves are reflected more efficiently from the measurement chamber, the absorption layer depletes the amplitude of the signal via friction within the material. All characterization measurements of the recording chamber will be given in the following. With these investigated parameters the room is fully acoustically classified according to the DIN e.V. norm ([DIN e.V. 2005a, DIN e.V. 2005b]).

3.1.1 Geometry & Material

The acoustic laboratory consists of a normal room (without soundproofing and absorption layer) in which most of the recording devices are located and installed. Within this room another room is built (see Fig. 3.1a), which is the actual acoustic measurement chamber. It stands 0.57m away from the surrounding walls of the outer room. Because these two chambers are not interconnected – except for the floor naturally – possible influences from building vibrations, which certainly exist and are measureable (e.g. closing doors, ventilation or even a person passing by), are reduced to a minimum.

The outer wall of the recording room is 23cm in thickness (without inner absorption layer) and consists of two individual gypsum plaster boards 2.65cm in thickness. They are 17.5cm in distance from each other. The gap between those boards is completely filled with mineral wool. Gypsum plaster boards are easy to handle for constructions, but unfortunately their density is pretty low ($\varrho_{\text{gypsum}} = 2.3\text{g/cm}^3$) compared to other material, which is used for room construction. Typically, the higher the density, the higher the ability to reflect airborne sound waves, due to the larger acoustic impedance mismatch (see A.2.9.1). Nevertheless one can assume, due to the big mineral-wool-filled cavity between the two plates, a certainly good damping factor for the outer ambient noise. The inner surface of the recording room is permanently covered with a combination of two different damping materials: the basis is formed by a 8cm thick mineral wool layer (see Fig. 3.1b), whereas the top layer is made of special acoustic pyramid foam (see Fig. 3.1c). The floor is also covered with a mineral wool layer and to be able to enter the room a metal grid is installed.

The dimension of the recording room (without the absorption layers) is 3.075m x 3.13m x 3.23m in width, length, and height respectively. Therefore one has a volume of $V \simeq 31\,\text{m}^3$ and a surface area of $S \simeq 60\,\text{m}^2$. If a sound source is placed in the middle of the room, the distance between the source and the wall is 1.46m (subtracting the absorber layer). The literature [DIN e.V. 2005a, DIN e.V. 2005b] defines the lower frequency confidence level of a measurement room as the minimum distance of one wavelength (from sound source to the inner wall). For the air temperature of 20°C that can be calculated by:

$$f_{conf} \approx \frac{c_{\text{air}}}{\lambda} = \frac{343\frac{\text{m}}{\text{s}}}{1,46\text{m}} \approx 230\text{Hz} \tag{3.1}$$

f_{conf} represents the lower limit for trustworthy results obtained in this measurement room. On a later point this will be verified by the room characterization measurement (see 3.1.2.2).

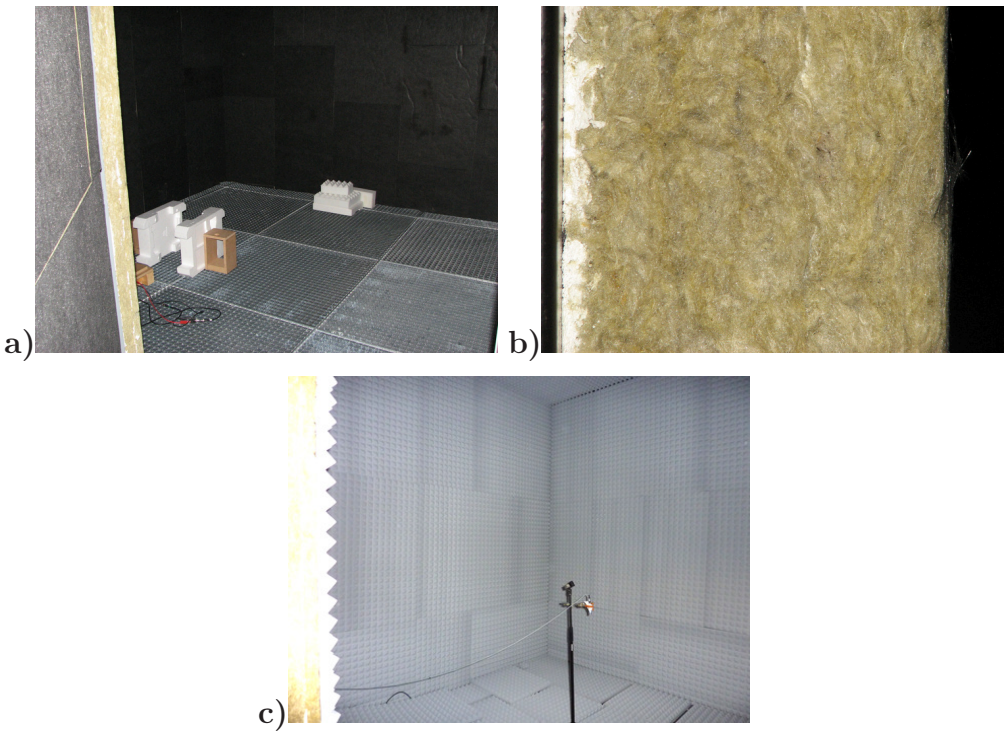

Figure 3.1: a): Overview of the acoustic measurement room seen through the door. The metal grid used for the entering of the room is seen beside some equipment. **b)**: Side view of the 8cm thick absorption material made out of mineral wool.
c): Showing the finally attached pyramid aborption layer of the anechoic chamber (See Sec. 3.1.1 for description.).

3.1.2 Sound Wave Absorption

3.1.2.1 Specification

The pivotal aim of sound wave absorption is to reduce the field of sound waves on a wide frequency range within the recording room. Due to inner friction within the absorption foam the amplitude of the reflected sound wave is reduced. In Eq. 3.1 the lower confidence level of the measurement chamber was found at about 230Hz. For higher frequencies, the absorption of the inner layers is very good.

For the special pyramid foam on top of the mineral wool layer, the frequency-dependent sound wave absorption coefficient α was provided from the manufacturer 'Pinta Acoustics GmbH'. Regarding the overall absorption layer (including the underlying 8cm mineral wool), this setup is very close to the 'pinta pyramid 100/50' configuration in terms of thickness and material, having absoption coefficient values given in Tab. 3.1.

frequency [Hz]	125	250	500	1000	2000	4000
absorption coefficient	0,30	0,80	0,99	0,99	0,99	0,99
reverberation time [ms]	232	51	18	18	18	18

Table 3.1: The absorption coefficient and the calculated reverberation time (see eq. 3.2) for the overall absorption layer ('pinta acoustic' pyramid foam and 8cm mineral wool; close to the 'pinta pyramid 100/50' configuration (see the producers' webpage)). Given are the values for the typical reference frequencies.

Due to the material structure, the complete absorber layer (wool and foam) has many internal air pockets, rapidly increasing the friction of a sound wave. The installed absorbers are predestined for a good absorption characteristic given the relatively large thickness of these layers.
Knowing the dimension of the recording room (volume V and surface area S) and the frequency-dependent absorption coefficient α (see Tab. 3.1) one is able to calculate the reverberation time T with the help of the Eyring formula ([Filippi 1999]):

$$T = \frac{0,16 \cdot V}{-\ln(1-\alpha)S} \tag{3.2}$$

This theoretical reverberation time T gives a lower limit for the real reverberation time. This formula yields a reverberation time of 51ms at the frequency of 250Hz ($\alpha = 0.80, S \simeq 60\,\mathrm{m}^2, V \simeq 31\,\mathrm{m}^3$) being just above the lower confidence level of 230Hz calculated with Eq. 3.1. Given this reverberation time for 250Hz a signal is reduced by a factor of 1000 within 12 vibration periods. But due to imperfect absorption, resulting from perturbations in the absorption layers and the metal grids installed on the floor, the actual reverberation time of the measurement room is higher than the theoretical value. The real reverberation time will be validated by measurement (see Sec. 3.1.3).

3.1.2.2 Absorption Measurement

To check the absorption ability of the inner layer of the measurement room, one assumes the radiation characteristic of a monopole sound source (see [DIN e.V. 2010, Russell 1998]), for which theoretically the sound pressure (see Appendix A.2.10) is reduced by a factor of two if the distance from the microphone to the loudspeaker is doubled[1]. It needs to be investigated if this absorption behavior is perturbated by any reflections within the room. Therefore, a single special loudspeaker placed in the middle of the

[1]Which is in contrast to the intensity, which has a distance progression of $\sim 1/r^2$

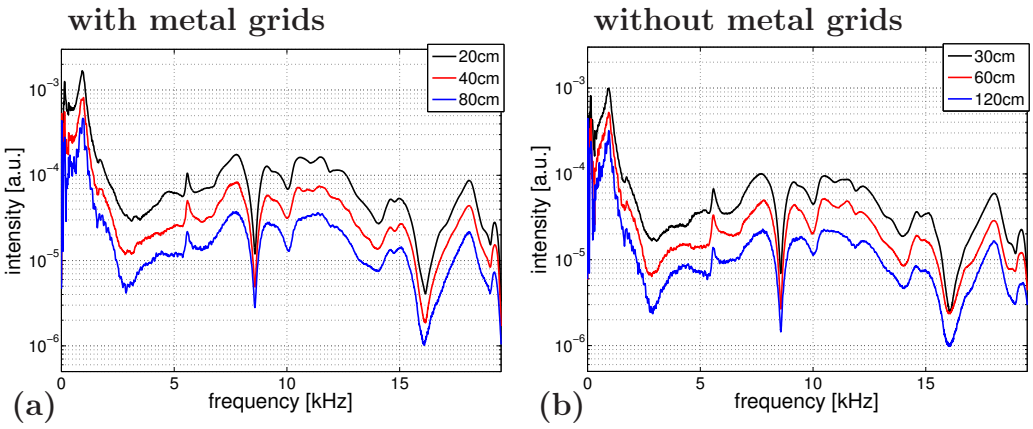

Figure 3.2: **(a)**: Measurements with metal grids on the floor. Sound pressure measured at different distances to the loudspeaker (20cm, 40cm and 80cm). **(b)**: Measurements without metal grids. Sound pressure recorded at the distances of 30cm, 60cm and 120cm from the loudspeaker.

room was used for this absorption quality measurement. The loudspeaker is mounted in a wood construction with a 4cm hole in front of the loudspeaker membrane. The relatively small hole in front of the loudspeaker membrane mimicks a monopole sound source. The sound pressure recording was realized with a 1/2" free-field B&K condenser microphone 'type 4192' with the connected preamplifier 'type 2669' (see Appendix A.1.1) and the compatible B&K amplifier 'Nexus Condition Amplifier'. During the measurements, the microphone was located right above the loudspeaker with the following distances to the speaker hole: 20cm, 30cm, 40cm, 60cm, 80cm and 120cm. The various distances ensure sufficient averageing for this classification. There was also a discrimination between measurements including the metal grids installed on the floor and without them, to check the influence they could have on the characteristic. At the same time, the position of the sound source is slightly changed to minimize possible room resonances. Induced by a frequency generator, the loudspeaker produced a sweep ranging from 20Hz to 20kHz. At different distances to the loudspeaker, the sound pressure is measured (plotted in Fig. 3.2). The spectral quotient between these distances gives the room reflection characteristic, which is ideally a straight line around the value 2 for the doubled distance (see Fig. 3.3).

The spectral characteristic of the loudspeaker is not flat resulting from its construction and geometric dimension. But for the determination of the sound pressure quotient, which is a relative parameter, it is not important to have a flat response function. The reflection room characteristic (see Fig. 3.3), including the installed metal grids, has a good absorption behavior starting

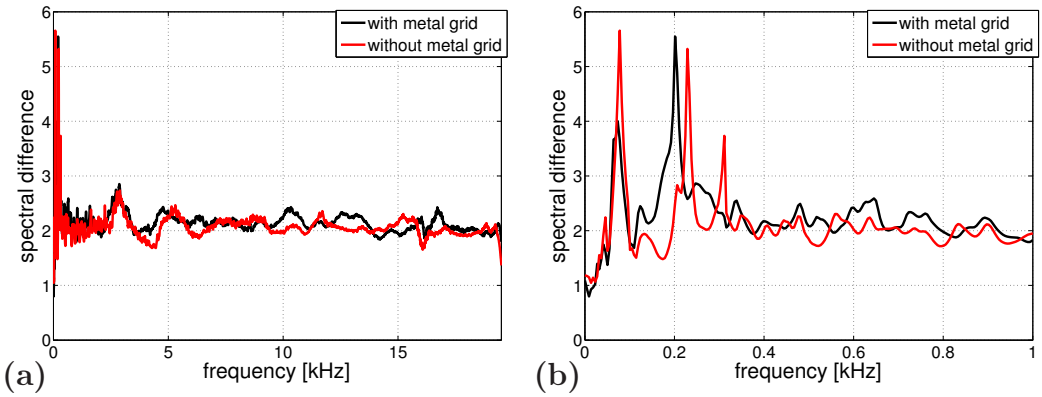

Figure 3.3: a): Sound pressure quotient with/without the installed metal grids on the floor shown the frequency range up to 20kHz.
b): Same as a) but with a zoom of the range 0kHz to 1kHz. The ideal room absorption characteristic would be a straight line along the value 2.

from 230Hz to 20kHz, where the sound pressure quotient is about in the range of factor 2. Despite assuming a better characteristic for the measurements without the metal grid, the range of the sufficiently good absorption behavior starts without the grids at about 320Hz; in constrast to the room with the grids, where good absorption is guaranteed above 230Hz. This is, by the way, in very good agreement with the lower frequency confidence level found with Eq. 3.1. Only for higher frequencies the 'no metal grid' curve becomes a bit smoother and closer to quotient 2. As a conclusion one can say, that it has almost no influence if the metal grids are placed in the room or not. Due to a lower frequency confidence level and better practicability (entering the chamber; de-/installation of the grids) the metal grids stay in the room while measurements are running.

Another effect occurs, if inner sound wave passes the absorption material and is reduced by a significant proportion in its energy. The remaining amplitude of the wave excites the rear wall of the measurement chamber, which is made out of plaster board, by its resonant frequency. The generated wall vibrations create airborne sound radiating within the recording room. For the present measurement configuration this effect has only a theoretical aspect. Within the range of the resonant frequency of the gypsum plaster boards (which is around $f_r \sim 1200$Hz) this effect could not be observed.

3.1.3 Reverberation Time

The reverberation time T [Möser 2007] is one of the most important parameters for an acoustic laboratory. This value denotes the time in which

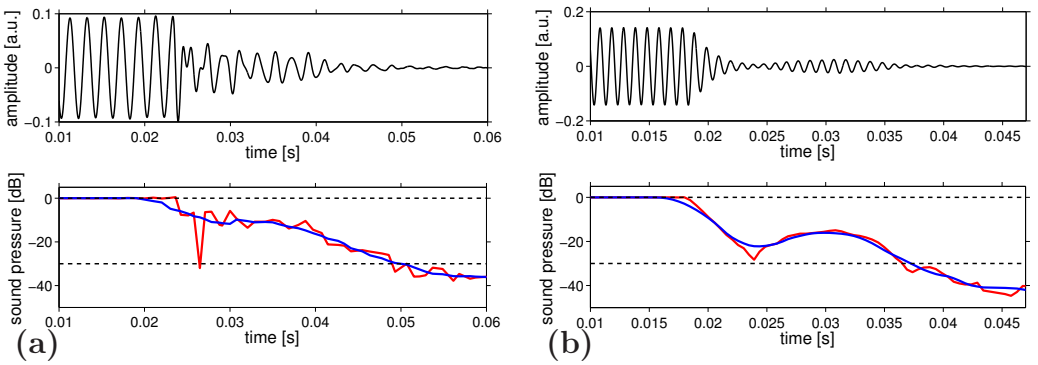

Figure 3.4: Determination of the acoustic room reverberation time T exemplarily shown for the frequencies 500Hz (**a**) and 1kHz (**b**). *Top*: Time dependent sinusoidal signal, including the switch-off. *Bottom*: Calculated effective value for the sound level L_p depicted in red. A smoothing of the effective sound level in blue. The dashed lines represent the 30dB intervall between the effective sound pressure of the loudspeaker and the intersection point for $T_{1/2}$. The full reverberation times for the plotted curves are $T_{500\text{Hz}} = 51\text{ms}$ and $T_{1000\text{Hz}} = 38\text{ms}$.

the sound pressure is reduced by a factor of 1000, i.e. the signal drops by 60dB (see Eq. 3.3). In many cases it is more practical to determine the 'half of the reverberation time' $T_{1/2}$, because a reduction of 60dB probably means a drop below the background noise of the recording room. Therefore, the drop by 30dB is usually measured and one is able to calculate the full reverberation time T.

For the verification of $T_{1/2}$ the following devices were used: the above mentioned loudspeaker, the B&K measuring system, the frequency generator 'Agilent 33220A 20 MHz Function Generator' and a computer. Driven by a sinusoidal function from the frequency generator, the loudspeaker radiated this signal and the B&K system recorded it, while the computer saved the data. During the sinusoidal radiation the electrical connection of the loudspeaker was interrupted. Knowing the following sound pressure decline, the reverberation time can be determined.

For this investigation one needs a relation between the sound pressure $\tilde{p}$ and the sound level L_p in [dB] (see Appendix A.2.10), which is defined via ([Hartmann 1998]):

$$L_p \stackrel{\text{def}}{=} 20 \cdot \log_{10}\left(\frac{\tilde{p}}{p_0}\right)[\text{dB}] \tag{3.3}$$

with $\tilde{p}$ representing the *effective* sound pressure, which is given by the maximum value of the current sound pressure with $\tilde{p} = p_{\max}/\sqrt{2}$. $p_0 = 2{\cdot}10^{-5}$Pa at 1000Hz is defined as the threshold of human hearing ([Veit 1996]),

Frequency [Hz]	125	250	500	1000	2000	4000
Reverberation time [ms]	86	75	60	40	26	21

Table 3.2: Full reverberation time for the given frequencies of the acoustic measurement room. A comparison between the experimentally measured and the theoretically determined full reverberation times are displayed in Fig. 3.5.

which is about 10^6 times smaller than the average human ear can withstand before it gets damaged at a sound pressure of $\sim$ 20Pa. Due to the large range of sound pressure, the scale is commonly used in logarithmic units.

In Fig. 3.4 the determination of the half of the reverberation time $T_{1/2}$ ([Möser 2007]) is demonstrated on two different examples, namely for the frequencies 500Hz and 1kHz. The top curve depicts the time signal, which was used for the reverberation time analysis. Then, the sound level L_p (plotted as the red curve in the bottom picture) is calculated from the maximum sound pressure $P_{\max}$ and the respective effective sound pressure $\tilde{p}$. A smoothing of L_p (blue curve) was performed to make a secure statement about the intersection point with the lower dashed line, which represents, together with the upper dashed line, the 30dB range – exactly the half of the normal 'reverberation range'. The time difference between the beginning of the decay and the intersection represents $T_{1/2}$. To obtain the full reverberation time $T_{1/2}$ needs to be doubled. The present examples (Fig. 3.4) exibit a full reverberation time of $T_{500\text{Hz}} = 51$ms and $T_{1000\text{Hz}} = 38$ms.

The measurement with the condenser microphone took place at four different locations within the recording room to average out possible resonances. The frequencies, which are commonly used for the characterization of the room reverberation time are: f = 125Hz, 250 Hz, 500Hz, 1kHz, 2kHz and 4kHz. Tab. 3.2 displays the measured values for the full reverberation times T at these frequencies. The comparison between the theoretical (black line) and the experimental (red line) reverberation times is displayed in Fig. 3.5 on a logarithmic frequency scale. There is a significant discrepancy between both curves in the range from 250Hz to 2kHz. The deviations are most likely due to the theoretical absorption coefficients given in Tab. 3.1: While the theoretical absorption coefficients only describe a stand-alone absorption layer, the measurements were carried out within a recording room, which includes metal grids for walking, a door frame, a door handle etc. All these additional parts cause reflections resulting in a larger reverberation time. Nevertheless, the values beginning at 1000Hz, which have a reverberation time lower than 40ms, are quite good for the size of the measurement room.

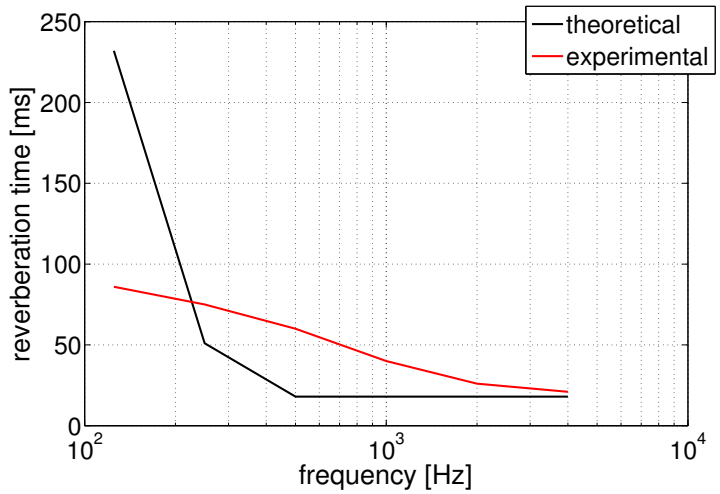

Figure 3.5: Theoretically and experimentally determined reverberation time for the acoustic room given for different frequencies.

3.2 Preparation of the Polymer Sensors

3.2.1 Sensor Production

The sensor material used in this investigation was mono-axially stretched prepoled piezoelectric polyvinylidene fluoride (Kynar-PVDF) [Kawai 1969] produced by Piezotech. The main advantage of this polymer film can be described with an extremely thin design, being just micrometers in height, while their extension is macroscopic (sub-millimeter to centimeter size). All used piezopolymer samples have a thickness of $30.1 \pm 1.2\mu$m and a density of $\varrho = 1.78\text{g/cm}^3 \pm 0.5\%$. This typical thickness of polymer samples is due to the poling process, because thicker films require very high voltages [Dickens 1992]. Electrodes, sputtered at the top and bottom surfaces, need to be attached in order to measure the current, which is produced by thickness variations caused by the structure-borne sound waves (see Sec. 2.2.1).

One of the main goals of this investigation is to mount specially prepared PVDF sensors inside of an instrument – in particular within a piano between the soundboard and the bridge, which are both made out of wood (see Sec. 2.1). It is commonly known, that sound wave reflections will appear at material surfaces, if the specific impedances of the used transition materials have not the same magnitude. Fortunately, the acoustic impedance (Sec. A.2.9.1) of PVDF ($Z_{\text{PVDF}} \sim 4{\cdot}10^6$ kg/m$^2{\cdot}$ s) is closer to Z_{wood} ($\sim 0.75{\cdot}10^6$ kg/m$^2{\cdot}$ s) compared to other typical piezoelectric materials (see Tab. 2.1), reducing possible disturbing reflections [MSI 2006, Bucur 2006].

From the perspective of acousticans, there is a major advantage in using the PVDF sensors: These accelerometers solely measure structure-borne vibrations [Möser 2007] without being disturbed by ambient *airborne* sound.

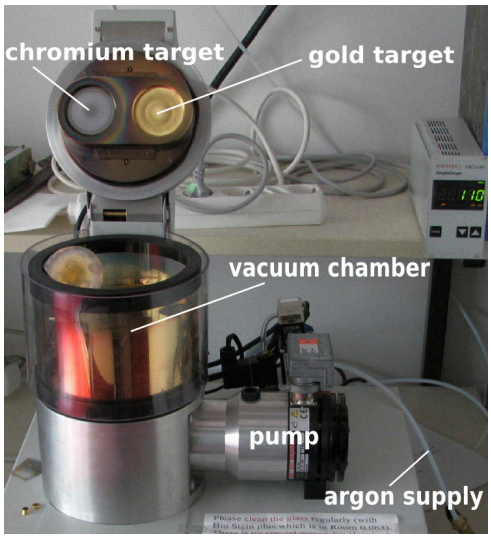

Figure 3.6: Photo of the sputtering device nicely showing the chromium and gold targets.

Thus, they can be used for measurements in almost every environment, as long as the measured setup is decoupled from structure surroundings, e.g. the basement.

Sputtering Electrodes: Due to the piezoelectric effect (see Sec. 2.2.1), an external force will generate compensation charges, which appear on both surfaces of the thin polymer film. To detect these charges, thin metal electrodes are attached on the top and bottom surfaces of the PVDF sensors. Sputtering thin metal films (chromium and gold) to the PVDF film is a fast, easy and relatively inexpensive method of applying electrodes to a sensor surface. The samples were sputtered with the Sputter Coater Emitech 'K575XD' (see Fig. 3.6) attaching a chromium and gold layer with an overall thickness of 56nm (chromium layer with 24nm and gold layer with 32nm). The chromium serves as a stabilizer for the final gold layer, rendering it more durable on the piezopolymer film.

For the sensor design (sketch drawn in Fig. 3.7a), it needs to be taken into account that the generated electric signal depends on the sputtered conduction layer on the PVDF film. Only the 'both side sputtered area' of the sensor film (the 'active recording' area [MSI 2006]; marked by the slightly reddish square in Fig. 3.7a) will contribute to the measurement signal, if an external varying force is applied. Lacking a metal layer, the 'wings' of the electrodes are not able to establish a clear electric field. Therefore, these areas will not significantly contribute to the overall signal. This has to be taken into account, when the film area is determined for the reconstruction of the external force. Another aspect of the actually used design was the relatively long distance between both electrode 'wings'. This certain form was choosen to reduce

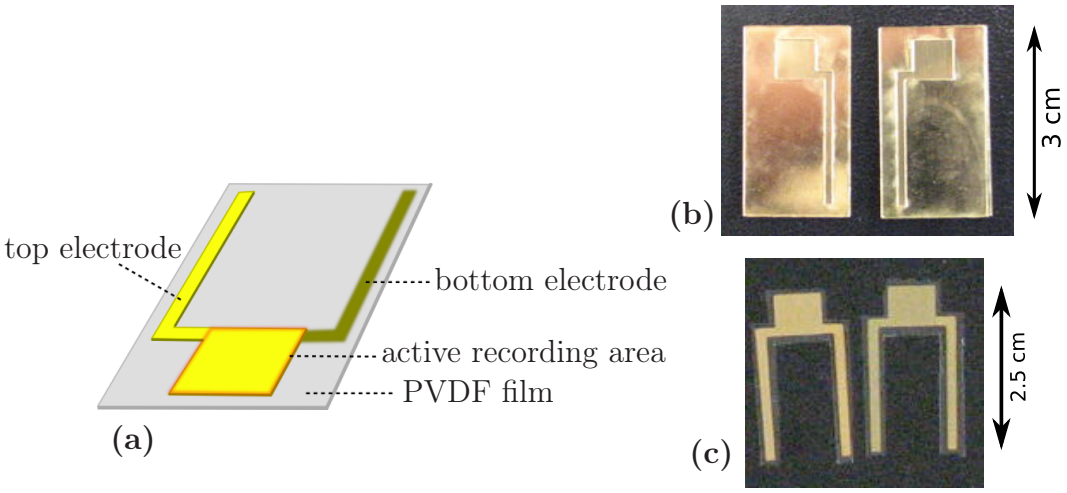

Figure 3.7: **(a)**: Sketch of the specially designed PVDF sensors, which are used for the Bechstein measurements, including the PVDF film as the basis and the top and bottom electrodes (main recording area (reddish square) and the 'wings'). Further descriptions in the text. **(b)**: One side of the masked and already sputtered PVDF film. **(c)**: After removing the mask and cutting the PVDF sheet closely to the gold electrodes.

distracting signal interactions between them.

In the next paragraph, it will be explained that the sensor structure was not clear from the beginning. Moreover, the current design was the result of a long evolution. For a certain time, a completely different sensor design was under consideration, with the electrode 'wings' on opposing sides (in contrast to only one side) to achieve an entirely symmetric arrangement. That way, possible signal perturbations between the electrode 'wings' would be reduced to a minimum. But the design ends up in having the electrodes at one single side due to constructional reasons, especially for the Bechstein measurements (see Sec 5.2). Of course, if one only has the intention to just place sensors in the final constructed instrument, the symmetric arrangement would be the perfect design, because the connection to the amplifier needs to be done only once. But the purpose of this investigation was always to determine the differences in the sound-wave propagation depending on the construction steps and hence, the connections to the sensors needed to be removable all the time.

During the sputtering process of the electrodes, specially cut masks need to be fixed on both sides of the sensor to produce a defined recording area [MSI 2006]. The usual mode of operation for the sputtering is as follows: i) cut masks from polyethylene (*PE*) pieces; ii) cut PVDF samples slightly smaller than the masks, iii) glue them together, sandwiching the PVDF film between

the PE-masks; iv) afterwards, the chromium and gold layers are sputtered onto both sides (see Fig. 3.7b); v) removing carefully the masks from the PVDF film, avoiding short-circuits (top to bottom electrode) by damaging the fragile PVDF sensor; vi) the last step includes a final cut of the PVDF film closely along the electrodes without striking them (see Fig. 3.7c). This cut, which was also a recommendation from the piano makers, minimizes unnecessary sensor surface. The less film material is glued into the instrument, the better the investigation follows the minimal-invasive approach.

An example for a fully sputtered PVDF film is shown in Fig. 3.7c. These sensors are used for the Bechstein measurement program and have a recording area of about $A = 3.6 \cdot 10^{-5}\mathrm{m}^2$ and a side length of the main electrode area of $l = 0.006\mathrm{m}$.

3.2.2 Calibration & Characterization

The following calibration and characterization of the PVDF films are fully described in [Kappel 2011] and below.

To use the PVDF sensors as measurement devices with a sufficient accuracy, the calibration and the characterization were performed with respect to pivotal key parameters. There were calibration investigations towards the dependence of the piezoelectric coefficient[2] on the initial pressure and the dynamical force amplitude. Also the long-term stability and the frequency response, which is probably the most important parameter for acousticians, were documented for the characterization.

The data analysis throughout this investigation, comprising the whole data processing and the respective plotting, was performed with 'matlab R2008a' [The MathWorks, Inc.].

3.2.2.1 Setup

The direct piezoelectric effect (see Sec. 2.2.1) is defined as the response of the material to an external force [Mellinger 2003, Wada 1981]:

$$d_{ij} = \left(\frac{\partial D_i}{\partial \sigma_j} \right)_E \tag{3.4}$$

with D as the electric displacement, σ as the stress and the constant electric field E; d_{ij} is the tensor describing the piezoelectric coefficient of the material. With $D = Q/A$ and $\sigma = F/A$ (with A describing the same area), Eq. 3.4 can

[2] PVDF has a negative d_{33} value, meaning that it will compress instead of expand [Pu 2010]

be rearranged in terms of a dependence on the charge difference:

$$d_{ij} = \left(\frac{\partial Q_i}{\partial F_j}\right)_E \tag{3.5}$$

where Q, A and F are the charge, the constant surface area and the external force, respectively. Assuming a constant temperature during the measurements, the piezoelectric coefficient d_{ij} can be determined via Eq. 3.5, due to the linearity between generated charges and external force. In a typical setup, which was also used in this investigation, the sensor sample is clamped vertically onto a conductive plate, such that no force contribution parallel to the sensor surface appears and no additional charge will be generated through other piezoelectric coefficients than d_{33}. It is therefore characterized by the surface charge Q generated in dependence on a normal external force F, and it is a measure for the sensor sensitivity:

$$d_{33} = \frac{\Delta Q_{33}}{\Delta F_{33}} \tag{3.6}$$

This means, an applied force acting onto the sample/sensor can be reconstructed and determined with the the help of a known d_{33} coefficient and a measured charge difference ΔQ_{33}. To obtain ΔQ_{33}, the recorded voltage difference ΔU_{33} needs to be put into $Q = C \cdot U$. The calculation of the capacitance C of the PVDF, together with the determination of the dynamic force ΔF_{dyn} will be carried out at the end of this chapter.

There are two ways to determine the piezoelectric coefficient – the static and the dynamic force measurement, described in [Hillenbrand 2004, Kremmer 2007, Künstler 2000].

The static force method yields only one single d_{33} value for each individual measurement. Furthermore, this method does not take the frequency into account. Both features are crucial disadvantages. Hence, achieving a convenient averaging of the single values needs a lot of time. The dynamic force measurement, which is described in Fig. 3.8a & b is much faster and more accurate than the static one. The measurement algorithm was performed as follows: a constant static force F_{stat}, which was exerted by an adjustable screw, is directed to the plain surface of the PVDF sensor, acting on an area with 1 cm in diameter. The surface of the PVDF sensor is covered with a conductive layer (see Sec. 3.2.1). With a built-in shaker from Brüel & Kjær ('type 4810') an additional periodic sinusoidal variation of the external force is realized, which is the dynamic part of the applied force. To run the shaker, a frequency generator ('Tektronix AFG3021B') and an amplifier ('Brüel & Kjær power amplifier ('type 2718')' – the matching device for the B&K shaker) were

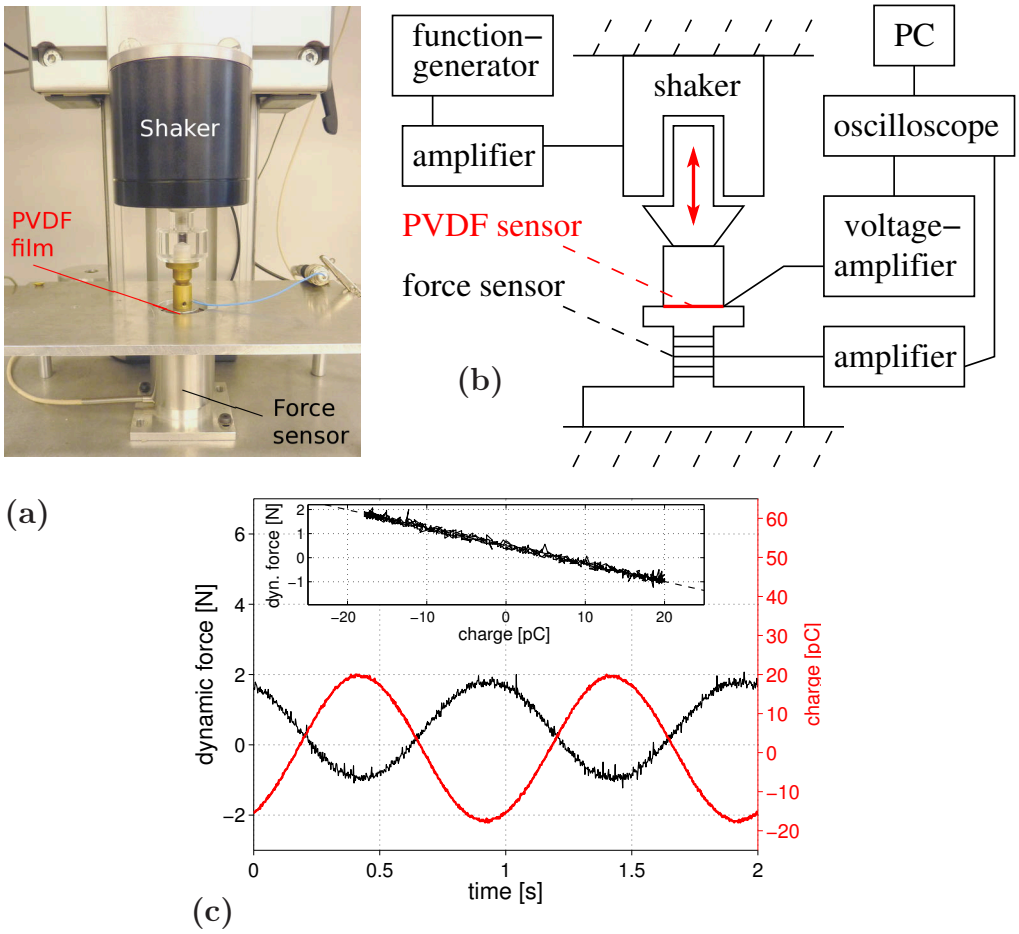

Figure 3.8: **(a)**: Picture of the dynamical d_{33} measurement setup. **(b)**: Dynamic force configuration for determing the d_{33} coefficient: With a constant initial pressure, a periodic sinusoidal force (produced by the shaker Brüel & Kjær ('type 4810')) generates a periodic electrical signal. Both signals are measured and analyzed by an oscilloscope, which plots the two parameters against each other. The resulting regression line gives a slope, being exactly d_{33} (see Eq. 3.9). **(c)**: Measured charge [pC] and force [N] captured with the dynamic force method in the big frame. The determination of d_{33} by averaging with a regression line in the inset frame. $d_{33} = 13.5$pC/N for this example.

included in the measurement setup. The force is recorded by the force sensor 'Burster – type 8435', which is located right below the PVDF sensor.

The overall, time-dependent applied force can be expressed by:

$$F_{dyn} = F_{amp} \cdot \cos(2\pi f t) + F_{stat} \tag{3.7}$$

Through the dynamic part of the force, the polarization of the piezoelectric polymer film is varying. This polarization change induces the generation of

compensation charges directly at the PVDF sensor surfaces (top and bottom). Due to the sinusoidal variation of the force, the charges appear also in an alternating manner:

$$Q_{dyn} = Q_{amp} \cdot \cos(2\pi f t) + Q_{stat} \tag{3.8}$$

By simply calculating the ratio of the amplitudes ΔF_{amp} and ΔQ_{amp} it is possible to determine the d_{33} coefficient immediately. Unfortunately, the force signal is typically hard to measure exactly, having a relatively large scatter. Performing an average of d_{33} by a linear regression between both parameters is an appropriate workaround for this noise problem (see Fig. 3.8c). The slope of the regression line is the d_{33} coefficient:

$$\Delta Q_{amp} = d_{33} \cdot \Delta F_{amp} \tag{3.9}$$

Both parameters (charge and force signal) recorded by their individual measurement devices were processed by the oscilloscope 'Gould Model 4094'. A Testpoint program determined the d_{33} coefficient from the regression line, calculated with the Marquardt-Levenberg method [Marquardt 1963].

3.2.2.2 Calibration Results

Initial pressure: The most delicate factor for the application of PVDF as a sensor. The main question is: How does the piezoelectric coefficient d_{33} behave under a changing static force on the PVDF sample and what means this for the subsequent measurements? Changing the static pressure on the PVDF sensor will result in a volume change of the amorphous phase of the PVDF, which is known as the 'dipole-density effect' [Sessler 1999a], i.e. the external force drives the internal molecular configuration out of equilibrium. The respective relaxation, which can be a multi-timescale process for other polymers, can be described for PVDF by just one typical relaxation time τ_r. If the relaxation behavior can be reconstructed or fitted, it is possible to compensate for this effect. The molecule configuration within the PVDF can be assumed constant, if the measuring time is $t_m \ll \tau_r$. But if the measuring time is $t_m \gg \tau_r$, relaxation effects could influence the d_{33} measurements and the subsequent instrument investigations. So the question arises in which magnitude will this effect perturbate the measurements ?

But first the static force dependence on the d_{33} coefficient is investigated, where the individual measurement time is put to $t_m \ll \tau_r$ to counter possible relaxation processes (For PVDF the relaxation time is in the order of $\tau_r \sim 100$h at room temperature [Oshiki 1976].) The fully sputtered PVDF film is placed in the measurement setup under constant initial force. The shaker

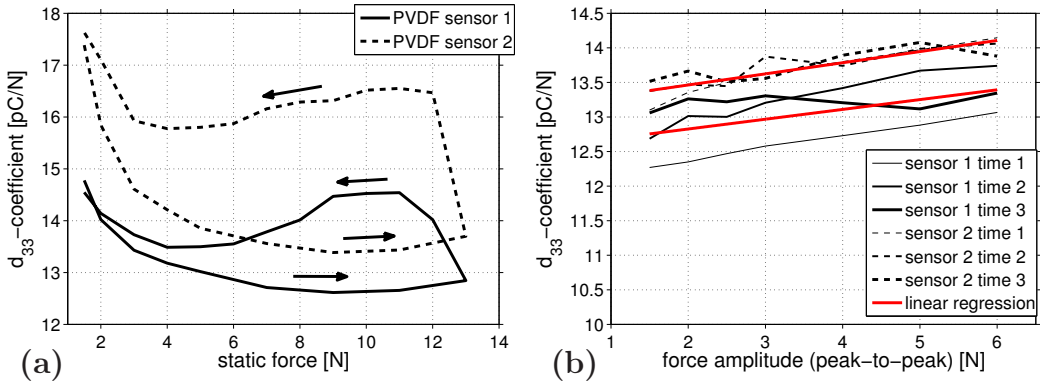

Figure 3.9: **(a)**: d_{33} coefficient hysteresis loop over the static force F_{stat}. The amplitude of the dynamic force was constant at 2N $\pm$0.1N (peak-to-peak). Indicated by the arrows, the increasing and decreasing of F_{stat} is documented. **(b)**: d_{33} coefficient vs. the dynamic force amplitude, where the static force was held constant at 6N $\pm$0.1N. Three independent measurements are obtained for each investigated sample at different times (black curves). The d_{33} behavior can be assumed as linear, indicated by the red regression lines, over this amplitude range. For both samples the same slope $m \sim (0.15 \pm 0.016)\mathrm{pC/N}^2$ was measured, justifying the linear regression.

generates a sinusoidal varying dynamic force $F_{amp} \cdot \cos(2\pi ft)$ additionally to the static force F_{stat} (see Eq. 3.7), which is produced by the adjustable screw. The resulting varying electric signal, recorded by an oscilloscope, is further processed by a computer, which determines the regression line between both parameters and the subsequently resulting slope – the d_{33} coefficient. To obtain an appropriate averaging, for each initial pressure value several measurements are carried out and the d_{33} coefficient is determined. The d_{33} outcome for the investigated sensors, shown in Fig. 3.9a, follows a hysteresis loop for increasing and decreasing static force, which is indicated by the inserted arrows. The amplitude of the dynamic part of the force is set to a constant value of 2N $\pm$0.1N (peak-to-peak). Initially, from 1N to 4N, the connection to the force sensor is not ideal by reason of a relatively large dynamic part of the force compared to the static force. This effect generates a 'threshold force' actually only for these measurements, where the measured force value is too small. Hence, a too high d_{33} value is determined in this range as a consequence.

Using exactly this data acquisition setup, this threshold effect becomes minimal in the range from 4N to 11N, indicated by the relatively constant d_{33} behavior. Unfortunately, the used measurement setup is only designed for static forces up to 11N. Any forces beyond that point will affect the accuracy

of the recording setup, especially the B&K shaker. That could result in a too high piezoelectric coefficient (as seen also in Fig. 3.9a for static force values beyond 11N), when the static force is not properly transfered to the force sensor. When the force is slowly released, the existing polymer configuration temporarily stays this way and begins to relax to its initial state. This will also end up in a seemingly higher d_{33} coefficient (see also Fig. 3.9a).

All investigated PVDF samples show exactly the same behavior, but on different initial levels. For each sensor, which will be used for further measurements, a separate d_{33} determination has to be made. The observed deviation in the piezoelectric coefficient can be explained by fluctuations within the polymer material and also by the size variation of the sputtered electrodes, caused during the sputtering process by the attached masks [Kappel 2011].

Excitation amplitude: An additional important parameter is the d_{33} dependence on the excitation force amplitude. During these measurements, the static force was held at 6N $\pm$0.1N. Shown exemplarily in Fig. 3.9b, two PVDF samples were independently analyzed at three different times. Their behavior can be appropriately described by a linear correlation, shown as the red lines. Both PVDF sensors have the same slope of $m \approx (0.15 \pm 0.016)\text{pC/N}^2$.

Signal-to-Noise Ratio: The signal-to-noise ratio (S/N ratio) [Guillaume 2006] was determined with the help of strings mounted onto the multichord and measuring the first harmonic of a tone with the fundamental frequency of $f_{\text{S/N}} = 200\text{Hz}$. The observed piezopolymer S/N ratio at this frequency is $L_p = 78\text{dB}$, representing a good S/N ratio.

3.2.2.3 Other notable parameters

Temperature and Humidity: The temperature variations within a single measurement run are not significant and are all in the range of one or two degree Celsius. The maximum temperature range considering several weeks did not extend below 20°C and above than 28°C. Exemplarily shown in Fig. 3.10b during the d_{33} long-term measurement, the temperature was monitored over the whole time range. It has been found that the variability of the temperature is rather small and has no significant correlation (see A.2.2) with the d_{33} coefficient behavior ($C_{\text{temp}} = 0.016$).

Another indicator that there is no significant temperature influence on the piezoelectric coefficient d_{33} is that pure PVDF, which was used in this investigation, is reasonably stable in temperature up to 80°C ([Harrison 2001, Sessler 1999a]). Considering all performed measurements, the temperature is within the range of 23°C to 27°C. Therefore, the temperature influence on the piezoelectric coefficient d_{33} can be fully neglected[3] [Tasaka 1981, Sessler 1999a].

In the same figure (Fig. 3.10b), the humidity of the measurement room is recorded as a possibly important parameter for the sensor performance, ranging from 37% to 57% relative humidity. Just as the temperature, the humidity has no effect on the sensor performance and the calculated correlation between the humidity and the d_{33} behavior tends to zero ($C_{\text{hum}} = 0.009$).

3.2.2.4 Characterization Results

Long term stability: Assuring a convenient sensor behavior during longer measurements, the d_{33} coefficient's long-term behavior is very important to quantify. Therefore, in the order of several days, the PVDF samples are held under constant pressure for the entire recording time. Different time ranges are considered: the short and long time scale, respectively. Fig. 3.10a and b, show the d_{33} coefficient for both ranges. Each data point represents an average of 10 individual measurements. In the short time scale (**a**), d_{33} can be assumed to have a constant value for the whole recording time. On the other hand, the long-term range (**b**) shows a certain decrease. This temporal coefficient behavior ($d_{33}(t)$) can be modeled via an exponential fit with an additional offset $d_{33,eq}$ [Oshiki 1976], which represents the already equilibrated value:

$$d_{33}(t) = d_0 \cdot e^{(-t/\tau)} + d_{33,eq}, \tag{3.10}$$

where τ is the Maxwell relaxation time of the polymer and d_0 denotes the difference of the initial d_{33} coefficient ($t = 0$) and the final value $d_{33,eq}$. $d_{33}(t)$ exponentially decreases to the offset $d_{33,eq}$, which is for every measured PVDF sensor about 96% of the initial value $d_{33}(t = 0)$. The offset $d_{33,eq}$ corresponds

[3] It should be mentioned at this point, that an additional co-monomer would decrease the stability of the temperature, dependent on the volume fraction of the add-on polymer. In [Furukawa 2001] this behavior with different volume fractions of PVDF is demonstrated. The co-polymer in this case is Trifluoroethylene, which is also the most commonly-used co-monomer for PVDF. The more co-polymers in volume fraction are included, the deeper is the Curie temperature, which represents the temperature sensor stability. The used PVDF sensors for this investigation, containing 100% PVDF and no co-monomer, have a high Curie temperature ($\sim$ 150°C), which is close to the melting temperature of $\sim$ 175°C

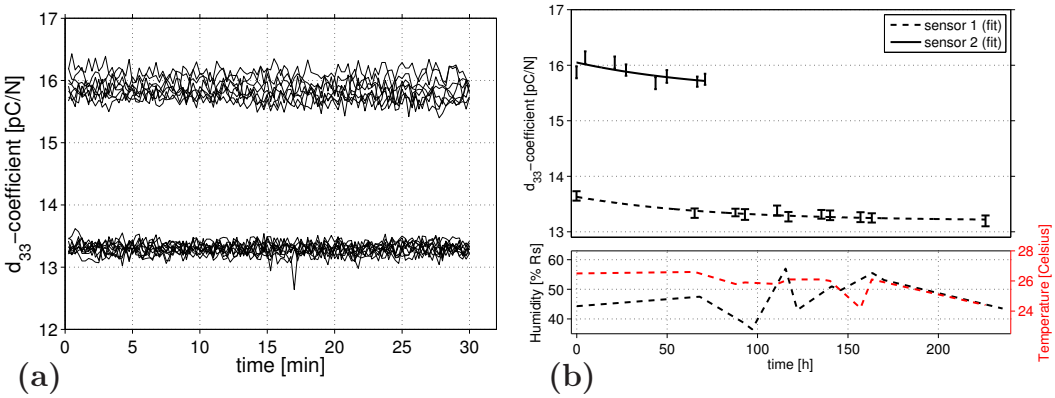

Figure 3.10: **(a)**: d_{33} coefficient over a short time range. Several measurements of two sensors are included in this plot and show a significantly flat d_{33} behavior over 30 minutes.
(b): A longer time range (up to 235 hours) for the d_{33} coefficient evolution in the upper plot. Fitted with $d_{33}(t) = d_0 * \exp(-t/\tau) + d_{33,eq}$ both curves are slightly decreasing towards the equilibrated value $d_{33,eq}$. Supplemental, the evolution of humidity (black) and temperature (red) are observed in the lower frame during the sensor 1 measurements. The calculated correlations of these parameters with the d_{33} evolution give values of $C_{\text{hum}} = 0.009$ for the humidity and $C_{\text{temp}} = 0.016$ for the temperature. Hence, no significant correlation has been found.

to the already relaxed molecule configuration; the relaxation time τ for both plotted curves (see Fig. 3.10b) have a value of $\tau \approx 77$h, which is in good agreement with [Oshiki 1976], who finds a value of about $\tau \sim 100$h for room temperature. For the investigated PVDF sensors 1 and 2, the equilibrated piezoelectric coefficients are $d_{33,eq_1} = 13.2$pC/N and $d_{33,eq_2} = 15.5$pC/N, respectively. During these measurements, the values for temperature and humidity are simultaneously recorded and have already been discussed in Sec. 3.2.2.3.

Taking into account that the investigation on the instruments include measurements, which last only few minutes at maximum, it is possible to conclude, that the d_{33} coefficient is constant during one recording. Furthermore, assuring a mounting of the PVDF sensors at least some days before the actual measurements begin, the coefficient behavior can also be assumed constant after this time. Even a data acquisition having the final value of the $d_{33,eq}$ coefficient, gives only a decrease of 4%, which is sufficiently small.

Frequency response: Fig. 3.11 describes two different measurement methods to investigate the frequency response of the PVDF sensors. The

first method (**a**) was performed with the dynamic force setup already used for the above described d_{33} measurements. Unfortunately, this setup does not support the data acquisition in the higher frequency range, by reason of measurement device vibrations. Between 1 Hz and 80 Hz this setup has its optimal working range. Beyond 80 Hz, a phase difference between the force signal and the recorded charge carrier appears, which is caused by the force sensor. Being too slow in comparison with the electric signal, the slope of the regression line becomes to steep, and therefore, the d_{33} value becomes too high. Furthermore, the standard deviation of the acquired data and thus its error also becomes too large (see Fig. 3.11a, the value for 160Hz). Regarding the wide field of possible applications (which is typically from 100Hz to 20kHz – the frequency range of audible sound), this limited frequency range is not ideal to measure the frequency response.
The second method also includes a shaker and a frequency generator, but an additional mechanical construction is used for the clamping of the PVDF sensor in combination with the shaker. Under constant static force the direct measurement of the PVDF frequency response was performed. For that, a sweep signal with the range of 100 Hz to 17 kHz having a time resolution of $t_r = 0.000021\text{s}^{-1}$ and a sweep time of $T_{max} = 20\text{s}$ was generated with the B&K shaker. This sinus signal has a constant peak-to-peak force value of $F_{\max} = 10\text{N}$ over the whole frequency range, which is due to the shaker. A respective voltage amplifier B&K Nexus (type 2692) enhances the resulting varying electric signal, which is detected by the sensors. The spectrum of two recorded time signals are depicted in Fig. 3.11b as the inset. Two perturbation effects can be observed as sharp minima at about 1190 Hz and 1320 Hz, both originated from the resonance frequency of the used calliper to clamp the measurement configuration. Showing that this is a calliper effect, the external force is varied, which results in a shift of the resonance effect. This ensures that this perturbation has nothing to do with a PVDF material property, but is due to imperfect measurement conditions. An additional effect can also be extracted from the plot, which has to do with the capacitor design of the 'sensor/amplifier' combination, which acts as a high-pass filter [Rabiner 1975], given by the following transmission:

$$\mathrm{T} = \frac{f/f_c}{\sqrt{1+(f/f_c)^2}}. \tag{3.11}$$

Here, f_c means the cutoff frequency, which is, related to the intensity, 3 dB below the maximum. T was fitted to both plotted graphs having a cutoff frequency of $f_c = 305\text{Hz}$. A high-pass filter deconvolution of the frequency signal will give a flat frequency response (maximum deviation of 6%, where the calliper resonances are excluded), plotted in Fig. 3.11b in the big frame.

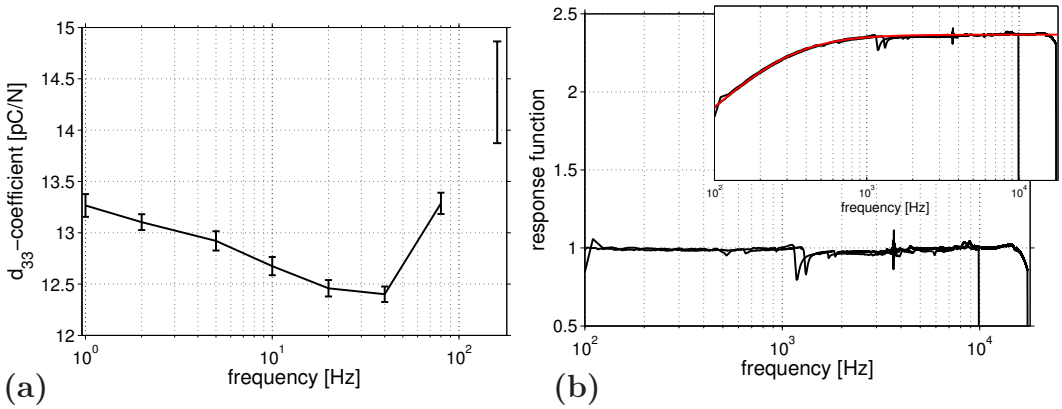

Figure 3.11: **(a)**: Measured frequency response gathered with the dynamic force measurement setup (see Fig. 3.8). Not ideal for a broad frequency range, but sufficient for 1 Hz to 80 Hz.
(b): Alternative method to check the independence of d_{33} from the frequency by measuring the resulting PVDF response function of a sweep from 100Hz to 17 kHz. A high pass effect occurs for the original data (see the inset), which can be modeled with the red graph (see Eq. 3.11). A deconvolution by this effect yields a flat PVDF frequency response function (bigger graph).

All subsequent PVDF recording signals are corrected for this high-pass effect.

Usually a further important parameter would be the thickness extension resonance spectrum of the polymer film, in particular the superelevation at the resonance frequency. But considering a thickness of about 30 μm, and the sound wave velocity within PVDF of $v_{\mathrm{PVDF}} = 2.3\mathrm{km/s}$ the lowest resonance frequency can be determined by:

$$f_r = \frac{v_{\mathrm{PVDF}}}{2 \cdot d_{\mathrm{film}}} \tag{3.12}$$

which comes from the condition that half of the wavelength of the structure-borne sound wave fits exactly to the thickness of the PVDF film. This yields a lower-limit resonance frequency of about $f_r = 37\mathrm{MHz}$, far beyond the parameter range in this investigation with a maximum of 20 kHz. Therefore, all measurements are located completely within the constant range of the mechanical resonance spectrum (see Appendix A.2.6 and [Möser 2010]).

Additionally, the piezoelectric resonance effect [Mellinger 2003] should be noted here, although its resonance frequency is even larger compared to the mechanical resonance. For corona charged PVDF with a thickness of 24 μm, a piezoelectric resonance of about 50 MHz was found [Kulek 2002], which is also far beyond the audible range.

parameter	value [unit]	comment
ε_0	$8.86 \cdot 10^{-12}$ As/Vm	physical constant
ε_r	~ 9	relative permittivity for β-PVDF ([Hahn 1985])
A	$3.6 \cdot 10^{-5}\,\mathrm{m}^2$ (Bechstein) $1.69 \cdot 10^{-4}\,\mathrm{m}^2$ (Multichord)	active surface area of PVDF sensor ($\pm$30% [Kappel 2011])
d_{33}	$(14 \pm 0.5) \cdot 10^{-12}\,\mathrm{C/N}$	measured piezoelectric constant
d	$(30.1 \pm 1.2) \cdot 10^{-6}\,\mathrm{m}$	thickness PVDF film

Table 3.3: Listed values, either calculated or constant, for the determination of the external dynamic force routed to the surface of the PVDF film.

3.2.3 External Dynamic Force

Having done the complete characterization and calibration of the PVDF sensors, the calculation of a dynamic part of the external force acting on the sensor plane can be determined. By configuration, there is no force contribution of a static part within the measurement signal. Certainly, this particular characteristic qualifies these thin polymer sensors as a data acquisition device for sound vibrations. The knowledge of relation Eq. 3.9 and the behavior of the piezoelectric coefficient for the investigated sensors gives the possibility of the direct determination of the dynamic part of the external force, where Eq. 3.9 marks the starting point:

$$\Delta Q_{dyn} = d_{33} \cdot \Delta F_{dyn} \tag{3.13}$$

Due to the fact, that eventually a voltage U, generated by the PVDF film, is measured, the well known relation $Q = C \cdot U$ will be further used. The two sputtered electrodes, which encase the dielectric PVDF, represent a capacitor with the respective capacitance C:

$$C = \varepsilon_0 \cdot \varepsilon_r \cdot \frac{A}{d} \tag{3.14}$$

at which A is the area with the acting force (see 3.2.1) of the gold sputtered polymer, d the film thickness, ε_0 the vacuum permittivity and ε_r the relative permittivity. The three formulas in combination yield an expression, which is practical for the measurement analysis:

$$\Delta F_{dyn} = \varepsilon_0 \cdot \varepsilon_r \cdot \frac{A}{d_{33} \cdot d} \cdot \Delta U \tag{3.15}$$

The values for the polymer accelerometers are listed in table Tab. 3.3.

With Eq. 3.15, the absolute value of the dynamic force can be calculated. All the following instrument measurements, recorded by the PVDF sensors,

are calibrated in this way providing the result in units of Newton [N]. A typical value for this investigation is $F_{Bechst.} \sim 0.3$N (Fig. 5.7) for the Bechstein measurements and $F_{Multich.} \sim 1.5$N for the multichord recordings. The obvious difference in the dynamic force is solely due to the different areas covered by the mounted bridges. For the multichord, the covered area of the bridge is smaller and due to the same excitation mechanism for both recording series, the dynamic force is therefore larger than in the Bechstein case.

3.3 Condenser Microphones

Since there is an extensive use of microphones in the present investigation, in particular capacitor microphones ([Eargle 2004, Ballou 2009, Wong 1997]), a description of the most important features is justified. But as a common standard technique, where the characteristics are completely known and provided by the microphone manufacturer Brüel & Kjær, the documentation about the functionality and the characteristics are provided in the appendix A.1.1.

3.4 Chapter Conclusion

The first part of this chapter introduces the acoustic characterization of the anechoic chamber in terms of dimension, absorption, soundproofing, and reverberation time. Knowing these parameters will yield reliable and secure airborne measurements within the recording room, which have been taken place for the multichord investigation described in the next chapter.

It was also demonstrated above that carefully prepared piezoelectric polymer sensors (which are produced from mono-axially stretched PVDF in this case) can be used as integrated force sensors to record body vibrations with minimal invasion of the investigated system. This recording procedure applies to many vibrational systems, such as the monitoring of buildings, vehicles, machinery, alarm systems, etc. There are enormous advantages in using these polymer materials: namely their relatively low cost and their minimal dimensions so that they can be used in large quantity without disturbing the monitored system.

Despite having many advantages, one fundamental challenge with polymers is their relaxation under external stress. Therefore, it is extremely important to understand and characterize the sensor response on short and long time scales. It was demonstrated that a careful calibration will take into account a slow drift of parameters. The piezoelectric coefficient d_{33}, representing the vertical electromechanical conversion, was determined with

respect to the following crucial parameters: initial force F_{stat}, amplitude of the dynamical force F_{dyn}, frequency response, and long-term stability. The exact knowledge of the sensor behavior under specific parameter variations provides the possibility of a secured and calibrated body-vibration measurement, which is shown in the next two chapters. Along with the airborne measurements of a conventional condenser microphone, statements can be made about the vibrational energy distribution during the excitation of the system.

Chapter 4

Multichord as a Conceptional Soundboard

The basic theory for some of the acoustic effects occuring in the sound generation of solid-state vibrations and the emerging dispersion relation was provided by the LCM model in chapter 2.1.4. A further evolution of this model towards an underlying obstacle pattern for the propagating material is provided in the first section.

The investigation of these theoretical effects is difficult when the particularly shaped sound board of an upright piano or even grand piano is considered – the eigenmodes heavily depend on the specific shape. However, a surface structured with regular ribs can be mapped to the soundboard. Therefore, it was decided to build a dedicated setup by a rectangular multichord, which is easily understood, cheap and well controllable. This multichord can be adopted as a simplified piano model and to render it as similar as possible to a real piano, the instrument will be equipped with all neccessary genuine parts important for the spectral radiation of the board. The spectral change of the propagating sound waves in the board (see additionally [Kappel 2010] for the multichord investigations) is measured by means of condensor microphones and state-of-the-art piezopolymer sensors, described in detail in [Kappel 2011] and in chapter 3.2.

The chapter goes on with the explanation of the construction, geometry and measurement setup of the multichord in Sec. 4.2. In Sec. 4.3, the acquired data and the respective results are presented. Finally, in Sec. 4.3.3, the data is fitted to the above-mentioned adjusted LCM model and discussed in detail.

4.1 LCM Model Projection to the Ribbed Soundboard

The LCM model (see Sec. 2.1.4) will be further developed and described in this section. This advancement of the model describes the structure-borne sound-wave propagation through a patterned material. This material should be infinitely extended towards one direction, assuming an asymptotic

situation. The bonding of the material is arranged in a row. This, in principle, can be summed up to a simplification as a quasi-1D system with unit cells (ribs with distance a) starting an infinite series with a periodic boundary condition. The next step in the model is a sound wave scattered forward and backward by the first obstacle (the first rib). This scattering process depends on the relative phase of the incoming wave and its wavelength, of course. The second rib will do the same, and so on.

Now consider a non-infinite series by a further evolution of the model to fit better the reality: a finite number of ribs $(N + 1)$ shall be infinitely heavy and infinitely thin, while the soundboard has a finite size of $N \cdot a$. Solving the model with the given boundary conditions yields standing waves with a wavelength given by the constraint $\lambda_n = 2a/n$, where n is a positive integer. These conditions describe obviously the only solution for this system. Furthermore, N-fold degenerate respective frequencies for an elastic membrane with $\nu_n = c(\nu)/\lambda_n$ are introduced, where $c(\nu)$ represents the speed of sound in dependence of the wavelength.

To advance the model, the weight of the ribs remains large but finite, which results in a coupling between the former independent individual inter-rib sections, described by a coupling constant ε. This also yields a removal of the former degeneration and consequently the frequency spectrum will consist of N separate eigenfrequencies having a band width of 2ε and located at the harmonics for the elastic membrane ν_n. Hence, an adaption was realized from an extended system including elasticity to a set of coupled oscillators with frequencies ν_n. Following the LCM model [Ashcroft 1976, Morse 1987, Ziman 1972, Kittel 1953], the equation of motion (including the harmonics of the elastic membrane ν_n) can be written down as:

$$\ddot{u}_j = -\nu_n^2 + \varepsilon(u_{j+1} - 2u_j + u_{j-1}) \tag{4.1}$$

with integer $j = 1, \ldots, N$ and u representing the displacement. Again, the coupling is restricted to the nearest neighbors only and the speed of sound is neglected. With the ansatz $u_j \sim e^{ik_j j/N}$, $k_j = 2\pi/\lambda_j$ and the periodic boundary condition $u([N + 1] \cdot a) = u(a); \qquad u(0) = u(N \cdot a)$, the frequency spectrum will include allowed 'pass bands':

$$\nu_j = \pm\,\nu_n \pm 2\varepsilon \sin(kj/(2N)) \tag{4.2}$$

In essence, located at each resonance frequency ν_n of the soundboard, a structure of 'pass-band' frequencies emerges, given by the dispersion relation in Eq. 2.7. Changing the boundary conditions to a fixed one would yield frequencies only shifted within the 'pass band'. Therefore, the result remains the same qualitatively.

The rib distance or the coupling could easily be varied by changing the respective entries of the parameters ν_n or ε. Theoretically, this would result in a shift of the individual frequencies in the 'band pass'. Even the complete destruction of the band structure can be achieved through a fully disordered system [Condat 1986, Crisanti 1993, Bayer 1993].

Since this configuration is fully symmetric, as shown by Eq. 4.2, the above-explained situation is clearly valid for positive and negative frequencies. Even though the negative frequencies are solutions to Eq. 4.2, they do not have any meaning in reality. This effect is linear and holds for any coupling. With an increase of the coupling factor, the sharpness of the peaks in the frequency spectrum will decrease, while the overlap of the sound waves between the inter-rib distances increases.

In the following, the limits of the model are discussed: The multichord used in the experiment has a finite length, thus imposing fixed boundary conditions. The finite size and mass of the ribs, the change in cross section of the soundboard, as well as the material imperfections, lead to deviations of the frequency response from the the above-discussed adjusted LCM model. The question arises, what are the observable effects in the spectrum concerning these imperfections? At least, one can expect a strong damping of frequencies in the spectrum, which means that these sound waves are not allowed to propagate through the material limited by the rib distances. They are reflected by the rib (acting as the scatterer) in such a way that the incoming wave interferes destructively with the reflected wave. As a result, large regions in the spectrum should be damped *and* bands of allowed frequencies – the 'pass bands' – should be observed, approximately within the intervals $[\pm\nu_n;\ \pm\nu_n \pm 2\varepsilon]$.

The specific eigenmodes of the studied multichord should be mentioned here as a short preview on the special structure of the investigated instrument (see Sec. 4.3). The two most important ones are L_{SB}, which is the first longitudinal mode and corresponds to the major part of the soundboard length, and L_{BR}, which is the second one in longitudinal direction and is marked by the distance between the excitation bridge and the end of the soundboard (see Fig. 4.6; see Fig. 4.2 for a complete description of the multichord dimension). Therefore, any generated spectral feature from the scattering could only appear *on top* of existing resonances ν_{SB} and ν_{RB} of the unperturbated (i.e. rib-free) resonance board. What actually can be expected from the measurements are peaks with respective band structure at about $\nu_{0,\text{long}} \simeq c/(2L_{SB})$ and $\nu_{0,\text{long}} \simeq c/2L_{BR}$ including all of their harmonics. Again, the configuration is fully symmetric, including left *and* right propagating sound waves. Hence, the banded scattering structure on the 'positive' side of the respective resonances $\nu_{SR,n}$ is completely mirrored on the

'negative' side of $\nu_{SR,n}$. That can be expressed with $\nu_{SR,n} \pm \nu_k$, $k = 1, ..., N$. This is exactly the spectral behavior that will be described in the results section.

There is an alternative perspective of the theoretical explaination of this effect. So far, the board with infinite-mass ribs ($\varepsilon = 0$) is the starting point of the consideration. Then, ε becomes small, allowing to emerge the 'pass band' effects in the frequency spectrum. The alternative view comprises a situation, which is closer to the experiment. Assume an unperturbated board with no specific modes and where the correlation is $\varepsilon = \infty$. For an increasing number of attached ribs, the unperturbated modes, which are the allowed resonances additionally to the main board resonances, begin to emerge. This description is closer to the experimental situation due to the subsequent mounting of the ribs, and perfectly analogous to the picture above. Both considerations result in a band of natural symmetric eigenfrequencies on top of the fundamental resonances due to the dimensions of the soundboard.

4.2 Construction & Experimental Setup

The multichord, intended as a conceptional soundboard, was constructed for several reasons. On the one hand, it is possible to test the newly calibrated & characterized PVDF sensors (see Sec. 3.2.2) on a 'real' vibrating and sound-radiating object and on the other hand to optimize the procedure. With the multichord recording experiences, the handling of the sensors, mounted in a genuine piano (see Sec. 5) becomes easier and more familiar. Nevertheless, a multichord is a stand-alone instrument worth to investigate possibly occuring physical effects. Due to the simplified geometry, which has significant difference to a real piano, scattering effects should be on a different level compared to the piano setup, which is much more complex. To investigate the unique sound-wave propagation characteristics between both vibrating constructions and even differences between certain construction steps is one of the major aims. The main objective is the investigation of the spectral characteristics of the sound propagated in and radiated from a soundboard with mounted ribs.

A rectangular multichord (1.2 m x 0.28 m) fully equipped with boundary bridges (for a defined length of the strings), the excitation bridge, tuning pegs and piano strings was constructed (see Fig. 4.1). Commercially available wood glue was used for the adhesive bonding of the individual parts. This is quite common even for real pianos. Ribs are significant for the piano and its sound radiation (discussed in 2.1.3). A number of equidistant ribs (seen also in Fig. 4.2) was successively placed under the soundboard. After

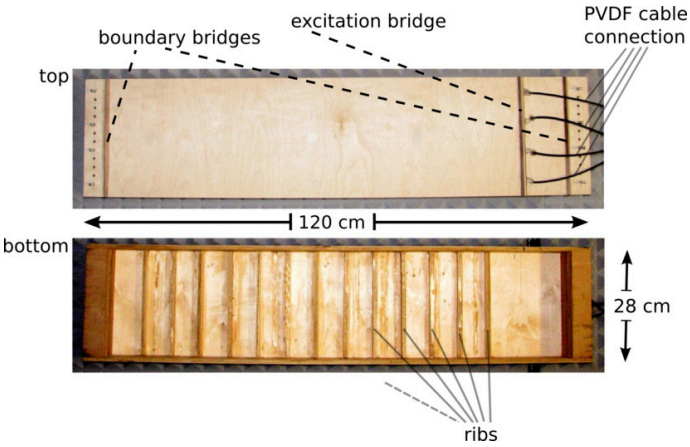

Figure 4.1: Top and bottom view of the constructed multichord without mounted strings, but with ribs on the bottom side of the soundboard. All the measurements were performed without strings and with a defined pulse at the excitation bridge. The picture contrast is enhanced for a better representation of the individual parts.

each rib mounting, the effect on the sound radiation was measured. The ribs were placed in equal distances to each other such that the outermost rib has the same distance to the excitation bridge, which is installed on top of the soundboard.

The material for the multichord soundboard was conventional maple plywood, arranged and glued in alternating layers respective to the grain. Although this is obviously not the case for the soundboards of grand and upright pianos (which have massive wood plates with very special properties)[1], anisotropy in the sound radiation and propagation is avoided along length and width. The exception is, of course, for the additional rib mounting, which acts as a restriction for the sound propagation. For the investigation, the ribs had equal distances of 7 cm, 9.8 cm, and 14 cm (see **b1** in Fig. 4.2), starting from the bridge. Therefore, at one side of the multichord one non-equidistant length exists (**b4**). The most important spacings for the instrument measurements are (see Fig. 4.2): Height **b2** = 7.8 cm, boundary thickness **b3** = 5 cm and the distance excitation bridge – boundary bridge **b4** = 11 cm.
The experimental procedure was the following: starting with an 'empty' (rib-free) soundboard; then step by step increasing successively the number of the mounted ribs until the board is filled with the maximum number of ribs possible (13, 9, and 6 ribs for 7 cm, 9.8 cm, and 14 cm distance respectively). The B&K condenser microphone, measuring the airborne radiation, was placed exactly over the middle of the resonance board, i.e. perfectly

[1] Also the high price of a genuine piano soundboard was part of the decision to use maple plywood.

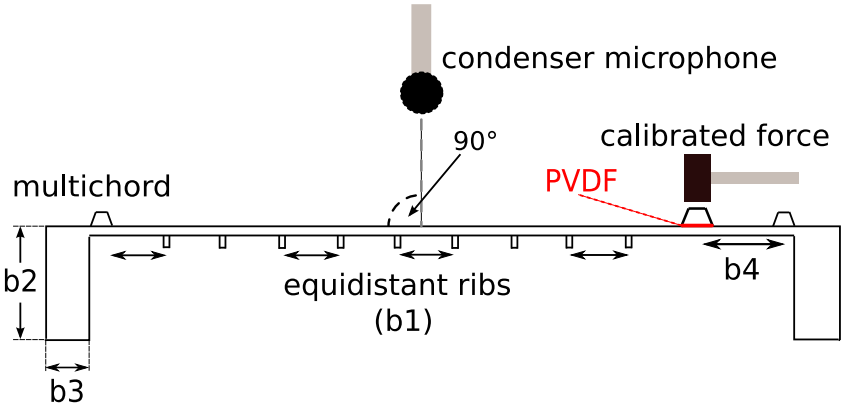

Figure 4.2: Overview of the multichord setup with mounted ribs (**b1** represents the distance between ribs). The hammering device is sketched on the right-hand side and excites the resonance board via the sound bridge with a single pulse. The airborne soundwaves were recorded by a B&K condensor microphone right above the arrangement and by PVDF piezopolymer sensors glued between the bridge and the board. Further dimensions are: height **b2** = 7.8 cm, boundary thickness **b3** = 5 cm and distance from excitement bridge to boundary bridge, **b4** = 11 cm.

perpendicular to the board's surface[2]. This microphone location provides the complete soundboard radiation (see Sec. A.2.8), because the radiation of a board has a specific characteristic – a dipole radiation pattern [Russell 1998], which varies over the angle between the recording device and the surface of the sound radiator. The distance to the middle of the soundboard was 62 cm.

PVDF mounting: The complete description of the PVDF sensors, their composition, preparation, characterization and calibration can be found in chapter 3.2.2. The piezoelectric coefficient for the recording transducer in the multichord investigation is $d_{33_{\mathrm{PVDF}}} = 16.3\mathrm{pC/N}$. The PVDF sensor was mounted between the sound bridge and the resonance board with a defined pressure of 55 kPa. Normal wood glue, as it is used also for the construction of professional piano instruments, was used for the adhesive bonding.

The further setup comprises an amplifier for the PVDF-sensor signal ('Brüel & Kjær Nexus signal conditioner type 2692'), the external soundcard 'MOTU PCIex 24 I/O' and the processing PC. Moreover, the sensors have to be connected to the Nexus amplifier with an additional cable. Therefore, silver conductive paste was used for the adhesive bonding between the cable and the electrodes of the solid-state sensors.

[2]Other angles were tested, but the 'rectangular recording' of the microphone was re-established.

4.3 Rib Scattering

4.3.1 Results

The main objective in this section is to investigate scattering effects in the sound propagation (time and frequency domain), which the mounted ribs will create. The best case would be the measurement of scattering features ('mirrored pass bands' around the eigenmodes of the multichord) in the frequency spectrum, as it was described in the theory section (see Sec. 4.1). To make a clear statement about their influence, it is advantageous to run the investigation by only changing one parameter between single recordings, i.e. performing a measurement after each single rib mounting. By finishing the data acquisition, it will be possible to compare:

- the solid-state soundwaves in the soundboard vs. the airborne sound (PVDF sensor vs. condenser microphone)
- the sound wave propagation and the occuring scattering effects for increasing rib number (same distances)
- the sound generated for equal rib number (different distances)

As an introduction, a spectral rib effect typical for this investigation is shown. A comparison between a 'clean' (rib-free) and a fully mounted soundboard is shown in Fig. 4.3, for both measurement techniques: PVDF sensor (bottom) and condenser microphone (top). Depicted in red is the case of 13 ribs, having a distance of 7 cm to each other, while the black curves where measured on the rib-free soundboards. All the spectra (also the subsequent in this investigation, if not indicated otherwise) are normalized to have equal total power. It should be noted, that the complete frequency range is plotted (even the negative range on the left side); the spectral pass bands of both ranges being solutions (see Eq. 4.2) for the differential equation of motion (see Eq. 4.1). The linear chain model (Sec. 2.1.4), developed and applied in solid-state physics, will be used for this case and will explain the pass-band effects in the spectrum.

The data depicted in Fig. 4.3 show an obvious change in the radiation characteristic depending on whether if there are ribs mounted or not. But while a clear scattering feature in the spectrum appears when the ribs are attached, it is probably more important that whole frequency ranges are suppressed.

This dramatic spectral effect (unperturbated pass-band structures and surpressed modes) is introduced by the presence of ribs. Finding this spectral rib characteristic so clearly, justifies the idea of comparing the ribbed

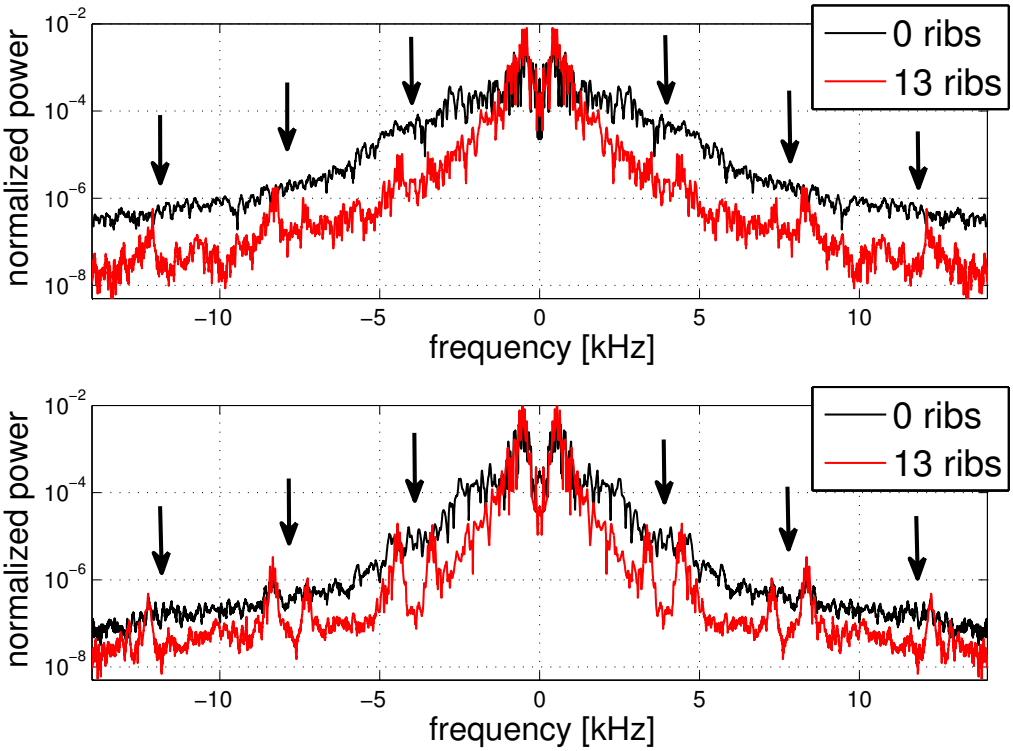

Figure 4.3: Spectral comparison (positive and negative !) of the soundoard without ribs (black) and with mounted ribs (red). *Top*: Condensor microphone. *Bottom*: PVDF sensor measurements. The arrows show the positions of the developing frequency pass bands. A clear banded structure can be observed for both signals, but the signal recorded by the piezopolymer sensor is much more pronounced with deeper suppressions. All spectra are normalized by the total spectral power.

soundboard with a crystal lattice to some extent. Obviously, due to the simple configuration of the rectangular multichord, the described emerging characteristics are very well pronounced. In a typical piano, the geometry is much more complex and the boundary conditions (even difficult to determine for the multichord) are almost impossible to find out. A closer look on the spectra reveals a minor effect for the airborne sound radiation. Although the band-pass effects are still observable and quantifyable for the microphone, the PVDF sensor signals show much more pronounced frequency structures. The reason could be that, due to the different impedances of the propagating materials (air and wood), the airborne radiation of the soundboard was smoothed at their transition. For a better comparison between the microphone and the PVDF-sensor signals, both spectra were plotted in Fig. 4.4, separated by a factor of 100. Again the 13-rib case is plotted. The soundwaves reflected on the left side of the multichord (see Fig. 4.2)) are stronger damped due to

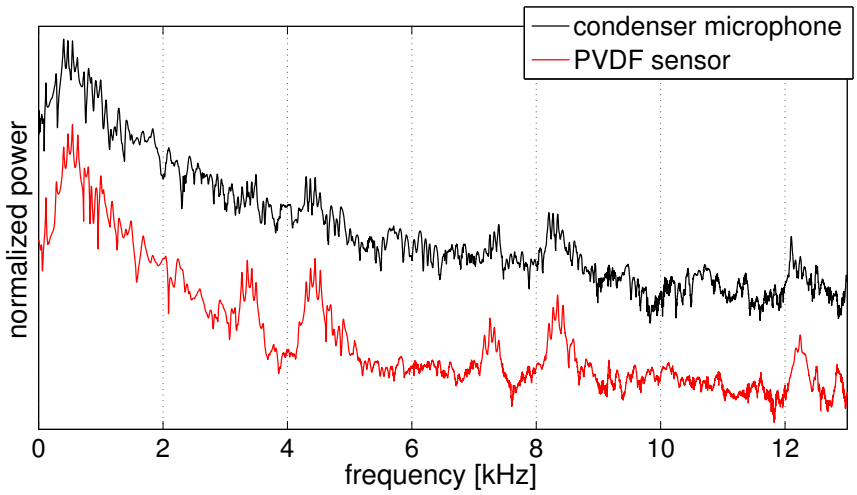

Figure 4.4: Direct comparison (only the positive frequency range) of the piezopolymer (red) and microphone (black) measurements, with 13 mounted ribs. The curves are normalized and seperated by a factor of 100 for a better comparison.

the longer propagation length. This is clearly reflected by the less pronounced 'left hand' pass bands, nicely shown in Fig. 4.4, where both pass bands at $\sim$ 8kHz have different intensities.

Repeatability and Point of Attack of the Soundboard Excitation In the first part of the measurements, mounted strings were excited by controlled hammering (only gravity was the driving force). But then there was, of course, always a preference of the frequency modes matching the harmonics of the strings. Since *all* relevant frequencies should be excited at once with the same intensity, the strings were removed from the multichord, and a pulse excitation (also only driven by gravity) was performed. The most convenient results were obtained by directly hitting the bridge. This also corresponds to the musical excitation, because the piano bridge is the 'soundboard entrance' for the string-generated soundwaves. Nevertheless, to check the occuring differences by changing the excitation location, the point of attack was changed from central on the bridge to decentral right within a void space between two ribs. There are observable differences, which are displayed in Fig. 4.5a. No deviations larger than 3% in peak position are found, instead one can expect large changes known from a piano string. While the bridge attack shows some additional structure apart from the pass bands, the direct soundboard attack turns out to be smoother. The multichord bridge excitation was performed always in the same manner, meaning that a specific mass was falling always from the same height, developing a defined momentum. The reproducibility

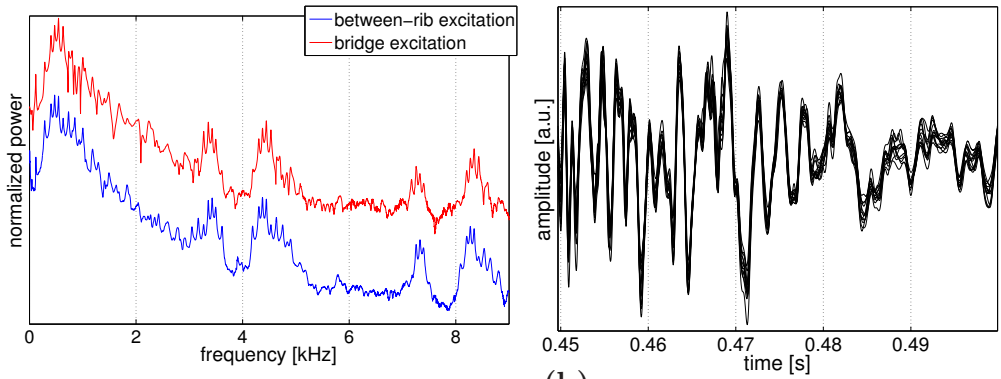

(a) (b)

Figure 4.5: (**a**): The different excitation points with their spectral differences. The bridge excitation (which is used throughout this investigation) as the red curve, and the decentral excitation located in the middle of a void rib space as the blue curve. The plots are also normalized and separated by a factor of 100 for a better comparability. Beside that the pass-band structures of interest are basically identical, the bridge excitation appears musically relevant, if the piano excitation is considered.
(**b**): 15 independent excitations at the bridge of the multichord covering the same time range. An almost perfect correlation ($C = 0.995$) between these curves secure the reproducibility of the excitation.

of this excitation method is nicely shown in Fig. 4.5b, where 13 different excitations on the same location at the bridge are shown for the same time range. An almost perfect correlation of $C = 0.995$ (see A.2.2) proves that the pulse excitation is almost perfectly reproducible, which is essential for the measurements. Furthermore, the excitation amplitude was measured in a series of successive experiments, where the amplitude was found constant with slight deviations. As we focus on the frequency analysis, the amplitude of the hammering shall not be discussed here.

The next step in this investigation is to take a closer look at the positions of the band edges and to analyze the underlying mode structure of the soundboard. Examining a rib-free soundboard, two eigenmodes could be found: first the mode of the vibration along the string direction (which will be then the 'ribbed' part of the soundboard) and second the mode of the vibration along the length **b4** (see Fig. 4.6 and Fig. 4.2) on the other side. Hence, the frequencies should be located at about $\nu_{1,n} = c/(n \cdot 2L_{SB})$ and $\nu_{2,n} = c/(n \cdot 2L_{BR})$. Unfortunately, the frequencies are hard to identify, because the boundary conditions of the soundboard are not well defined (neither completely fixed, nor completely free). Since the material parameters

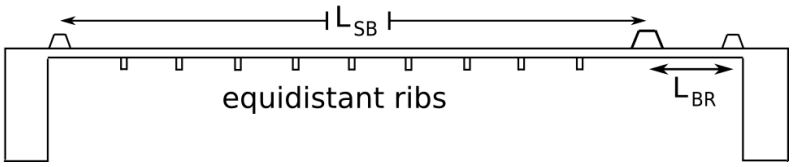

Figure 4.6: The most important longitudinal modes of the investigated multichord – L_{SB} and L_{BR}.

are not known exactly either, the determination of the eigenmodes is left to the measurements. To calculate the resonant frequencies, one needs the sound velocity in the rib-free soundboard. With the help of two accelerometers, manufactured by Brüel & Kjær, which are commonly used, the sound velocity within the board was determined. There are two different kinds of velocities: the group velocity, which combines all frequencies within a wave, and the phase velocity, which includes one single frequency. The excitation was performend by a single pulse, including all possible frequencies. Therefore, knowing the distance between both accelerometers and the measured time delay of the excitation, the group velocity can be determined. In the case of a 'rib-free' soundboard, the velocity was $v_{0\,\mathrm{ribs}} = 1145\mathrm{m/s}$. The 'ribbed' soundboard exibits a value of $v_{13\,\mathrm{ribs}} = 773\mathrm{m/s}$. Hence, the sound velocity is reduced if ribs are mounted. The intuition is fully confirmed: Including scatterers will hinder the propagation of the sound wave, yielding a reduced sound velocity. With the known lengths $L_{SB} = 0.99$ m and $L_{BR} = 0.11$ m (see Fig. 4.6), the resonant frequencies can be determined as $\nu_{1,1} = 578$ Hz and $\nu_{2,1} = 5205$ Hz. In the measured spectrum of the 'rib-free' soundboard the main characteristics appears between 250 Hz and 1050 Hz, which is, in very good agreement with the resonant frequency $\nu_{1,1} = 578$ Hz of the model. The other resonant frequency $\nu_{2,1} = 5205$ Hz from the model was not observed.

Given the assumptions above, 13 peaks within a pass band should be found. Actually only 10 peaks are well distinguishable (see Fig. 4.7) due to the relatively simple modeling with LCM, where the ribs act as the masses and the void spaces between the ribs act as the springs. The findings nevertheless are quite good and very convincing. It should be noted, that the frequencies near the pass-band edges are sensitive to any perturbations and can fall out of the band easily. This leads to a strong damping which makes them probably hard to find in the frequency spectrum.

The second pass band is found in the frequency range from 4150 Hz to 4865 Hz, the third from 8065 Hz to 8765 Hz and the forth from 11950 Hz to 12665 Hz. The spectrum reveals no higher pass band, which means that they are probably damped. Taking a closer look to the exact peak positions from the measurements and comparing these between the different bands, one finds, that these positions are *exactly* the same, only shifted by $\nu_2 = 3900$ Hz, which

fits perfectly the fundamental frequency of the multichord concerning the length $L_{BR} = 0.11$ m and the measured sound wave velocity $c = 773$ m/s. This effect is nicely demonstrated in Fig. 4.7, where again the 13-rib case, measured with the PVDF sensors, is plotted. Shifting the second, third, and fourth band (the higher harmonics of the fundamental frequency ν_{BR}) for positive frequencies by $m \cdot \nu_2$, $m = 1, 2, 3$ ('right hand' pass bands) results in a very convincing coincidence as demonstrated in the figure. For negative frequencies $-m \cdot \nu_2$ ('left hand' pass bands) the result is also very convincing, but with a disappeared band for $m = 3$, and an already vanishing band for $m = 2$. That can be explained by a stronger damping at higher frequencies and that the sound waves travelling in the negative direction (which are represented by the 'left peaks' of the pass-band structure; see Fig. 4.4 at $\sim$ 8kHz where both structures have different intensities) are more damped compared to the 'right peaks'. The 'left structure' sound waves are scattered many times within the soundboard and have a longer propagation distance until they return to the recording point, which is the PVDF sensor mounted beneath the bridge.

It turned out that the effect of a successive increase of the rib number marks another important evolution, which is plotted in Fig. 4.8. Here, for two rib distances (14cm (*left*) and 9.8cm (*right*)) the evolution of the emerging pass bands is demonstrated. Starting from the bridge, a new rib was mounted 14 cm (or 9.8 cm or 7 cm) away from the last one, until the soundboard was fully covered with 6 ribs (or 9 ribs or 13 ribs). The model predicts a new peak for each newly attached rib, building eventually a pass-band structure.

Looking at Fig. 4.8a, which shows the case for 6 ribs and a distance between them of 14 cm, reveals for 2, 4 and 6 ribs the respective 2, 4 and 6 peaks, which are marked by the arrows. This peak behavior holds for all bands in the spectrum. This clear demonstration shows a good agreement with the qualitative understanding of the setup configuration. Furthermore, similar spectral changes are also observed for other rib distances (see Fig. 4.8b), but not as pronounced as for the 6-rib case. What about the exact pass-band positions ? The model predicts peak positions at $m \cdot \nu_2 + \nu_1 \pm 2 \cdot \varepsilon \sin(k_j j/N)$. Unfortunately, only a qualitative coincidence can be observed, for example for the second band, where the individual peaks have been found at the frequency positions: 4254 Hz and 4351 Hz (2 ribs); 4202 Hz, 4286 Hz and 4361 Hz (4 ribs); 4120 Hz, 4175 Hz, 4248 Hz, 4327 Hz and 4395 Hz (6 ribs). But also shown in Fig. 4.8, there are no additional obvious features in the spectrum resulting from the resonant frequencies $\frac{c}{2 \cdot 0.14\text{m}} \simeq 2760$ Hz, and $\frac{c}{2 \cdot 0.098\text{m}} \simeq 3943$ Hz.

Another aspect of the investigation is the variation of the rib distance and the comparison of measurements with an equal number of ribs, which is plotted in Fig. 4.9 for a distance of $d_1 = 14$ cm and $d_2 = 9.8$ cm, respectively.

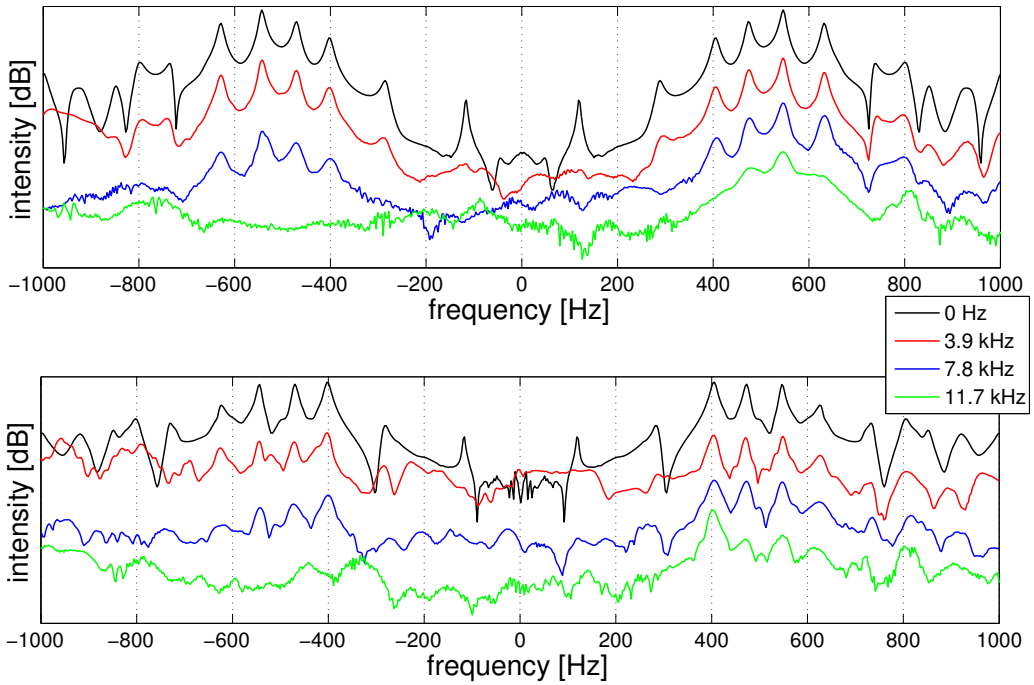

Figure 4.7: Structure comparison of the shifted pass bands measured at the multichord. *Top*: PVDF sensor beneath the bridge, and *bottom*: microphone measurement.
The first band structure (−1000 Hz to 1000 Hz) is shown as the black line; the second structure shifted by 3900 Hz depicted as red curve right below; the third band shifted by 7800 Hz (blue) and the forth band with a shift of 11700 Hz (green). Independent of the number of the mounted ribs and the distance between them, the shift is always $m \cdot 3900$ Hz, $m = 1, 2, 3$. The coincidence of the individual peaks (e.g., at ±280Hz, ±400Hz, ±460Hz, ±540Hz etc.) within the specific bands is highly significant. The red, blue and green curves are enhanced by a factor of 100 for a better comparability.

Looking at the peak positions, actually only little changes can be observed. The basic structure of the pass bands remains constant.

Finally, the lifetime of the pass-band modes is also discussed. Therefore, a time-dependent frequency analysis with short time slices of 5 ms has been performed. It can be concluded from Fig. 4.10, that the above-mentioned 'pass bands' have significantly longer decay time within the instrument. Considering the airborne sound measurements, this effect can also be observed, without being that clear. To investigate this lifetime behavior in particular, the decay factor γ is determined for all frequencies in the next chapter.

In conclusion, frequency 'pass bands' with a bandwith of 2ε were found

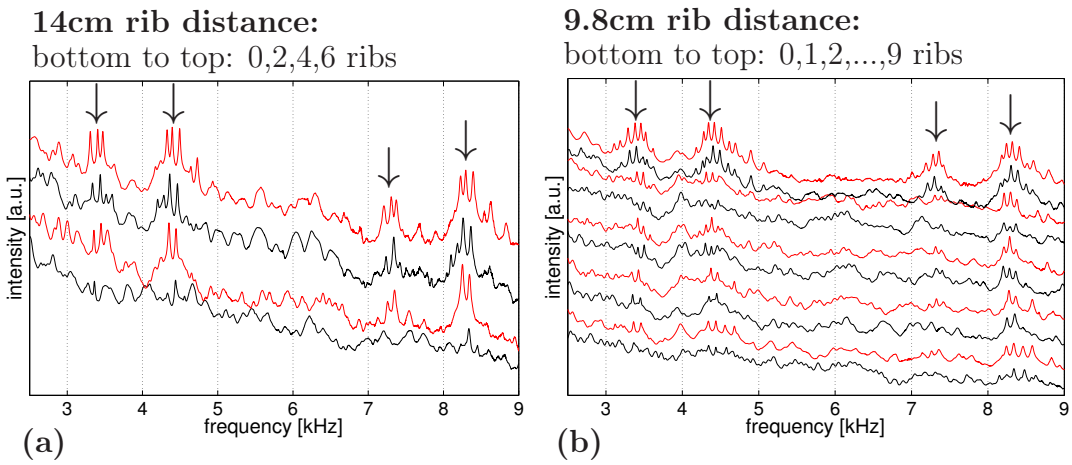

Figure 4.8: Successive mounting of ribs on the soundboard for different inter-rib distances, **(a)**): 14 cm and **(b)**): 9.8 cm distance. The rib number increases from zero (bottom curve) to the maximum possible number – by one for the 9.8 cm distance and by two for the 14 cm distance. The arrows indicate the emerging frequency pass bands. Especially for **(a)** the evolution of the single peaks are nicely recognizable. For a better comparison, all curves are separated by a factor of 10.

at the position of one of the resonant frequencies of the soundboard. The particular pattern or rather the band structure is exactly repeated for the 'higher' harmonics.

4.3.2 Frequency-dependent Damping Factor

The decay of a tone generated by a piano is complicated as explained by [Weinreich 1977]. The different decay times of different piano notes are also very nicely demonstrated therein. For the evaluation of the tone quality and length generated by a piano, it is of major importance to investigate the early decay of a tone. Therefore, it is necessary to determine the damping factor of the tone. While the above-mentioned investigations ([Weinreich 1977, Wogram 1980]) focus on the vertically matching impedance between the string and the soundboard, this investigation highlights the effect, if only a soundboard and no strings are involved. This setup demonstrates the generic decay ability of the soundboard without taking the strings into account.

For each frequency data point the damping factor γ is calculated. This was done via a fitting of the intensity decay:

$$I = I_0 \cdot e^{-\gamma t} \tag{4.3}$$

where I represents the intensity, I_0 the initial intensity, t the time and γ the damping factor. For the fitting, a time-dependent frequency spectrum

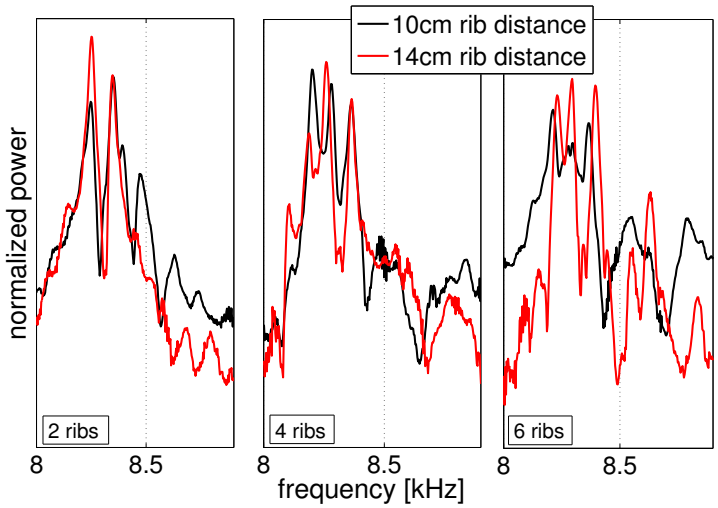

Figure 4.9: PVDF spectral comparison for equal rib number (*left* – 2 ribs; *middle* – 4 ribs; *right* – 6 ribs) with different rib distances (red – 14cm; black – 9.8cm). The third pass band (8 kHz to 8.9 kHz) is shown. Curves are normalized to spectral power.

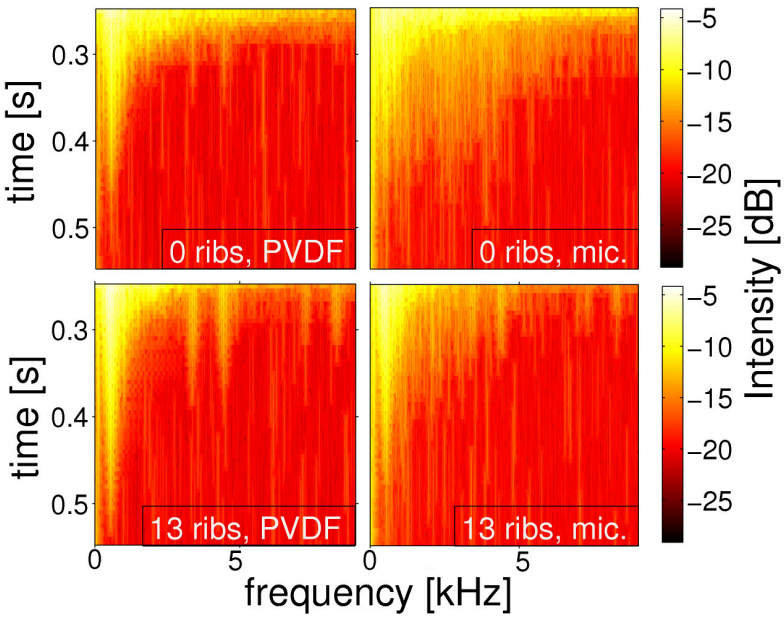

Figure 4.10: Time-dependent frequency spectrum of the resonance board with 0 ribs (**top**) and with 13 ribs (**bottom**). The soundboard is excited once and the decay of the signal is observed by the piezopolymer (**left**) and the microphone (**right**).

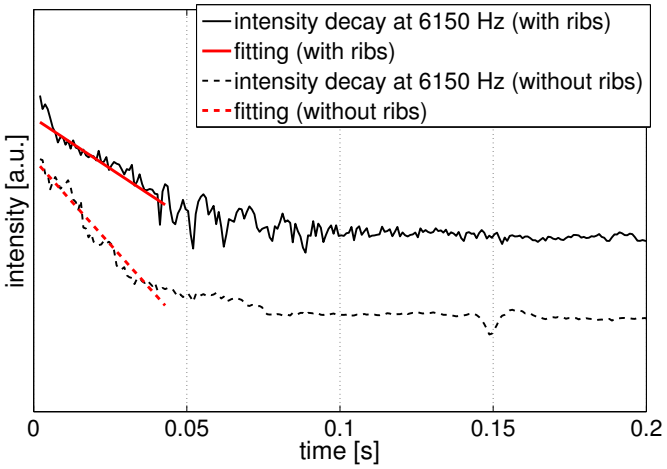

Figure 4.11: Demonstrating the algorithm for the determination of the damping factor at a certain frequency. The plotted curves are separated by a factor of 10 for a better comparability. Shown is the case for 6150 Hz. The decay with ribs and without ribs is fitted with Eq. 4.3. Comparing the fits yields the difference in the damping factor.

was calculated (e.g. Fig. 4.10). An exemplary calculation is performed in Fig. 4.11 at 6150 Hz, including the difference for the damping factor with ribs and without. The determined values for γ were $\gamma_{\text{none}} = 156.21/\text{s}$ and $\gamma_{\text{ribs}} = 92.71/\text{s}$, meaning a faster intensity decay without ribs, compared to the 'ribbed' case.

This analysis is extended consequently to the audible frequency spectrum as depicted in Fig. 4.12. As can be seen from the graph, the damping factor and the respective decay factor vary drastically with frequency. Consistently, a drop in the damping factor between 3 kHz and about 10 kHz can be seen – the soundboard radiates longer in this range if the ribs are attached. This effect becomes more pronounced, when a larger number of ribs are mounted to the soundboard.

4.3.3 Comparison: Scattering Model vs. Experimental Data

Using the adjusted LCM model explained in chapter 2 and the section above, the theoretical peaks of the pass bands will be fitted to the measured peak positions. Therefore, the ribs represent the masses in the model, while the spaces between the ribs represent the springs.

The acoustic dispersion relation (see Eq. 2.7) is given by

$$\omega_k = 2 \cdot \omega_0 \cdot \left| \sin\left(\frac{\pi}{2} \cdot \frac{n}{N}\right) \right| \tag{4.4}$$

ω_k represents the frequency of mode $k = (2\pi n)/(aN)$ with a as the rib distance, ω_0 is the fundamental vibrating frequency of the soundboard. n

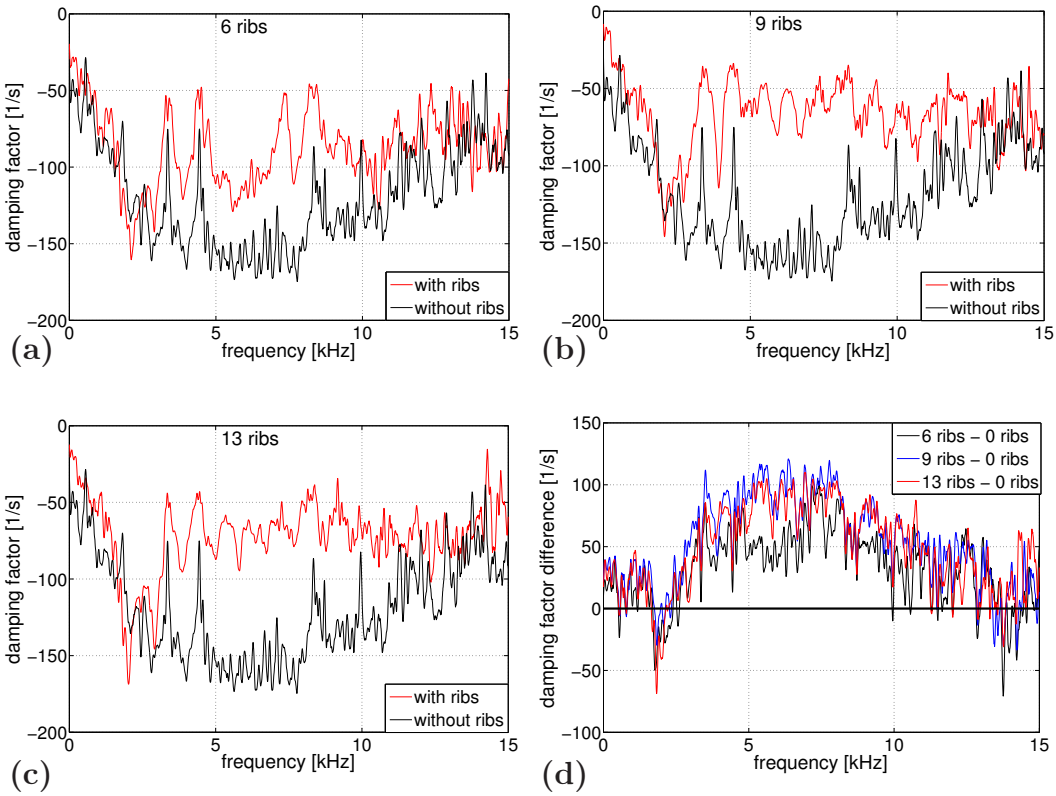

Figure 4.12: Damping factor for different rib numbers 6, 9 and 13 compared to the respective damping factor with 0 ribs. The difference between these factors are given in (**d**). There is a significant drop of the damping factor in the range of about 3 kHz and 10 kHz, when the ribs are attached to the soundboard. If the ribs are mounted, the soundboard radiates for a longer time, due to the smaller damping factor. With different intensities, this effect is completely independent from the rib number attached to the soundboard. But there is, also independent from the final rib number, an increase of the damping around 1 kHz. The rest of the damping-factor spectrum does not change very much with a variation of the rib number.

denotes the actual numbering of the ribs and N gives the total rib number. Knowing Eq. 4.4 and the determined peak positions of the measured spectrum provides the opportunity to justify the application of the adjusted LCM model. A fit of the equation of the acoustic dispersion relation (Eq. 4.4) to the real data gives the possibility to determine the vibrating length of the soundboard L_{SB} (see Fig. 4.6). The fitting procedure will yield the fundamental frequency ω_0 of the resonance board and was performed with a weighted Marquardt-Levenberg algorithm (see [Marquardt 1963] and Appendix A.2.1), where the weight was derived from the peak height of the

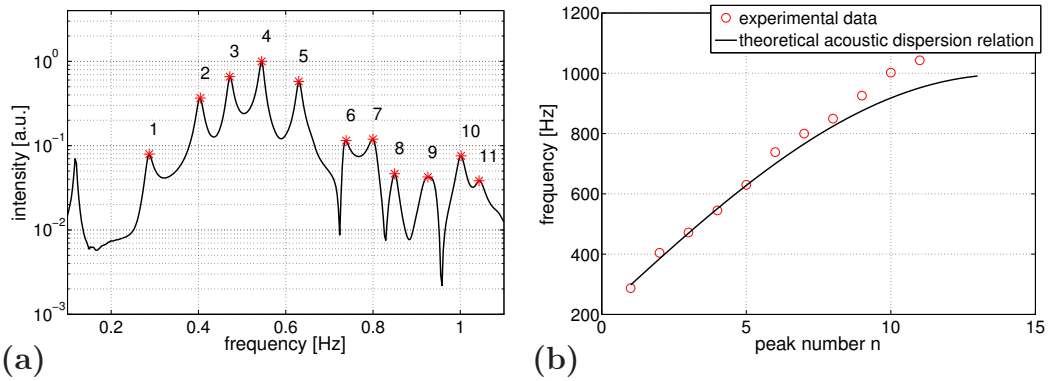

Figure 4.13: **a**): Pass band peak detection of the measured spectrum for the '13 ribs' case. The result of the peak detection is plotted as the red asterisks. **b**): The fitted LCM acoustic dispersion relation (black graph) in comparison to the pass-band peaks of the recorded spectrum. The last points of the acoustic relation fall apart due to the performed weighted fitting. But the fit works very well for the clearly distinguishable peaks up to number eight. Again, the '13 mounted ribs' case is shown.

'band-pass' frequencies (see Fig. 4.13a for the case with the 13 mounted ribs). The fitting yields a fundamental frequency of $\omega_0 = 393$Hz for the soundboard.

Figs. 4.13b and 4.14 show the obtained results from the fitting procedure in detail, where the positions of the theoretical peaks (marked with the red circles) are in very good agreement with the actual data of the '13 ribs' case (black curve). Due to the large coincidence between the higher harmonics of the scattering structure (see Fig. 4.7), the model can also be transfered to these specific peak positions, which was actually done in Fig. 4.14 up to the fourth order. Although, there were no frequency structures observed at about 16 kHz (due to the damping), the theoretical positions are indicated. The direct comparison (for the '13 ribs' case) between the theoretical and experimentally determined peak positions are plotted in Fig. 4.13b showing a significantly high agreement up to peak number eight.

For further analysis, the sound velocity within the soundboard, which was already mentioned above, will be needed again: The 'rib-free' soundboard exibits the velocity of $v_{0\,\mathrm{ribs}} = 1145$m/s, while the soundboard with the 13 mounted ribs has a value of $v_{13\,\mathrm{ribs}} = 773$m/s. With these parameters one is able to back-calculate the vibrating soundboard length, given the sound velocity of the '13 ribs' case, via:

$$v_G = \lambda \cdot \omega_0 \qquad \rightarrow \qquad \lambda = 2 \cdot L_{SB} = v_G/\omega_0 \tag{4.5}$$

where v_G is the group sound velocity, λ the wavelength, ω_0 the fundamental frequency, and L_{SB} the vibrating length of the soundboard.

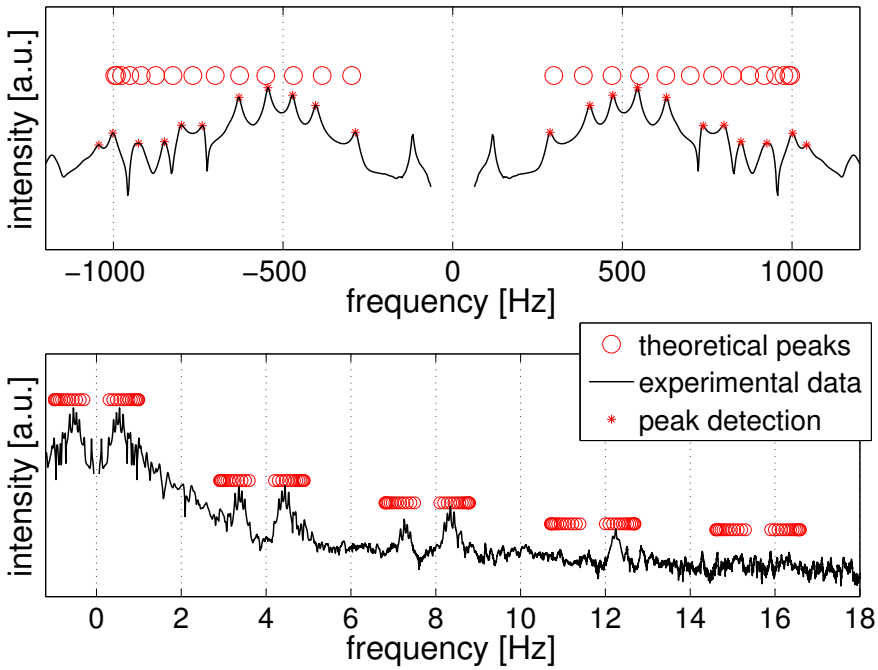

Figure 4.14: The fitted theoretical peaks (red cicles) from the passband (LCM model) in comparison with the peaks of the experimental data shown for different frequency ranges. *Top*: A close-up for the identification of the individual peaks (-1.2 kHz to 1.2 kHz). *Bottom*: The broad range to show the position of the other pass bands in comparison with the theoretical peak locations (1.2 kHz to 18 kHz).

Knowing Eq. 4.5, the sound velocity $v_{13\,\mathrm{ribs}} = 773\mathrm{m/s}$ and the fundamental frequency $\omega_0 = 393\mathrm{Hz}$ will provide the length of the vibrating soundboard via back-calculation, which is $L_{vibr} = 0.98\mathrm{m}$. This is in very good agreement with the 'rib-mounted' vibrating length of the resonance board with $L_{SB} = 0.99\mathrm{m}$ (Whole multichord length (1.2m) minus boundaries (2x0.05m) minus distance between boundary bridge and excitation bridge ($L_{BR} = 0.11\mathrm{m}$; see Fig. 4.2)), justifying the use of the adjusted LCM not only for the understanding of the scattering effects of the sound-wave propagation in patterned materials, but also for the exact position of the emerging peaks in the spectrum.

Also a qualitative discrimination of the acoustic dispersion relation between the different rib distances could be drawn, which is plotted in Fig. 4.15. The specific relations for rib distances 7cm (blue), 9.8cm (red), and 14cm (green) are compared, while the inset of the same figure shows the theoretical trend for the mounted 13 ribs. A successively better agreement between theory and measurement can be observed with an increasing rib number. This result also fully confirms the intuition, because *many* obstacles are closer to the LCM model, which was actually proposed for the acoustic

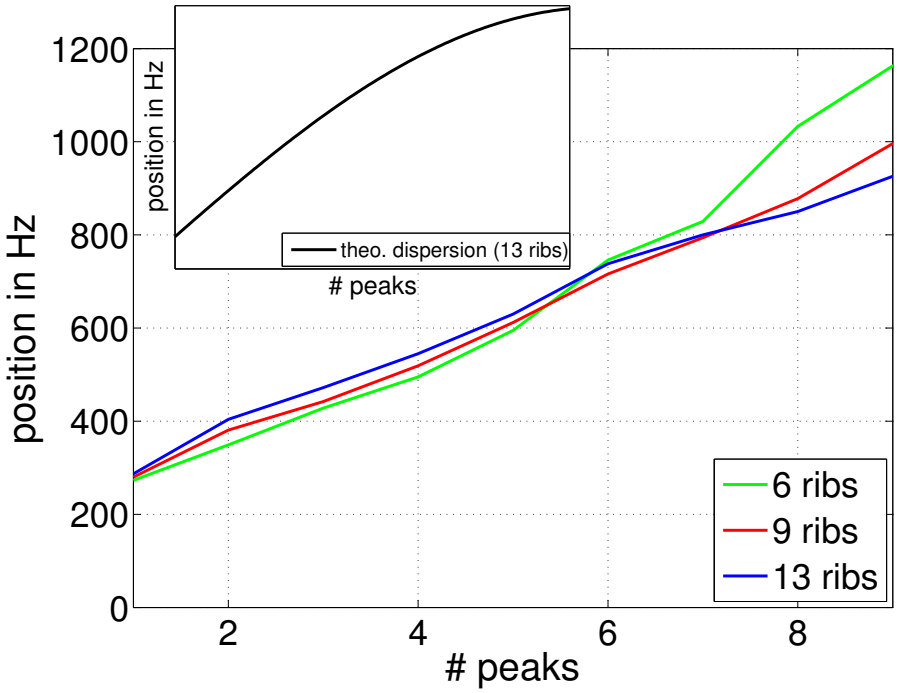

Figure 4.15: *Large plot*: The different measured dispersion relations for the various rib distances: '6 ribs' – green, '9 ribs' – red, '13 ribs' – blue. *Inset*: The theoretical dispersion relation for the '13 ribs' case

dispersion relation on an atomic level.

Possible alternatives to the LCM, such as FEM (finite-element method) simulations, were not employed due to the time-consuming procedure. The LCM is a simple approach indeed, but due to the very good agreement of the peak positions between this model and the measured data with variations smaller than 3%, it is sufficient to make predictions about the positions of the emerging peaks.

4.4 Chapter Conclusion

In this chapter, the dramatic effect obstacles mounted on a multichord soundboard may have on the propagation of sound waves is demonstrated. To some extent, the results hold for any vibrating body with a regularly structured surface which radiates sound when excited. From general arguments, it follows that the spectrum of the multichord and the piano has many similarities as can be seen later in the 'Bechstein piano' chapter 5. Nevertheless, the piano soundboard geometry used is different and the modal structure is not as clear as on the rectangular multichord soundboard.

A specifically designed setup with minimal parameter variations was used

to have full control of the reproducibility of the results[3]. The number of ribs mounted and the spacing between the ribs were varied, and as a result, a heavy influence of even few ribs on the sound radiation and propagation has been found. The position of the passing frequencies found are the eigenmodes of the structured soundboard, which correspond with qualitative band theory (see Sec. 4.1), analogous to the theory of phonons in solid state physics – the so called LCM model. These certain eigenfrequencies are determined experimentally and verified theoretically. Knowing the positions of the pass-band peaks, the 'length' of the chain (which is the 'ribbed' vibrating length of the multichord) could be back-calculated.

The question arises how to circumvent the unwanted suppression or increase of certain frequencies, if ribs must be mounted to strengthen the soundboard mechanically. As explained in the next chapter for the piano, a structured band can be easily eliminated, if disorder is introduced into the system.

[3]The exception was the sucessive mounting of the ribs.

Chapter 5

The Real Piano: Bechstein 'Zimmermann Z.3/116'

One of the main aims of this investigation was the application of the PVDF sensors in a *genuine* instrument. A cooperation with the piano manufacturer 'C. Bechstein Pianofortefabrik' [Bechstein 2005] provided the opportunity to mount these sensors in one of their pianos.
The structure of this chapter is as follows: First, the design and construction of an upright piano is explained (Sec. 5.1). Then, every step of the assembly of the piano is described. The PVDF sensors are mounted within the Piano structure from the beginning of the assembly process.

5.1 Piano Assembly

The upright piano '*Zimmermann Z.3/116*' (see Fig. 5.1), which is the smallest model in the Zimmermann series, manufactured by 'C. Bechstein Pianofortefabrik', was the investigated object. The assembly of a piano[1] comprises several individual construction steps (see Tab. 5.1 and the additional pictures in Fig. 5.3b&c and Fig. 5.4 for each stage), using a combination of automated machinery and hand crafting. Following the listing in Tab. 5.1, the bridges (treble and bass bridge) on one side and 11 ribs on the other side are glued to the empty soundboard, which has a dimension of width x height x depth: 146cm x 93cm x 0.8cm (step **no. 1a & 1b**). After a drying time of about two hours, the back of the board was varnished (step **no. 2**). To provide stability and the basis for further mountings, the whole soundboard was attached at a wooden frame (step **no. 3**). With the final varnishing on the front side (step **no. 4**), the moisture level within the board is fixed. The next step in the course of the construction process comprises the attachment of the metal frame, which includes the mounted strings already (step **no. 5**). The last two steps[2] in the piano assembly are the installation

[1] The description of the construction relies solely on personal experience of the investigator. A detailed reference of the typical assembly workflow has not been found. This expert knowledge was acquired during several visits of the Bechstein manufacturing center.

[2] Beside the individual tuning of the strings.

Figure 5.1: The piano '*Zimmermann Z.3/116*' – the model which was investigated. Photo: By Courtesy of C. Bechstein Pianofortefabrik.

no.	construction step	comment
1a 1b	mounting the bridges on soundboard gluing the ribs to the soundboard	normally done in one step
2	varnishing the soundboard rear side	reducing water absorption
3	framing the soundboard	stability and piano basis
4	varnishing the front	stopping water absorption
5	mounting the strings and metal frame	the actual instrument
6	assembly of the hammering mechanism	string excitation
7	apply the piano faceplate	-

Table 5.1: The manufacturing workflow for an Bechstein upright piano. Except the first step, where 1a and 1b is done usually at once, the evolution of the built-up is typical for an upright piano. See Fig. 5.3b&c and Fig. 5.4 for the intermediate states.

of the hammering mechanism (step **no. 6**) and the placement of the wooden cover (step **no. 7**). The final state of the instrument can be described by its width of 1.51 m, height of 1.16 m, depth of 0.59 m and weight of 236 kg [Bechstein 2005].

5.2 Mounting the Polymer Sensors

Using thin polymer sensors (see Sec. 3.2.1 for preparation and characterization) provides a minimally-invasive measurement technique of body vibrations generated in an instrument. From the constructional perspective, the exact mounting of the sensors is the most interesting point, and the question of the sensor placement in the piano arises. Knowing that the bridges (treble and bass bridge – see Fig. 5.2a) are the transition material between strings and soundboard, makes this particular interface one of the most interesting positions of the sensors. The transition from the strings to the bridge is not very practical for sensor placement, obviously due to the small area involved, where the strings touch the bridge. Furthermore, the strings are attached to the soundboard at a late stage of the workflow. Covering as many assembly steps as possible, especially the installation of the ribs, the PVDF sensors need to be placed between the bridge and the soundboard. The bonding of these two parts is normally done in one single step using a hydraulic press. Given that the radiation differences of the soundboard with and without ribs is pivotal for the present investigation, the usual and traditional work flow of the piano assembly was modified especially for these measurements by splitting the procedure in two parts: i) mounting the bridges onto the board and ii) after a short time window, mounting the ribs in their positions. The above-mentioned time window of two hours was the maximum time suggested by the responsible piano maker. An overstepping of the time limit could possibly result in a deformation of the board due to moisture loss and the loss of back pressure normally generated by the ribs.

The design of the sensors was chosen with having electrodes in one single direction due to constructional reasons, especially for these measurements, where the 'string-sided' area seen from the bridge is completely covered by attached strings after step 5 (see Tab. 5.1). That would make it extremely difficult to reach the 'string-sided' electrode for the connection to the amplifier during the individual construction steps of the piano.

The question remains, how to fix the sensors between the wooden parts. This construction aspect had to be decided in favor of not changing the typical workflow again. For that reason, typical wood glue on water basis, used for all adhesive bondings during the whole assembly, was utilized for the sensor mounting (see Fig. 5.2b). This decision is additionally supported by the very small water absorption of Kynar-PVDF of 0.03% over a time of 24 hours [MSI 2006]. Only lasting few hours for the full hardening of the water-based glue, the influence of water on the PVDF during the measurements can be mainly neglected.

Due to practical reasons and the recording hardware, the number of the

(a)

(b)

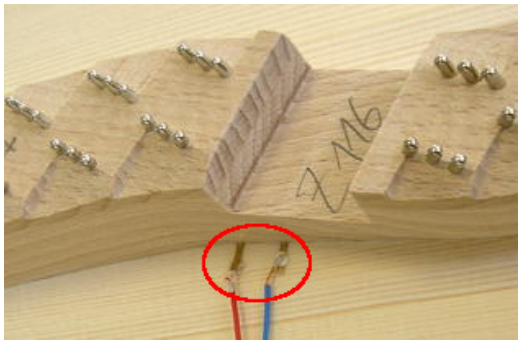

(c)

Figure 5.2: **(a)**: The stand-alone bridges of the upright piano (*left*: treble bridge; *right*: bass bridge). **(b)**: The bridge covered with wood glue. The PVDF sensors are already in place, right before the brigde is glued onto the soundboard. **(c)**: Finally after the mounting: The sensor electrodes (red ellipse) can be seen very nicely.

body vibration sensors is limited to six. The selected locations (see Fig. 5.3a as the filled red squares) were chosen for several reasons; on the one hand to cover as well as possible the whole length of the treble piano bridge and therefore a wide range of the tone pitch, and on the other hand, to be able to record differences that possibly occur, if a sensor is placed right under a rib or not (see Fig. 5.3, especially the locations of PVDF1 / PVDF2 and PVDF4 / PVDF5). After the polymer sensors are fully installed, only two small parts of the sputtered electrodes (top and bottom) are sticking out as the 'only evidence' of the sensors' presence. The possible PVDF perturbation of the sound propagation within the piano can also be mainly neglected by reason of the matching impedances of wood and PVDF [MSI 2006, Bucur 2006]. Given a width of 3cm for the treble bridge, the piezoelectric sensors (see Fig. 3.7b) are placed symmetrically with regard to the sputtered rectangular area, i.e. the middle of the squared electrode surface is located right under the middle

of the bridge.

To reduce the complexity of the recording process and due to the lack of further hardware channels, a possible sensor mounting under the bass bridge was left out. Nevertheless, possible follow-up measurements on different pianos should include this location for the enlargement of the investigated area.

Once the PVDF sensors are in place between the treble bridge and the soundboard, they have to be connected to an amplifier, which is the 'Brüel & Kjær Nexus signal conditioner type 2692'. This is the same device used for the multichord measurements. Again, the amplified signal is then processed by the external soundcard 'MOTU 24 I/O'. To implement the connection between the Nexus and the PVDF sensors, additional cables need to be attached to the electrodes of the sensor. Silver conductive paste was used for the adhesive bonding between cable and electrode. This special connection is shown in Fig. 5.2c.

5.3 Results

Due to the temporally tight connection between the assembly of the piano and the measurements, the investigation of the Bechstein soundboard had taken place in a conference room at the Bechstein factory in Seifhennersdorf, Saxony. Thus, no special absorption and damping of the room could be realized, i.e. the recordings of the condenser microphone should be handled with care, due to less damping of the reflected sound waves. The data of the PVDF sensor measurements have no restrictions towards the room characteristics, because they solely measure body vibrations.

To have the possibility to compare the Bechstein measurements with the recordings from the multichord, the excitation procedure needs to be the same. Not only that the excitation occurs at the bridge, but even the mass by which the single pulses are produced has to be identical. The locations of the excitation points at the Bechstein soundboard are labeled as green circles in figure Fig. 5.3a. These specific locations on the treble bridge follow the idea of a wide area range and also have the intention to investigate the differences if a rib is underneath a stimulus point or not. Also, the reproducibility of the excitations are demonstrated very well in Fig. 5.5 with 12 independent incidents shown in the same time range.

It should be noted, that while former soundboard measurements are done for one single construction step (exemplarily: soundboard with ribs, bridges and wooden frame, but without cast-iron plate strings [Suzuki 1986] or full piano with damped strings [Moore 2006]), the present investigation fully

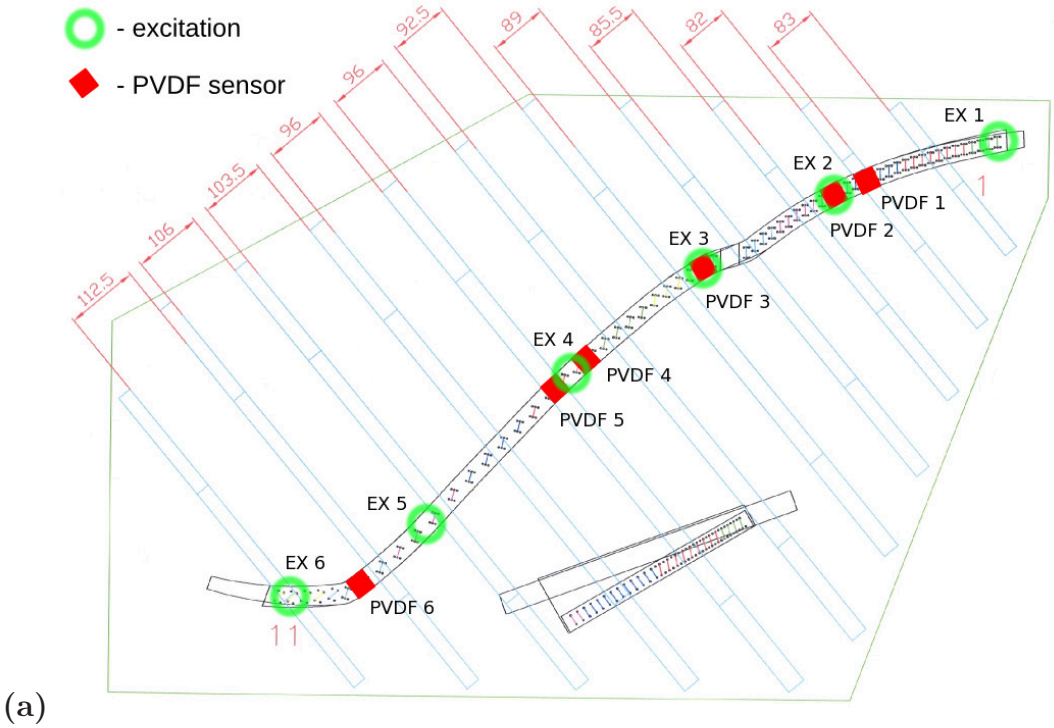

(a)

(b)

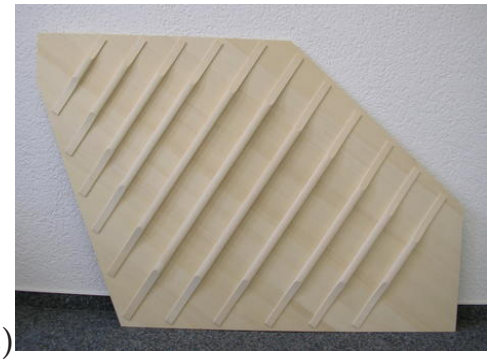

(c)

Figure 5.3: **(a)**:Design drawing of the Bechstein 'Z.3/116' soundboard, including all parts on the front and back; units given in [mm]. Also depicted in the graph are the excitation points at the bridge (six green cicles) and the positions of the PVDF sensors (six red squares). The numbers 1 and 11 clarify the rib numbering. **(b)**: Front side of the soundboard with the PVDF sensors already mounted in their respective positions. **(c)**: The same for the rear side of the soundboard including the bonded ribs.

(a)

(b)

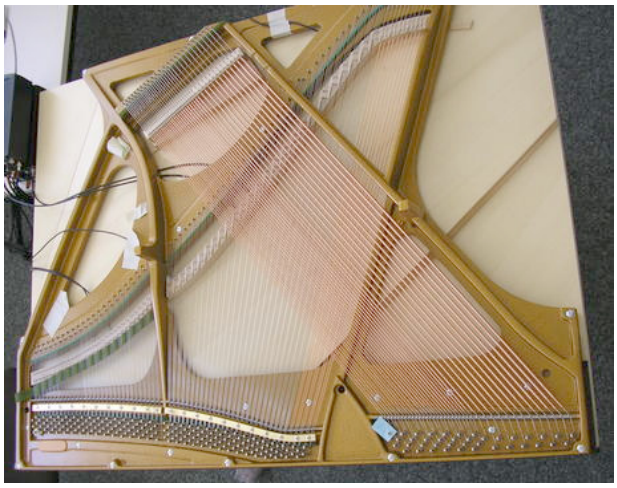

(c)

Figure 5.4: The front **(a)** and the rear side **(b)** of the soundboard after the wooden frame was attached. **(c)**: The piano construction with the strings already mounted.

comprises all construction steps necessary for the piano assembly.

Since the PVDF sensors are connected with silver conductive paste to the Nexus amplifier during an individual run of the measurements, they have to be disconnected from the Nexus afterwards for the further assembly of the piano. The adhesive bonding is firmly attached, but it is possible to lever the conductive paste from the electrode surface. It needs a high level of dexterity not to remove parts of the sputtered electrodes. In the course of the measurements the PVDF sensors are connected and disconnected from the amplifier six times during the individual recording runs. Unfortunately, sensor 'PVDF2' got broken after the front side of the soundboard was varnished, due to the successive removing of the electric connection from the conducting

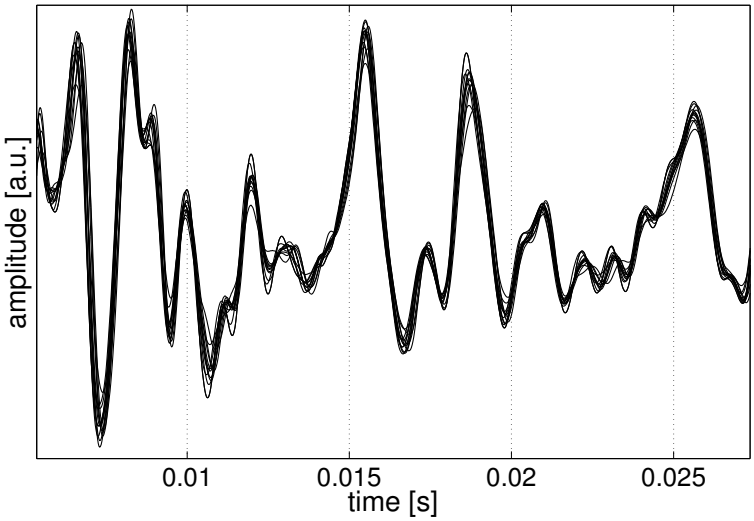

Figure 5.5: 12 different excitations for the same time range (0.006 s to 0.027 s), demonstrating the repeatability of the excitation mechanism.

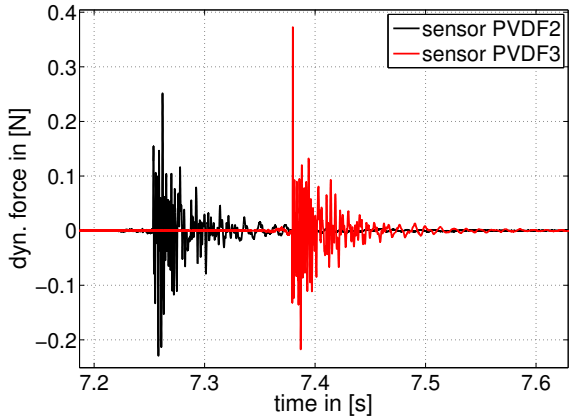

Figure 5.6: One individual excitation recorded by two different PVDF sensors – 'PVDF2' and 'PVDF3'. The location of the excitation in this case was 'EX 2' (see Fig. 5.3a), which is situated exactly above 'PVDF2'. This demonstrates that the maximum amplitude is not neccessarily related to the initial amplitude. Details in the text.

layer. Since the metal frame with the strings are in place (step 5 in Tab. 5.1), it is more practical in the further assembly process to keep the connection to the PVDF sensors permanently. This will also prevent further damage of the electrodes.

5.3.1 Pulse Amplitude

An important and interesting aspect of the measurements is the evolution of the dynamic force amplitude at the bridge-soundboard transition and the question of its rib dependency. Therefore, the maximum amplitude for each excitation and for each PVDF sensor was determined. Measurements show that the initial amplitude is *not* mandatorily the overall maximum amplitude. As one takes a look at Fig. 5.6, this behavior is exactly demonstrated.

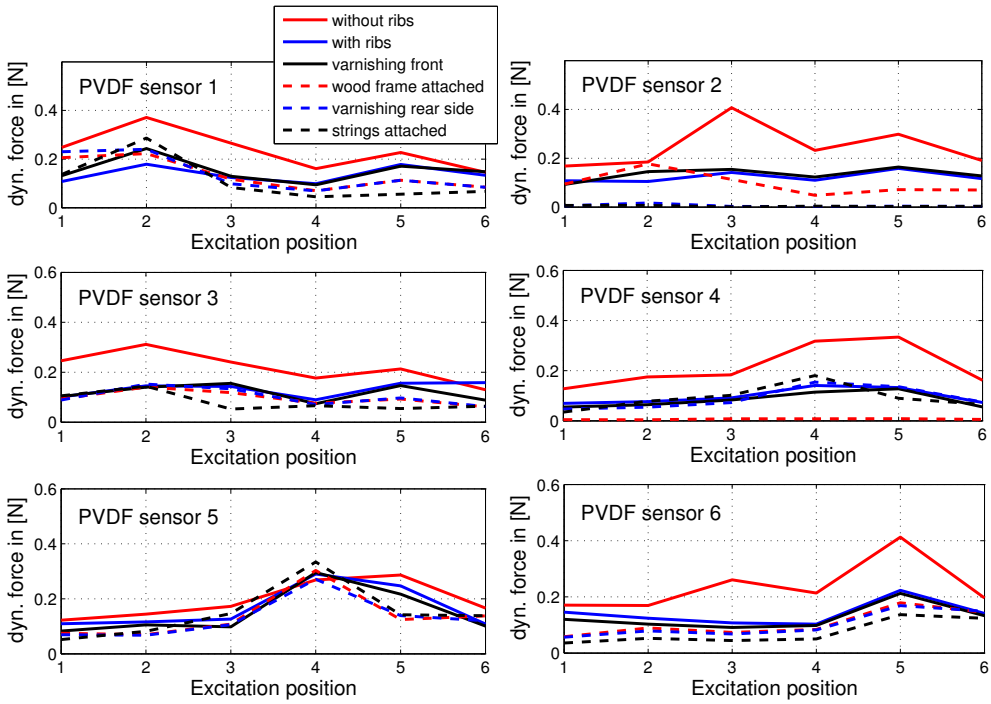

Figure 5.7: Pulse amplitudes for all PVDF sensors and all construction steps at the different excitations points. See Fig. 5.3a as the reference.

For the same excitation the signals of the sensors 'PVDF2' and 'PVDF3' are presented, which reveal a different relative location of their maximum amplitudes. While the 'PVDF3' signal has its maximum at the beginning of the excitation, the 'PVDF2' signal has its peak about 8ms later.

The maximum amplitude of a single excitation was checked after each construction step. Due to the normalized excitation, the measured signals are also normalized throughout the investigation. Fig. 5.7 shows all the amplitude measurements in an overview. One of the main findings, which also fully confirms intuition, is the correlation between the amplitudes and the excitation point at the bridge. For example, the initial dynamic force value for sensor 'PVDF4' is larger for the excitation points 4 & 5 compared to the points 1 & 2 (see Fig. 5.7), which is obviously due to the distance between the excitation point and the sensor position. While most recorded amplitudes obey this correlation, there are also outcomes which are not so easy to explain and are against the expectations. For example, the differences of the 'PVDF2' and 'PVDF3' amplitudes, which were measured during the excitations at position 'EX 2' (see again Fig. 5.6): From the perspective of the excitation positions, a stronger maximum amplitude would be expected for the sensor 'PVDF2' (compared to sensor 'PVDF3'), but exactly the opposite

has been found. In that case depicted in Fig. 5.6 the 'PVDF3' maximum amplitude is 1.5 times stronger then the 'PVDF2' signal. One explanation for this effect could be the positive interference of scattered waves within the soundboard, but more likely is another explanation: A large value recorded by the PVDF sensors means a large acceleration between the soundboard and the bridge, not neccessarily a large net force. Therefore, two signals with the same energy content are able to generate amplitudes, which can be quite different. The present case with an excitation at position 'EX 2' shows the maximum amplitude at the position of 'PVDF3'. A good picture for an explanation of this effect is a stroke of the whip, where the outer end of the whip is much more accelerated compared to the starting point. But nevertheless, it is noticeable that the overall signal envelope (see Fig. 5.6) for both signals (except for some single peak values) have the same appearence.

Furthermore, except for sensor 'PVDF5', it was found that there is a large difference regarding the amplitudes between steps 1a and 1b (reference Tab. 5.1). The mounting of additional ribs onto the soundboard results in a significant damping of the amplitude. For example, the largest difference was found for the sensor 'PVDF2' at excitation position 'EX 3', where a factor of 2.7 (0.40 N (rib-free) to 0.15 N (ribbed)) was determined (see Fig. 5.7). The average of the force amplitude for all sensors changed from 0.23 N (without ribs) to 0.14 N (with ribs). This amplitude drop at the measurement points can be explained by scattering of the acoustic sound wave at the ribs, which yield a more equally distributed energy of the excitation within the soundboard. Also, the increase of the soundboard rigidity due to the ribs will decrease the movability of the resonance board perpendicular to its surface.

5.3.2 Normalized Spectra

The spectra in the following have been determined via averaging over at least 12 individual excitations, which results in a significant reduction of the signal-to-noise ratio. Due to the large quantity of determined spectra, a representative selection is depicted in Fig. 5.8: (**a**) shows the spectral evolution of the soundboard during the six investigated piano assembly steps (bottom (step 1a) to top (step 5) (see Tab. 5.1)). For this, the resonance board was excited at position 'EX 1' and only the 'PVDF1' sensor signals are shown. (**b**) on the other hand shows the spectral signal for all sensors (from bottom to top: 'PVDF1', 'PVDF2', 'PVDF3', 'PVDF4', 'PVDF5', 'PVDF6', and microphone) measured during one single excitation at the position 'EX 1'.

Essentially, no qualitative evolution, in particular no emerging pass bands between an empty and a ribbed soundboard as known from the multichord measurements, can be observed. There are several reasons for this outcome:

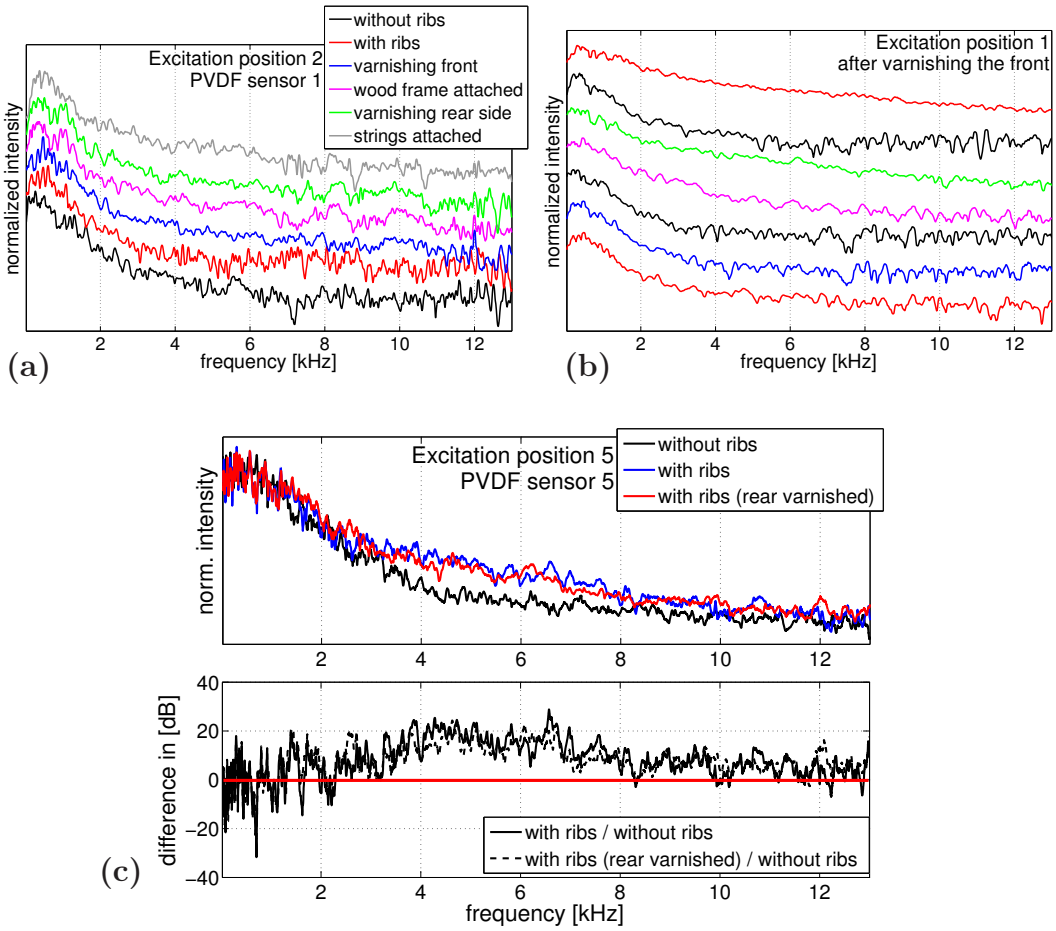

Figure 5.8: **(a)**: PVDF sensor 1: The spectral evolution over the six construction steps (recorded at the same excitation point 'EX 2'). Curves are separated by a factor of 10 for a better comparability. **(b)**: Output for all measurement devices for one excitation event (from top to bottom: 'PVDF1' via 'PVDF6' to Microphone). Curves separated by 100. **(c)**: Rib influence on the spectrum (*top*) with the spectral differences (*bottom*).

The distances between the mounted ribs are successively increasing (from 83 mm to 112.5 mm (see Fig. 5.3a) starting from the high tone pitch side of the soundboard. Also the lengths of the ribs are not equal (ranging from 284.0 mm (rib no. 1) to 1012.0 mm (rib no. 6)), as well as their heights (from 18mm (no.1) to 27mm (no.6)) and their widths (25mm for all ribs, except 26mm for no. 7 and 27mm for no. 6). Furthermore, the geometry of the soundboard is far from being rectangular. All these listed variations of the assembly parts are perturbations towards the LCM model we know from the background chapter (see Sec. 2.1.4). This leads to the elimination of the pass-band structure, which was found for the conceptional soundboard (see Sec. 4.3). But these variations of the assembly parts could be the initial point

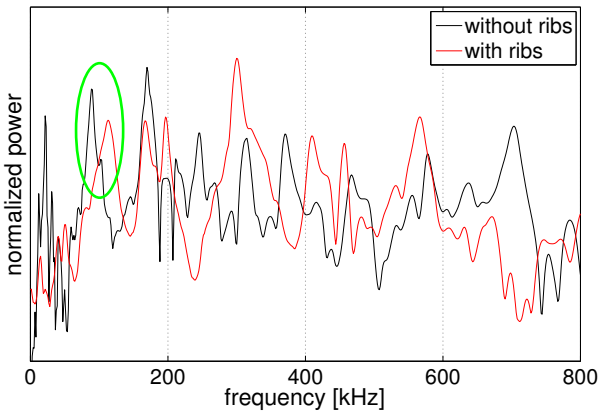

Figure 5.9: Increase of the fundamental frequency of the soundboard from 89Hz ('non-ribbed') to 113Hz ('ribbed') highlighted with the green ellipse. Also, the lowering of the spectral intensity of the fundamental frequency can be observed.

for further investigations and their relation to the LCM model. Nevertheless, one can make a statement about the difference between a free and a ribbed soundboard, which is depicted in Fig. 5.8c. A clear elevation of the normalized spectral signal between 2.5 kHz and 10 kHz with a maximum of 29dB and an average of 13.9 dB can be observed for the 'ribbed' case. This is independent from the varnishing of the rear side of the board, which is shown as the red curve. The increase of this frequency range means a higher brilliance for the soundboard, although nothing can be said about the decay behavior yet. The damping factor (depending on the frequency) needs therefore to be calculated, which will be done in the next section.

Another effect, which is observed (see Fig. 5.9), is the shift of the fundamental frequency of the soundboard towards higher frequencies, due to the enhanced rigidity of the board. The determined shift is from 89Hz ('non-ribbed') to 113Hz ('ribbed'). At the same time, an intensity lowering of the fundamental frequency can be seen. Both effects are also described in [Giordano 1997, Wogram 1980] and in Sec. 2.1.3.

5.3.3 Damping Factor

The damping factor or rather the decay factor γ is calculated in the same way as described in Sec. 4.3.2, with a logarithmic fit of the tone decay. Doing this for small frequency slices with a width of $\Delta f = 1.8$Hz (which is the actual resolution of the FFT performed) yields the decay factor at different frequencies. A lot of analyzes have been made regarding the damping factor and the influence of the rib presence (see Fig. 5.10): i) γ vs. the location on the board (a), ii) γ through the construction steps for the PVDF sensor 'PVDF4' (b), iii) different γ's of the microphone and the PVDF sensors (c), and iv) γ of the multichord and the piano (d). The differences of γ (if there are ribs or not) are further analyzed in Fig. 5.11 for the multichord and the

Bechstein soundboard.

Starting with Fig. 5.10a, it can be observed that γ is not significantly different at the rim of the soundboard both with ribs or without (see 'PVDF1' and 'PVDF6'). But in contrast to that, the middle of the soundboard (at 'PVDF4'), shows a significant γ variation where the minimum changes its position from 2 kHz to 6.7 kHz (with a maximum variation from -50 [1/s] (rib-free) to -100 [1/s] (ribbed) at about 6.7 kHz). Thus, the γ variance of the soundboard center is higher compared to the rim of the resonance board. The curves for one individual sensor are additionally separated by a factor of 100 for a better comparison.

Fig. 5.10b shows the measurements of only one single PVDF sensor ('PVDF4'), through all the construction steps of the piano. The zoom of the lower part of the frequency spectra reveals a range between 1 kHz and 3 kHz with a large variation of the damping factor. This frequency range, approximately beginning with the piano tone C6 (1046.50 Hz), is not only important for the higher notes, but also for the sound or rather the brilliance of the lower notes. This variability of γ for the solid-state vibrations in this range has not yet been reported to our knowledge. The largest γ difference which is at about 2 kHz corresponds to a factor of 5 between step no. 4 and 5 (see Tab. 5.1). Hence, the maximum change of γ was observed when the metal frame with the strings is attached to the wooden frame of the piano.

A further analysis comprises the different acquisition techniques (condenser microphone and body vibration sensor) and their influence on the damping factor, shown in Fig. 5.10c. Simultaneous measurements reveal large deviations of the γ distribution dependent on the recording technique. While γ of the PVDF sensors shows a maximal damping around 2 kHz, the γ curve for the condenser microphone follows a smooth decreasing trend. One of the reasons for the difference of γ between both acquisition techniques could be the influence of the recording room on the microphone spectrum, due to less damping for all frequencies.

One of the most interesting parts of the analysis concerns the direct comparison of γ for the two investigated instruments (Multichord vs. Bechstein piano), which is depicted in Fig. 5.10d and Fig. 5.11. The absolute damping factor (without ribs and with ribs) is shown in the first plot, while the latter depicts the direct difference ('ribs' - 'without ribs') for each instrument. The Bechstein curves in 5.10d are enhanced by an additional factor of 100 for a better comparability. Within the frequency range from 2 kHz to 8 kHz the multichord damping factor γ_M reveals a slower vibrational decay with the ribs mounted onto the soundboard. This results in a longer sounding of the intrument. The decay factor of the Bechstein soundboard γ_B has a different overall trend than γ_M, if the ribs are mounted: While in the frequency range

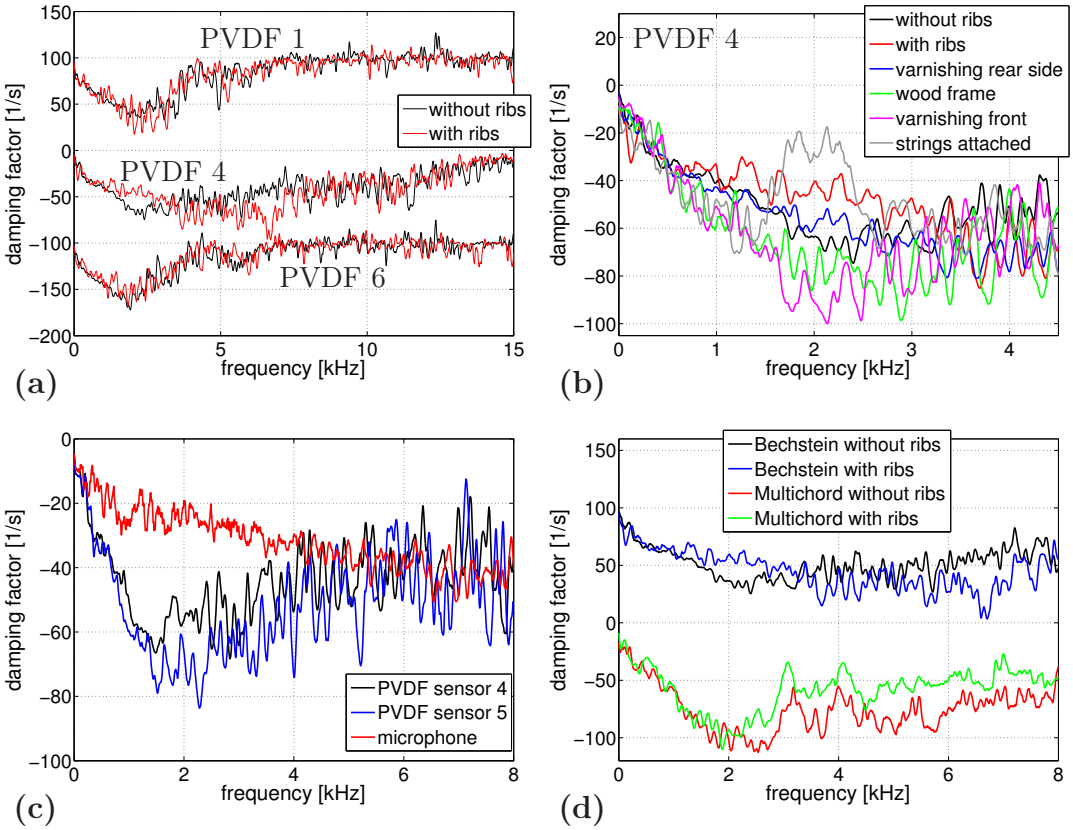

Figure 5.10: **(a)**: Damping factor γ for 3 different PVDF sensors (both with and without ribs): Not many changes of γ at the rim of the soundboard, in contrast to the middle of the board. Curves are separated by an additional factor of 100 for a better comparability. **(b)**: The damping factor for 'PVDF4' excited at position 'EX 4' followed through the assembly steps of the piano. A large parameter variation occurs in the frequency range from about 1 kHz to 3 kHz. **(c)**: The difference of the damping factor between microphone and two PVDF sensor signals. This difference is due to the different sensor technology and radiation pattern. (Measurements after step 4 are plotted, when the rear of soundboard is varnished (see Tab. 5.1)). **(d)**: Bechstein vs. Multichord: Direct comparision of γ dependent on the rib presence. Curves separated by additional factor of 100.

from 1 kHz to 3 kHz a similar behavior to the multichord can be observed with a slower vibrational decay, the range between 3 kHz and 8 kHz shows in contrast to that a faster decay. Despite having a higher overall brilliance between 2.5 kHz and 10 kHz (see Fig. 5.8c), the faster vibrational decay means a very effective radiation of the Bechstein resonance board compared to the conceptional soundboard.

The results of the investigation from [Chaigne 2011] about the rib effects

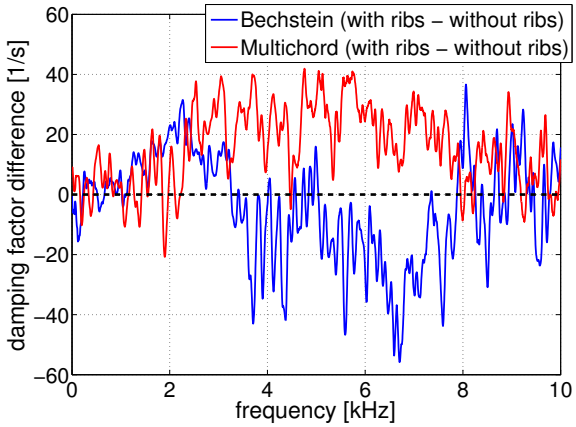

Figure 5.11: The direct comparison (subtraction 'with ribs' – 'without ribs') of the decay factor γ dependent on the frequency. The differences of the individual instruments between 3 kHz and 8 kHz are significant.

on soundboards are not published yet[3].

5.4 Chapter Conclusion

Summarizing this chapter, each step of the assembly of an upright piano manufactured by 'C. Bechstein Pianofortefabrik' was monitored completely with six PVDF sensors and a conventional condenser microphone. With the polymer sensors mounted between bridge and soundboard, all construction steps of an upright piano were documented; all changes in the soundboard characteristics were recorded. Just for this measurement campaign, the typical assembly process was modified in order to investigate the differences between a 'free' and a 'ribbed' soundboard. Hence, a direct comparison between the piano and the multichord is possible. Despite having a completely different geometry, similarities in the spectrum have been found, but the spectral differences are predominant. While from 1 kHz to 3 kHz, a similar behavior can be observed for the multichord and the Bechstein soundboard (slower vibrational decay), the frequency range between 3 kHz and 8 kHz shows a contrary behavior (faster decay). Also a large difference can be observed in the intensity of the frequency spectrum, when the 'ribbed' Bechstein soundboard exibits a significant enhancement from 2.5 kHz to 10 kHz, and the 'ribbed' multichord shows in contrast a significant reduction due to the ideal LCM configuration.

In the end, the rib array design on the soundboard is a compromise: On the one hand, the soundboard stability to counter the high tension from the strings, which leads to a specific brilliance enhancement (see Fig. 5.8c), and on the other hand, a faster vibrational decay which follows (see Fig. 5.11).

[3]Information from E-Mail correspondence with Antoine Chaigne.

Due to the large number of the perturbations regarding the LCM model (see 2.1.4; namely the varying rib distance, the gradual thinning of the rib endings, etc.) the sound of the resonance board becomes more homogeneous. Having these boundary conditions, no pass-band structures, which were shown in the multichord investigation, are able to emerge. Hence, the radiation of the soundboard is optimized in a way which is most suitable for our listening needs.

Chapter 6

Conclusion and Outlook

The present thesis treats the question of the generation, radiation, and the propagation of sound waves regarding instrument soundboards. It consists of two parts: the development of experimental techniques in order to measure internally propagated and radiated sound (see Chapter 3) and a comparison of measured sound between a conceptual soundboard and a *genuine* Bechstein resonance board with simple theoretical approaches (see Chapter 4 & 5).

The first part fully describes the preparation, calibration, and characterization of specially prepared structure-born vibration sensors, which are made out of piezoelectric polyvinylidene fluoride (PVDF) [Kappel 2011]. It is demonstrated that these special probes can be used as integrated dynamic force sensors. The specific application of these probes for the measurement of solid-state vibrations was one of the main challenges in this investigation. The piezopolymer sensors have many practical advantages, like their variable geometry, their flexible handling, the relatively low cost of the material, and that they exclusively measure solid-state vibrations without perturbations from airborne sound, to name just a few. The main advantage from the perspective of scientific recording, is the extremely small probe thickness, which allows minimally invasive measurements *inside* of a vibrating system with minimum perturbation. The relatively high signal-to-noise ratio and the fast recording speed, which implies an insignificant signal delay, are comparable to microphones.

Concerning the calibration, the relaxation of the polymer sensor under an external force was of major interest. Much effort was put into the understanding and the characterization of the probe efficiency both on short and long term scales. It has been shown in this work that a careful calibration can compensate the impact of the parameter drift resulting from external stress. The determination of the vertical electromechanical conversion, which is represented by the piezoelectric coefficient d_{33}, was *the* important procedure throughout the technical part of this investigation. Its behavior was monitored with respect to several important parameters, such as the static force, the amplitude of the dynamic force, the frequency response, and the long-term stability. Knowing these values and their evolution will yield a

reliable and calibrated measurement of the structure-born vibrations.

The second part of the study not only brought forward the application of these specially prepared PVDF sensors, which are mounted within musical instruments. Also, the investigation of scattering effects within instrument soundboards in the presence of a regular array are examined. The array consists of uniform ribs attached to a soundboard. It was demonstrated, which dramatic impact on the soundboard radiation and sound-wave propagation this could have. Moreover, the acquired results and their effects can be applied acoustically to any regularly structured surface. Only few investigations of the 'ribbing' effect of soundboards have been made [Wogram 1980, Chaigne 2011], and the obtained results are either limited in frequency range and resolution, or the results were not published yet.

The acoustic scattering effects mentioned above were investigated with two different setups : i) a multichord, which represents a conceptual soundboard ([Kappel 2010]), and ii) a genuine upright piano manufactured by 'C. Bechstein Pianofortefabrik'. The rectangular multichord (i) was specially designed with minimal parameter variation, except for the rib mounting. Hence, a fully controllable setup was achieved, ensuring the reproducibility of the measured results. Governed by the question: 'What is the effect of sound wave propagation when ribs are mounted onto a soundboard?', the number of the ribs as well as their distance were varied in the course of the investigation. It was found, that even just a few ribs strongly modify the sound radiation and propagation. A banded structure of passing frequencies (and their harmonics) emerges, which can be only explained by the presence of the ribs. These 'pass bands' correspond to the eigenmodes of the structured soundboard. They are in perfect agreement with qualitative band theory ('linear-chain model'), analogous to the eigenmodes of phonons in solid-state physics. It was also observed that the effect becomes more prominent with increasing rib number.

In addition, the assembly of an upright piano (ii) was scientifically complemented by mounted PVDF sensors. They were inserted between the bridge and the soundboard at the beginning of the piano build-up. Each single construction step was documented, and the soundwave propagation characteristics of the soundboard were recorded. The traditional piano construction process was modified in order to study the differences between a 'free' and a 'ribbed' soundboard. Based on these results, it was possible to make a qualitative comparison between the piano and the conceptual soundboard. Naturally, the multichord geometry is completely different from a real piano, and thus the modal structure is much more complex for the piano soundboard. But some similarities in the spectrum should be expected, following general arguments. Besides the fact that the additionally mounted

ribs in each case changed the frequency spectrum, it was found that the damping factor γ of most Bechstein and all multichord measurements follow the same overall behavior in the frequency range from 1 to 3 kHz with having a minimum (i.e. the largest damping) around 2 kHz. (An exception represents the central area of the Bechstein soundboard. There, a different behavior concerning the damping factor γ was found, where the decay factor changed its minimum from 2 kHz (without ribs) to 6.5 kHz (with ribs)). The spectral range from 3 to 8 kHz shows a large difference of γ between Bechstein soundboard and multichord. While the multichord has a slower vibrational decay, the Bechstein soundboard exibits an increasing damping factor γ. It is clear that the different geometries and rib configurations are causing these differences of the damping behavior. Obviously, due to the special design of the Bechstein piano and its deviations from the LCM model, the pass-band structure is smeared out and the radiation of the soundboard is therefore homogenized to optimize it in a way that is more suitable to our listening needs. Eventually, the specific rib design of the genuine piano can be regarded as a compromise: The stability of the soundboard, which is needed to withstand the high pressure generated from the strings and the spectral intensity enhancement from 3 to 10 kHz on the one hand, and on the other hand a faster vibrational decay between 3 and 8 kHz, resulting from a more efficient radiation of the soundboard. The present rib design and its arrangement is the result of an evolution of the best possible listening characteristics over the last three centuries.

By combining the monitoring of body vibrations with the customized piezoelectric PVDF sensors and the measurement of radiated airborne sound by conventional methods (e.g. condenser microphones), one is able to deduce the temporal distribution of the vibrational energy in the investigated structure. This acoustic recording procedure can therefore be recommended as an optimal measurement method: PVDF sensors record the solid-state vibrations *inside*, and one or more condenser microphones placed *outside* of the structure acquire the airborne sound waves, simultaneously.

But many aspects concerning this topic were not yet investigated and remain open. A systematic study of the radiated and propagated sound in dependence on the measuring angle as well as further piezopolymer locations for the structure-born vibrations, could be helpful in verifying the obtained results. Also, the influence of different materials, geometries, and sizes for the conceptual soundboard is another starting point for follow-up measurements. But the major achievement in the future would be the exploration of the grand piano characteristics. In particular, a long-term radiation monitoring of the soundboard would be an interesting issue. For piano makers, the radiation

dependency on crucial parameters could be investigated, such as the humidity content, the form of the rib endings, the gradual thinning towards the treble side of the sound bridge, etc. The number of relevant variables important for the radiation and sound wave propagation characteristics seems endless in such a complex instrument as the piano.

However, it is also worth to discover further applications for the calibrated and characterized PVDF sensors. A huge selection of possible implementations are imaginable, such as wall-integrated monitoring of buildings, innovative nondestructive sensors for alarm systems, and further machinery.

In the end, a rich and fruitful topic was highlighted concerning the minimally invasive sensor technology. An exceptionally robust and reliable measurement technique for the recording of internal vibrations has evolved and was tested in different setups. Also, new insights were achieved in the sound-wave propagation characteristics of structured surfaces. In doing so, a transfer of solid-state theory models to the physics of musical instruments was successfully realized. Finally, similarities and differences in the sound-wave propagation and radiation between a conceptual and a genuine piano soundboard were found.

Appendix A

Appendix

A.1 Technical Background

A.1.1 Microphones

The use of microphones, in particular capacitor microphones (see Fig. A.1a and b), as recording devices is a standard technique, commonly used for acoustical measurements and well described in the literature [Eargle 2004, Ballou 2009, Wong 1997].

A.1.1.1 Physical Background of Capacitor Microphones

A condenser microphone consists of one diaphragm and a backplate with a small cavity of air (for design see Fig. A.1c). A voltage V, supplied either by a battery in the microphone or by external power, is applied between the planes. As a further development of this concept, the electret capacitor microphone has a special material for the diaphragm or the backplate, which is permanently charged. Nevertheless, a preamplifier is needed in the mode of operation.

The plate at the outside of the microphone, which is used as a 'diaphragm', is made of very light and thin material (a few microns thick). Compared to dynamic microphones, the characteristics of the plate material is the reason why capacitor microphones have such an outstanding frequency response, which is shown specifically for the Brüel & Kjær 1/2“ free-field microphone 'type 4191' in the next subsection (see Fig. A.2). Deformations of the outer membrane generated by a sound wave temporarily change the width of the air cavity, resulting in a capacitance change of the charged plates. A minor distance increases the capacitance and hence a current flows, which can be measured. With an increasing distance, the capacitance is reduced and a current can be measured, too, but in the opposite direction. Therefore, a sound signal normally produces an alternating current. Capacitor microphones are able to measure at very high audio frequencies, and they are usually much more sensitive than their dynamic counterparts. Therefore, they require less amplification to produce the same level of output in comparison to the dynamic microphones. Not only does that make them more suitable for

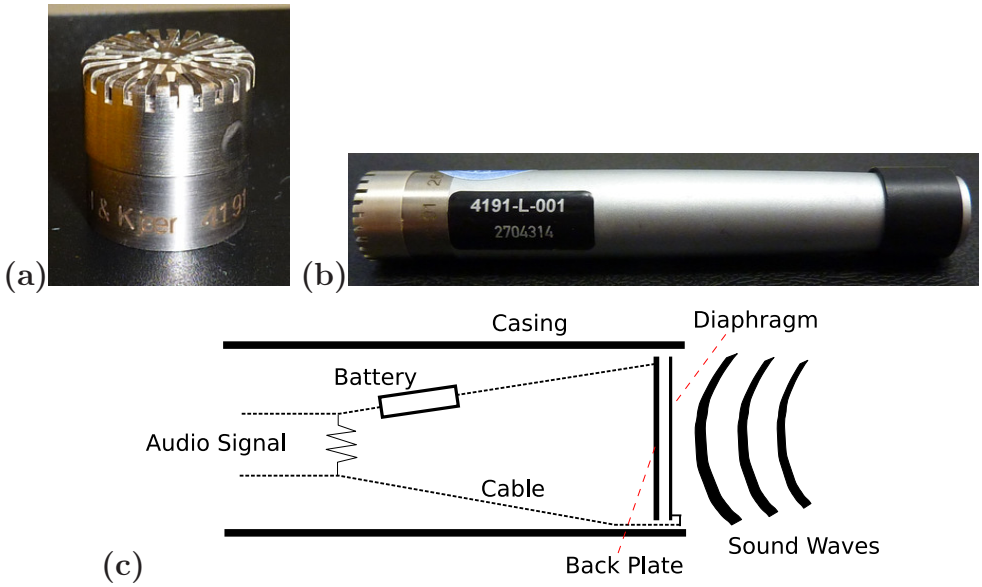

Figure A.1: **(a)**: Brüel & Kjær 1/2“ free-field microphone type 4191 used for the measurements of the airborne sound throughout this investigation.
(b): Shown is the same microphone as in **(a)**, but with additional pre-amplifier, which is needed for the measurements.
(c): Sketch of the condenser microphone assembly.

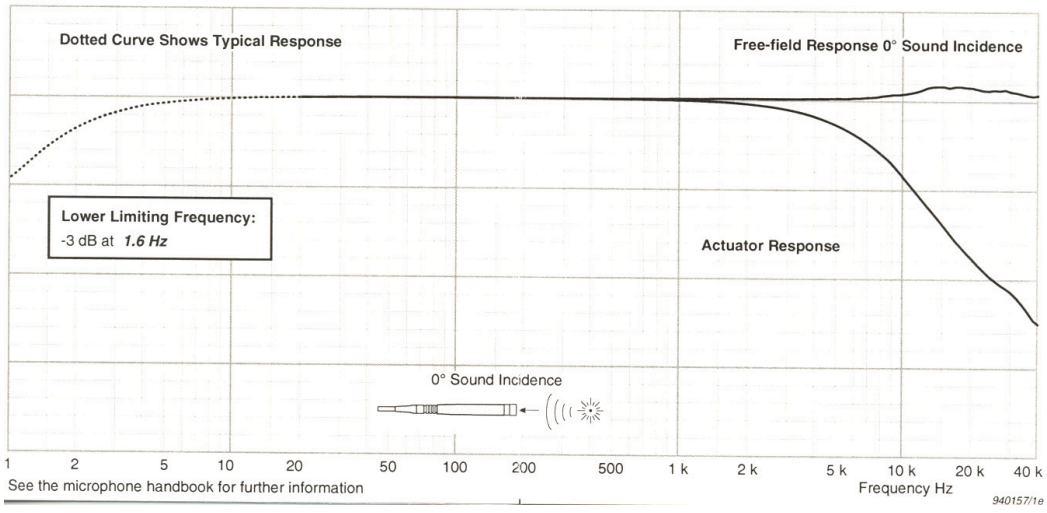

Figure A.2: The Brüel & Kjær 1/2“ free-field microphone ’type 4191’ frequency response (black solid line) as given from the manufacturer.

very weak signal sources, but there is also the advantage of the linear frequency response, which is an outstanding feature, de facto simplifying the process of data acquisition. The frequency response of the capacitor microphone is much

flatter than of the dynamic ones and therefore much easier to handle in the data analysis.

A.1.1.2 Brüel & Kjær Condenser Microphone

Throughout this investigation the 1/2“ freefield Brüel & Kjær condenser microphone 'type 4191' with the preamplifier 'type 2669L' was used. The signal from the microphone is then further amplified by the fitting Brüel & Kjær amplifier 'Nexus type 2690'. The frequency response function for the whole setup, given by the manufacturer, is presented in Fig. A.2, showing a perfect flat behavior in the important frequency range 20Hz to 20kHz.

A.1.2 Acoustic Laboratory and Ambient Noise

Within the recording room, the absorption occurs at the same time as the damping/reflection of ambient noise by the outer room walls. Considering the reflection, the sound wave from outside is hindered to radiate into the recording room. The damping coefficient R of a free standing wall can be determined theoretically by [Möser 2010]:

$$R \approx 10 \cdot \lg\left(\frac{\omega m''}{2 \cdot Z_0}\right)^2, \tag{A.1}$$

whereas ω, m'' and Z_0 represent the frequency, the mass of the wall in relation to its surface area and the characteristic acoustic impedance of the gas behind the wall (which in this case is air with an impedance value of $Z_{\text{air}} = 413,5$ Ns/m^3 at a temperature of 20°C and a pressure of 1 atm), respectively. The characteristic acoustic impedance Z_0 is a material property and given by the material density ϱ and the sound velocity c:

$$Z_0 = \varrho \cdot c \tag{A.2}$$

The theoretical progression of R is displayed in Fig. A.3 for three different temperatures (0°C, 20°C and 35°C). It is nicely shown that there is hardly a difference in the damping coefficient R for different temperatures.

Therefore, a temperature dependence of the measurement can be safely neglected. To measure the damping coefficient one needs two reverberation rooms – a sending room and a measurement room [Möser 2007, Veit 1996]. Unfortunately, both rooms are difficult to realize for different reasons. On the one hand, the absorption material is already placed in the recording room, while on the other hand the actual acoustic laboratory is no reverberation room at all, due to the whole measurement equipment, which acts as an absorber. Therefore, the measurement of this characteristic is not possible without destroying important parts of the recording room.

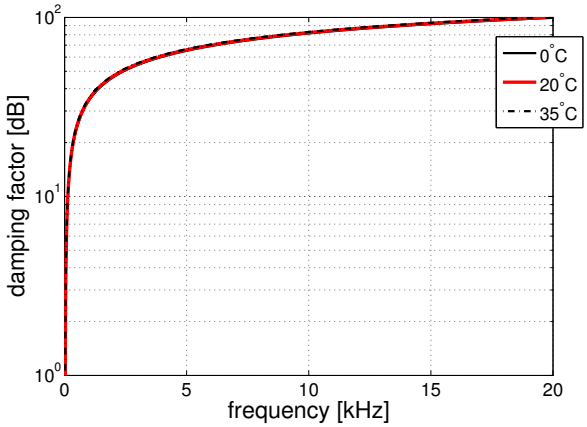

Figure A.3: Theoretical characteristic acoustic impedance of the gypsum plaster board walls of the recording room. The sensitivity to temperature is displayed with three different curve progressions. Temperatures plotted are 0°C, 20°C and 35°C. As can be seen from the curves, the differences for the three temperatures are minimal.

A.2 Additional Theoretical Background

A.2.1 Levenberg-Marquardt Method

The Levenberg-Marquardt algorithm (LMA) [Marquardt 1963] provides a numerical solution to the mathematical problem of minimizing a function, which is generally nonlinear, over a space of parameters of the function. This minimization problem arises especially in *least-squares* curve fitting. The LMA is a modification of the Gauss-Newton algorithm (GNA), but the LMA is more robust than the GNA, which means that in many cases it generates a solution even if the initial values are very far off the final values. But nevertheless the convergence to a solution is not guaranteed with the LMA, due to possibly bad initial values. It could also happen, with these bad initial guesses, that the LMA just finds a local minimum and not the global one. That makes the definition of the initial guesses an important point within the procedure.
For the function $F(x) : \mathrm{R}^m \rightarrow \mathrm{R}^n$ $m < n$ the minimization problem

$$\min_{x \in \mathrm{R}^m} \|F(x)\|_2^2 \tag{A.3}$$

is to be solved with the initial value x_0. If it is done in the GNA, $F(x)$ is approximated in every step through a linearization and the alternate problem

$$\min_{x \in \mathrm{R}^m} \|F(x_k) + J(x_k)(x - x_k)\|_2^2 \tag{A.4}$$

is observed. In that equation J represents the Jacobian of the function F. Additionally, it is required for the LMA that

$$\|x - x_k\|_2^2 < r_k \tag{A.5}$$

Due to this additional constraint it is possible to force the decay of $\|F(x_k)\|_2^2$ in every step. For that the parameter r_k is always adjusted.
The Levenberg-Marquardt procedure descends locally to the Newton procedure, so the convergence is locally quadratic.

A.2.2 Correlation Function

In the data signal processing, the correlation function $\xi(\tau)$ [Smith 1997, Rodgers 1988, Hartmann 1998] between two parameters x and y is an important mathematical method to check possible dependencies. Usual cases of 'hidden' dependencies, for example as a function of time, space or temperature, will be eleminated through this function. The correlation function $\xi(\tau)$ of two parameters $x(t)$ and $y(t)$ can be written as:

$$\xi(\tau) = \int_{-\infty}^{\infty} x(t)y(t+\tau)\mathrm{d}t.$$

with $\xi \in [-1, 1]$; $\xi = -1$ means perfect anti-correlation, 0 no correlation at all and 1 perfect correlation. Therefore, it is needed here to normalize both parameters in such a way, that the correlation function $\xi(\tau)$ remain in the given range $[-1, 1]$. The most practical normalization is the $\mathcal{L}^2$ normalization, which is defined by

$$\|f\|_2 := \left(\int_\Omega \|f(t)\|^2 \,\mathrm{d}t\right)^{1/2} \stackrel{!}{=} 1$$

Ω here represents the domain of the function. Applying the $\mathcal{L}^2$ normalization, $\xi(\tau)$ will always be between -1 and 1. The correlation function characterizes (similar to the transfer function) the change of shape of a wave over a time interval τ, or distance Δx, respectively.

A.2.3 Fourier Transform

The Fourier transform [Smith 1997, Rabiner 1975, Guillaume 2006, Hartmann 1998] is a reversible transform of a time-dependent signal $x(t)$ into a frequency-dependent signal $\hat{x}(\nu)$. Thereby, the signal $\hat{x}(\nu)$ can be described bijectively as a superposition of the fundamental frequency and its harmonics for a periodic function:

$$f(t) = f(t + T_0) \qquad \forall t \in \mathbb{R}$$

and

$$T_0 = \frac{2\pi}{\omega_0}.$$

where T_0 represents the function period. The Fourier analysis is practical in particular for these periodic functions.

Furthermore, $x(t)$ needs to be continuous in the complex range and the Fourier series expansion, which decomposes the periodic signals into a sum of simple oscillating functions, can be written as:

$$f(t) = \sum_{n \in \mathbb{Z}} c_n(f) e^{-in\omega_0 t} \qquad \forall t \in \mathbb{R}$$

with the respective Fourier coefficients $c_n(f)$:

$$c_n(f) = \frac{\omega_0}{2\pi} \int_{-\pi/\omega_0}^{\pi/\omega_0} f(t) e^{in\omega_0 t} \mathrm{d}t \qquad \forall n \in \mathbb{Z}$$

Here, c_n needs to be unique. If a complex continuous function $f(t) \in \mathbb{R}$ is furthermore absolutely integrable (i.e. $\lim_{T\to\infty} \int_{-T}^{T} |f(t)| \mathrm{d}t < \infty$), the Fourier transform $\mathfrak{F}$, which expresses the time-dependent signal $x(t)$ as a function of frequency, will look like:

$$\mathfrak{F}(f(t)) = \frac{1}{\sqrt{2\pi}} \int_{-\infty}^{\infty} f(t) e^{+i\omega t} \mathrm{d}t \qquad \forall \omega \in \mathbb{R}$$

while the back transform appears as

$$f(t) = \frac{1}{\sqrt{2\pi}} \int_{-\infty}^{\infty} \tilde{f}(\omega) e^{-i\omega t} \mathrm{d}\omega \qquad \forall t \in \mathbb{R}$$

According to the Nyquist theorem [Smith 1997, Guillaume 2006], an increase of the signal sampling rate (samples/time) will expand the frequency spectrum towards higher frequencies. With a known sampling frequency SR, an upper frequency bound f_{max} is given by: $f_{max} < SR/2$. Below this specific frequency f_{max}, the whole signal can be perfectly reconstructed.

A.2.3.1 Fast Fourier Transform

The Fast Fourier transform (FFT) is the 'working horse' in the spectral analysis and an efficient algorithm to determine the discrete Fourier transform. The Cooley-Tukey algorithm [Cooley 1965] is the most commonly used algorithm. Recursively, it breaks down the discrete Fourier transform into smaller parts, which are faster to compute. Owing to the available computing power today, the fast Fourier transform can be done in an appropriate time span.

A.2.4 Tone Generation by a String

Since this investigation deals with the physics of pianos, the generation of a tone by string vibration [Guillaume 2006] should be shortly mentioned. An ideal piano tone $f(t)$ consist of many single sinusoidal tones, which are superimposed on each other:

$$f_n(t) = A_n \sin \omega_n t + \varphi_n, \qquad A_n \geq 0, \varphi_n \in \mathbb{R}$$

with $T = \frac{2\pi}{\omega_0}$ as the period of the first harmonic. The lowest angular frequency ω_0 is also the smallest divisor of all frequencies concerning this tone description. This ω_0, which is the fundamental frequency of the tone, is decisive for the tone pitch. The intensity distribution of the harmonics is responsible for the tone timbre.

A.2.4.1 The 1-dim vibrating String

Generally, a string can be vibrated perpendicular (transversal) and in direction (longitudinal) of the string. The longitudinal vibration, which corresponds to density vibrations within the string [Möser 2010], is typically not considered in the sound analysis due to its relatively low intensity. Only accounting for the transversal modes, it can be observed that the strings are fixed at their ends, having a velocity that equals zero – $v_E = 0$. With these assumptions, one can solve the one-dimensional homogeneous wave equation [Guillaume 2006]:

$$\frac{\partial^2 u}{\partial x^2} - \frac{1}{c^2}\frac{\partial^2 u}{\partial t^2} = 0,$$

with the following *d'Alembert* solution:

$$u(x,t) = \varphi(x + ct) + \psi(x - ct)$$

and the two arbitrary functions φ and ψ, which must be differentiable. With the known boundary condition $v_E = 0$, one obtains the following representation:

$$u(x,t) = a\sin\left(2\pi n \cdot \frac{x}{L}\right) \cdot e^{i\omega t}.$$

This solution describes standing waves with a wave length of $\lambda = \frac{L}{2n}$; these are also the only possible modes of an ideal vibrating string. Assuming the complete chain, which is needed to play a stringed instrument, this is of course a very basic model. Non-linear effects, such as damping and transfer functions through the instrument, are not easy to implement into the model, but they all contribute to the individual timbre.

A.2.5 Propagation of Sound Waves in Gases

Airborne sound waves are longitudinal waves and they can be described via the sound wave elongation $\mathrm{d}(x,t)$. This is the position vector of the particle at the time t and at the position x. Under stationary condition one can state in first order, that [Möser 2007]:

$$\mathrm{rot}(\mathrm{d}(x,t)) = 0$$

That would mean, the rotation of the sound waves over the edge of an area is always zero. 'Translated' it would be: What goes in, comes out. Furthermore, one can write the vector wave equation (also in the first order) as [Guillaume 2006, Möser 2007]:

$$\left(\frac{1}{\hat{c}} \cdot \frac{\partial}{\partial t}\right)^2 \mathrm{d}(x,t) - \Delta \mathrm{d}(x,t) = 0$$

with $\hat{c}$ as the sound wave velocity, fulfilling $\hat{c} = 1/\sqrt{\langle\kappa\rangle \langle\mu\rangle}$. The average compressibility is $\langle\kappa\rangle$ and $\langle\mu\rangle$ represents the average density of the gas. These parameters are also dependent on the temperature T and the pressure p. If the solution of the wave equation furthermore has the condition $\mathrm{rot}(\mathrm{d}(x,t)) = 0$, the solutions will be longitudinal waves.

In the following some other important parameters for the propagation of sound waves, which can also be found in [Guillaume 2006, Möser 2007], are presented. First of all, there is the sound particle velocity, which is described by the sound-wave displacement:

$$u(x,t) = \frac{\partial}{\partial t}\mathrm{d}(x,t)$$

Secondly, the sound pressure $p = P - \langle P\rangle$ can also be defined via the sound-wave displacement:

$$p(x,t) = -\frac{1}{\langle\kappa\rangle}\mathrm{div}(\mathrm{d}(x,t))$$

The sound wave velocity is dependent on the temperature:

$$\hat{c}(T) \approx \sqrt{\frac{T}{T_0}}\hat{c}(T_0)$$

where $T_0 = 273,15$ K. Therefore, the velocity of the sound wave increases for higher temperatures. That is due to the larger mobility of the sound particles and arises from thermodynamics.

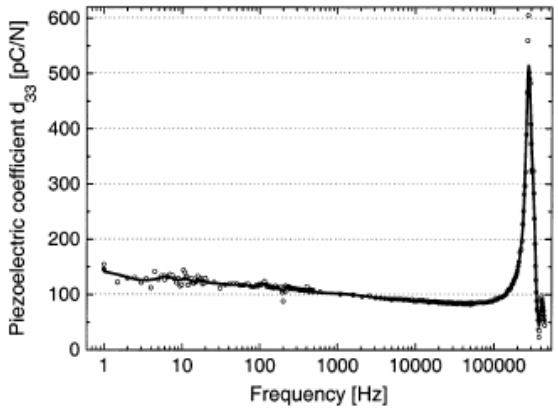

Figure A.4: (Graph taken from [Hillenbrand 2004].) The resonance spectrum of cellular polypropylene with a thickness of 70μm. At 300kHz, the thickness resonance and a significant enhancement of the piezoelectric coefficient d_{33} can be seen.

A.2.6 Resonance Spectrum

The resonance can be described by the behavior of a system to oscillate at different amplitudes for different frequencies. Where the oscillating amplitudes become locally and/or globally large, resonance occurs; namely at the resonance frequencies. Even very small driving forces could then lead to resonance catastrophe, because the system stores to much of the vibrational energy. The vibrational intensity I for a specific resonance frequency ω_0 is given through the formula [Hartmann 1998]:

$$I(\omega) \propto \frac{1}{|(1-(\frac{\omega}{\omega_0})^2)|}$$

where ω means the driving frequency. In Fig. A.4 the behavior of a thin polymer film under an external driving voltage is shown as an example for a resonance spectrum.

A.2.7 Signal-to-Noise Ratio

The signal-to-noise ratio (SNR) [Smith 1997, Hartmann 1998, Guillaume 2006] is a measure for the quality of a signal, which is overlayed by noise. It is defined by the ratio of the average power of the signal to that of the noise source:

$$\mathrm{SNR} = \frac{P_S}{P_N}$$

while the power is defined via the effective voltage being the root mean square of the time varying value:

$$\mathrm{SNR}_{\mathrm{dB}} = 10\ \lg\left(\frac{P_S}{P_N}\right) = 10\ \lg\left(\frac{u^2_{\mathrm{eff},S}}{u^2_{\mathrm{eff},N}}\right).$$

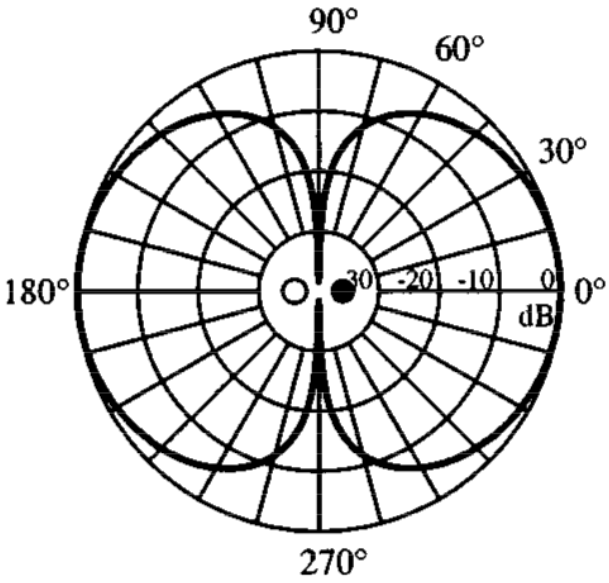

Figure A.5: Figure taken from [Russell 1998]. Radiation characteristics of an acoustic dipole at 250 Hz.

Moreover, one can define the SNR in [dB] by:

$$\mathrm{SNR}_{\mathrm{dB}} = 20 \ \lg\left(\frac{\mathrm{Var(Signal)}}{\mathrm{Var(Noise)}}\right)$$

Simply by the determination of the variances (the measure of the average distance of an random value to its expected value), the SNR [dB] can also be reconstructed. With the help of these equations, the SNR of the specially prepared piezopolymer can be determined with $\mathrm{SNR}_{\mathrm{dB}} = 78\mathrm{dB}$ measured at the first harmonic of the multichord.

A.2.8 Acoustic Dipole Radiation

An acoustic dipole can be associated as two monopole sources [Russell 1998], which have an opposite phase and equal strength. The dipole radiates not homogeneously. There is a specific directivity (see Fig. A.5), which is also frequency-dependent compared to the monopole [Russell 1998].

A.2.9 Impedance

Generally, two kinds of impedances can be distinguished: the electrical and the acoustical or rather the specific mechanical impedance.

A.2.9.1 Acoustic Impedance

The acoustical impedance [Morse 1936, Veit 1996, Möser 2010, Bucur 2006, Giordano 1998a] in the free sound field is the multiplication of density ϱ and longitudinal velocity v_c and describes the resistance against the propagating sound wave:

$$Z_a = \varrho \cdot v_c \tag{A.6}$$

Within a material, the acoustical impedance can be represented by the material constants: sound-wave pressure p and sound-wave flux q:

$$Z_a = \frac{p}{q}$$

A.2.9.2 Electrical Impedance

Since the sound vibrations in this investigation are always electrically recorded, it is worth to take a look at the electrical impedance z_e [Alexander 2006], because every change of the conducting material will change z_e. This will result in additional reflections at the junctions, which will be present in the frequency spectrum. But these device effects can be deconvolved from the measured signal in order to have a 'device function'-free spectrum.

The electrical impedance z_e, which is also called the alternating current (AC) resistance, is the quotient of the complex alternating voltage u and the complex alternating current i:

$$z_e = \frac{u}{i}.$$

But z_e can also be expressed by the active resistance R and the reactance X:

$$z_e = R + \mathrm{i} \cdot X.$$

with i as the imaginary unit. X is dependent on the frequency: either it runs ahead (concerning the inductivity of a coil) or behind (concerning the capacitance of a condensor) a signal. Therefore, in the present case, where the measurements were performed with a cable (with a condensor setup), X is running behind the signal and can be expressed with:

$$Z = |Z| \cdot \exp^{\mathrm{i}\varphi}.$$

ϕ is here the phase angle. The absolute value of the apparent impedance Z is given by the effective values of the voltage and the current:

$$Z = \frac{U_{eff}}{I_{eff}}$$

The ideal setup for electrical recordings to avoid reflections at the transition points can be summarized with: input resistance R_i equals output resistance R_o.

A.2.10 Sound Pressure Quantity

An average human ear can withstand a sound pressure of $\sim$ 20Pa before it gets damaged [Veit 1996], which is about 10^6 times the threshold of human hearing ($p_0 = 2 \cdot 10^{-5}$Pa at 1000Hz). Due to its wide range, the sound pressure L_p is commonly given on logarithmic scale [Veit 1996, Möser 2007]:

$$L_p \stackrel{\text{def}}{=} 20 \cdot \log_{10} \left(\frac{\tilde{p}}{p_0} \right) [\text{dB}] \tag{A.7}$$

$\tilde{p}$ represents the effective sound pressure and is given through the maximum value of the sound pressure: $\Rightarrow \tilde{p} = p_{\max}/\sqrt{2}$. For example, a normal conversation at a distance of 1m has a sound pressure of about $L_p = 1\,\mu$bar $\hat{=}$ 74 dB.
Giving the sound-wave energy density $\rho(x,t)$:

$$\rho(x,t) \stackrel{\text{def}}{=} \frac{\langle \kappa \rangle}{2} \left(\frac{\partial}{\partial t} \mathrm{d}(x,t) \right)^2 + \frac{1}{2\langle \kappa \rangle} (\mathrm{div}(\mathrm{d}(x,t)))^2 \tag{A.8}$$

and the sound intensity or the energy flux density of the sound wave $\jmath(x,t)$:

$$\jmath(x,t) \stackrel{\text{def}}{=} p(x,t) u(x,t) \tag{A.9}$$

the continuity equation is then given by:

$$\frac{\partial}{\partial t} \rho + \mathrm{div} \jmath = 0 \tag{A.10}$$

Appendix B

Curriculum Vitæ

Personal Data

Name:	Marcel Kappel
Birth:	02.12.1981 in Nauen
Address:	An der Petersburg 8, 49082 Osnabrück
Email:	makappel@gmx.de

Education

Aug. 2008 – present	Member of Research Staff; PhD-Thesis at the ACMP Group (University Potsdam) under the Supervision of Prof. R. Gerhard
Oct. 2006 – Nov. 2007	Diploma Thesis at the Astrophysical Institute of Potsdam
Oct. 2002 – Mar. 2008	Study of Physics at the University of Potsdam
July 2001 – Apr. 2002	Civil Service at the Office for Environment in Ketzin
June 2001	'Abitur' at the 'Goethe-Gymnasium' in Nauen
June 1998	'Mittlere Reife' at the Comprehensive School in Ketzin

Employment & Practical Experience

2009 – 2012	4 Contributions at the Long Night of Science
2008 – 2011	5 Semester of weekly Tutorials for Experimental Physics
2008 – 2010	Participation in the Project: SEPHA – Didaktische Konzepte für die strukturierte Studieneingangsphase
March – August 2006	Student Assistant for the Maintaining of a Data Reduction Pipeline

Publications

2010	M. Kappel, M. Abel und R. Gerhard *'Sound Generation in a Piano: Multichannel Measurements'* Conference Proceedings 'DAGA 2010'
2010	M. Kappel, M. Abel und R. Gerhard *'Comparison of Measurements on a Simplified Piano Model with a Condenser Microphone and a Piezoelectric Polymer Sensor'* Conference Proceedings 'DAGA 2011'
2011	M. Kappel, M. Abel und R. Gerhard *'Characterization and Calibration of Piezoelectric Polymer: in-situ Measurements of Body Vibrations'* Rev. Sci. Instrum. **82**, 075110 (2011)
2012	Co-Author of a Chapter in: Kossak, Peter; Lehmann, Uta; Ludwig, Joachim (Ed.) *'Die Studieneingangsphase - Analyse, Gestaltung und Entwicklung.'* (**ISBN-10: 3937026770**)

Conference Contributions

2010	**DAGA 2010 Berlin**, Poster: *'Sound Generation in a Piano: Multichannel Measurements'*
2011	**DPG 2011 Dresden**, Poster: *'Acoustic Calibration and Characterization of PVDF: in-situ Measurements of Body Vibrations'*
2011	**DAGA 2011 Düsseldorf**, Oral Prasentation: *'Scattering Effects: Ribs on Soundboard'*

Bibliography

[Alexander 2006] C. Alexander and M. Sadiku. Fundamentals of electric circuits. McGraw-Hill; 3. revised edition, 2006.

[Altafim 2009] R. A. P. Altafim, X.Qiu, W. Wirges, R. Gerhard, R. A. C. Altafim, H. C. Basso, W. Jenninger and J. Wagner. *Template-based fluoroethylenepropylene piezoelectrets with tubular channels for transducer applications.* J. Appl. Phys, vol. 106, 2009.

[Ashcroft 1976] N. W. Ashcroft and N. D. Mermin. Solid state physics. Brooks Cole, 1976.

[Askenfelt 1993] A. Askenfelt and E. V. Jansson. *From touch to string vibrations. I to III.* J. Acoust. Soc. Am., 1990 –1993.

[Ballou 2009] G. Ballou. Electroacoustic devices: Microphones and loudspeakers. Focal Press, 2009.

[Bauer 2004] S. Bauer, R. Gerhard-Multhaupt and G. M. Sessler. *Ferroelectrets: Soft Electroactive Foams for Transducers.* Physics Today, vol. 57 (2), pages 37–43, 2004.

[Bayer 1993] G. Bayer and T. Niederdränk. *Weak localization of acoustic waves in strongly scattering media.* Phys. Rev. Lett., vol. 70, pages 3884–3887, 1993.

[Bechstein 2005] C. Bechstein. The world of pianos - fascination with an instrument. Nicolai-Verlag, 2005.

[Bensa 2003] J. Bensa, S. Bilbao, R. Kronland-Martinet and J. O. Smith. *The simulation of piano string vibration: From physical models to finite difference schemes and digital waveguides.* J. Acoust. Soc. Am., vol. 114, pages 1095–1107, aug 2003.

[Bensa 2005] J. Bensa, O. Gipouloux and R. Kronland-Martinet. *Parameter fitting for piano sound synthesis by physical modeling.* J. Acoust. Soc. Am., vol. 118, pages 495–504, jul 2005.

[Bissinger 2008] G. Bissinger. *Structural acoustics of good and bad violins.* J. Acoust. Soc. Am., vol. 124, pages 1764–1773, 2008.

[Bork 1993] I. Bork. *Abstrahlung des Anschlaggeräuschs beim Flügel.* Bericht der 17. Tonmeistertagungen, pages 751–764, 1993.

[Bucur 2006] V. Bucur. Acoustics of wood. Springer, 2006.

[Chaigne 1994a] A. Chaigne and A. Askenfelt. *Numerical simulations of piano strings. I. A physical model for a struck string using finite difference methods*. J. Acoust. Soc. Am., vol. 95, pages 1112–1118, feb 1994.

[Chaigne 1994b] A. Chaigne and A. Askenfelt. *Numerical simulations of piano strings. I and II*. J. Acoust. Soc. Am., 1994.

[Chaigne 1994c] A. Chaigne and A. Askenfelt. *Numerical simulations of piano strings. II. Comparisons with measurements and systematic exploration of some hammer-string parameters*. J. Acoust. Soc. Am., vol. 95, pages 1631–1640, mar 1994.

[Chaigne 2011] A. Chaigne, R. Vuillez and R. Viggiano. *Influence of ribs on the radiation of a piano soundboard*. In Proceedings: 161st Meeting: Acoustical Society of America, Aspen, USA, 2011.

[Condat 1986] C. A. Condat and T. R. Kirkpatrick. *Localization and resonant transmission of third-sound waves on a random substrate*. Phys. Rev. B, vol. 33, pages 3102 – 3114, 1986.

[Conklin Jr. 1990] H. A. Conklin Jr., A. Askenfelt, E. Janson, D. E. Hall, G. Weinreich and K. Wogram. *Five lectures on the acoustics of the piano*, 1990. Royal Swedish Academy of Music *ISBN-10: 9185428620*.

[Conklin Jr. 1996a] H. A. Conklin Jr. *Design and tone in the mechanoacoustic piano. Part I. Piano hammers and tonal effects*. J. Acoust. Soc. Am., vol. 99, pages 3286–3296, jun 1996.

[Conklin Jr. 1996b] H. A. Conklin Jr. *Design and tone in the mechanoacoustic piano. Part I to III*. J. Acoust. Soc. Am., 1996.

[Conklin Jr. 1996c] H. A. Conklin Jr. *Design and tone in the mechanoacoustic piano. Part II. Piano structure*. J. Acoust. Soc. Am., vol. 100, pages 695–708, aug 1996.

[Conklin Jr. 1996d] H. A. Conklin Jr. *Design and tone in the mechanoacoustic piano. Part III. Piano strings and scale design*. J. Acoust. Soc. Am., vol. 100, pages 1286–1298, sep 1996.

[Cooley 1965] J. W. Cooley and J. W. Tukey. *An algorithm for the machine calculation of complex Fourier series*. Math. Comput., vol. 19, no. 90, pages 297 – 301, 1965.

[Crisanti 1993] A. Crisanti, G. Paladin and A. Vulpiani. Products of random matrices in statistical physics, pages pp. 87–115. Springer Series in Solid-State Sciences, 1993.

[Curie 1880] J. Curie and P. Curie. *Développement par compression de l'électricité polaire dans les cristaux hémièdres à faces inclinées*. Bull. Soc. Min. France, pages 90 – 93, 1880.

[Das-Gupta 1991] D. K. Das-Gupta. *Pyroelectricity in Polymers*. Ferroelectrics, vol. 118, pages 165 – 189, 1991.

[Dickens 1992] B. Dickens, E. Balizer, A. S. DeReggi and S. C. Roth. *Hysteresis measurements of remanent polarization and coercive field in polymers*. J. Appl. Phys., vol. 72, pages 4258 – 4264, 1992.

[DIN e.V. 2005a] DIN e.V. Akustik - Messung der Schalldämmung in Gebäuden und von Bauteilen - Teil 1 (DIN EN ISO 140-1). Beuth Verlag GmbH, 2005.

[DIN e.V. 2005b] DIN e.V. Akustik - Messung der Schalldämmung in Gebäuden und von Bauteilen - Teil 3 (DIN EN ISO 140-3). Beuth Verlag GmbH, 2005.

[DIN e.V. 2010] DIN e.V. Bestimmung der Schallleistungs- und Schallenergiepegel von Geräuschquellen aus Schalldruckmessungen (DIN EN ISO 3745). Beuth Verlag GmbH, 2010.

[Ducasse 2005] E. Ducasse. *On waveguide modeling of stiff piano strings*. J. Acoust. Soc. Am., vol. 118, pages 1776–1781, sep 2005.

[Eargle 2004] J. Eargle. The microphone book, second edition: From mono to stereo to surround - a guide to microphone design and application. Focal Press, 2004.

[Elejabarrieta 2002] M. J. Elejabarrieta, A. Ezcurra and C. Santamaria. *Coupled modes of the resonance box of the guitar*. J. Acoust. Soc. Am., vol. 111, pages 2283–2292, may 2002.

[Filippi 1999] P. Filippi, D. Habault, J. P. Lefebvre and A.Bergassoli. Acoustics: Basic physics, theory and methods. Academic Press, 1999.

[Fletcher 1993] N. H. Fletcher and T. D. Rossing. The physics of musical instruments. Springer-Verlag, 1993.

[Fletcher 1999] N. H. Fletcher. *The nonlinear physics of musical instruments*. Rep. Prog. Phys., vol. 62, pages 723–764, may 1999.

[Fukada 1950] E. Fukada. *Vibrational study of the wood used for the sound boards of pianos*. Nature, vol. 166, pages 772 – 773, 1950.

[Furukawa 1981] T. Furukawa, G. E. Johnson, H. E. Bair, Y. Tajitsu, A. Chiba and E. Fukada. *Ferroelectric Phase Transition in a Copolymer of Vinylidene Fluoride and Trifluoroethylene*. Ferroelectrics, vol. 32, pages 61 – 67, 1981.

[Furukawa 2001] T. Furukawa and Y. Takahashi. *Ferroelectric and antiferroelectric transitions in random copolymers of vinylidene fluoride and trifluoroethylene*. Ferroelectrics, vol. 264, page 1739, 2001.

[Giordano 1996] N. Giordano and A. J. Korty. *Motion of a piano string: Longitudinal vibrations and the role of the bridge*. J. Acoust. Soc. Am., vol. 100, pages 3899–3908, dec 1996.

[Giordano 1997] N. Giordano. *Simple model of a piano soundboard*. J. Acoust. Soc. Am., vol. 102, pages 1159–1168, aug 1997.

[Giordano 1998a] N. Giordano. *Mechanical impedance of a piano soundboard*. J. Acoust. Soc. Am., vol. 103, pages 2128–2133, apr 1998.

[Giordano 1998b] N. Giordano, H. Gould and J. Tobochnik. *The physics of vibrating strings*. Comput. Phys., vol. 12, pages 138–145, mar 1998.

[Giordano 2006] B. Giordano and S. McAdams. *Material identification of real impact sounds: Effects of size variation in steel, glass, wood and plexiglass plates*. J. Acoust. Soc. Am., vol. 119, pages 1171–1181, feb 2006.

[Goldstein 1980] H. Goldstein. Classical mechanics. Addison-Wesley Publishing Company, 1980.

[Gren 2006] P. Gren, K. Tatar, J. Granström, N. E. Molin and E. V. Jansson. *Laser vibrometry measurements of vibration and sound fields of a bowed violin*. Measur. Sci. Technol., vol. 17, pages 635–644, apr 2006.

[Guillaume 2006] P. Guillaume. Music and acoustics. ISTE Ltd, London, 2006.

[Hahn 1985] B. Hahn and J. Wendorff. *Dielectric relaxation of the crystal-amorphous interphase in poly (vinylidene fluoride) and its blends with poly (methyl methacrylate).* Macromolecules, vol. 18, pages 718 – 721, 1985.

[Hall 1992a] D. E. Hall. *Piano string excitation I to VI (series).* J. Acoust. Soc. Am., 1987-1992.

[Hall 1992b] D. E. Hall. *Piano string excitation. VI: Nonlinear modeling.* J. Acoust. Soc. Am., vol. 92, pages 95–105, jul 1992.

[Harrison 2001] J. S. Harrison and Z. Ounaies. *Piezoelectric Polymers.* ICASE Report, no. 2001-43, 2001.

[Hartmann 1998] W. Hartmann. Signals, sound, and sensation. Springer, 1998.

[Hayashi 1999] E. Hayashi, M. Yamane and H. Mori. *Behavior of piano-action in a grand piano. I. Analysis of the motion of the hammer prior to string contact.* J. Acoust. Soc. Am., vol. 105, pages 3534–3544, jun 1999.

[Hillenbrand 2004] J. Hillenbrand and G. M. Sessler. *Quasistatic and Dynamic Piezoelectric Coefficients of Polymer Foams and Polymer Film Systems.* IEEE Transactions on Dielectrics and Electrical Insulation, vol. 11, pages 72 – 79, 2004.

[Kappel 2010] M. Kappel, M. Abel and R. Gerhard. *The effect of Mounted Ribs on the Radiation of a Soundboard.* arXiv:1011.5372v1, 2010.

[Kappel 2011] M. Kappel, M. Abel and R. Gerhard. *Characterization and calibration of piezoelectric polymers: In situ measurements of body vibrations.* Rev. Sci. Instrum., vol. 82, page 075110, 2011.

[Kawai 1969] H. Kawai. *The piezoelectricity of polyvinylidene fluoride.* Jpn. J. Appl. Phys., vol. 8, pages 975–976, 1969.

[Kittel 1953] C. Kittel. Introduction to solid state physics. Wiley, 1953.

[Komano 1994] T. Komano and T. Kunimoto. *Electronic musical instrument which simulates physical interaction of piano string and hammer.* J. Acoust. Soc. Am., vol. 96, page 621, jul 1994.

[Kremmer 2007] A. Kremmer. Untersuchungen der Struktur von Polyamid 11-Filmen und ihres Einflusses auf deren piezo- und ferroelektrischen Eigenschaften, pages 16 – 23. PhD thesis (in german), 2007.

[Kressmann 2001] R. Kressmann. *Linear and Nonlinear Piezoelectric Response of Charged Cellular Polypropylene*. J. Acoust. Soc. Am., vol. 104, pages 3489 – 3496, 2001.

[Kulek 2002] J. Kulek, Cz. Pawlaczyk and E. Markiewicz. *Influence of poling and ageing on high-frequency dielectric and piezoelectric response of PVDF-type polymer foils*. Journal of Electrostatics, vol. 56, pages 135 – 141, 2002.

[Künstler 2000] W. Künstler, Z. Xia, T. Weinhold, A. Pucher and R. Gerhard-Multhaupt. *Piezoelectricity of porous polytetrafluoroethylene single- and multiple-film electrets containing high charge densities of both polarities*. Appl. Phys. A, vol. 70, no. 1, pages 5 – 8, 2000.

[Landolt 2006] H. Landolt and R. Börnstein. Ferroelectrics and related substances. Springer, 2006.

[Mamou-Mani 2008] A. Mamou-Mani, J. Frelat and C. Besnainou. *Numerical simulation of a piano soundboard under downbearing*. J. Acoust. Soc. Am., vol. 123, pages 2401–2406, 2008.

[Marquardt 1963] D. W. Marquardt. *An algorithm for least squares estimation of nonlinear parameters*. SIAM J. Appl. Math., vol. 11, pages 431 – 441, 1963.

[Mellinger 2003] A. Mellinger. *Dielectric Resonance Spectroscopy: a Versatile Tool in the Quest for Better Piezoelectric Polymers*. IEEE Transactions on Dielectrics and Electrical Insulation, vol. 10, pages 842 – 861, 2003.

[Moore 2006] T. R. Moore and S. A. Zietlow. *Interferometric studies of a piano soundboard*. J. Acoust. Soc. Am., vol. 119, pages 1783–1793, 2006.

[Morse 1936] P. M. Morse. Vibration and sound. AIP for ASA, 1936.

[Morse 1987] P. M. Morse and K. U. Ingard. Theoretical acoustics, pages pp. 175–227. Princeton University Press, 1987.

[Möser 2007] M. Möser. Technische Akustik. Springer, 2007.

[Möser 2010] M. Möser and W. Kropp. Körperschall. Springer, 2010.

[MSI 2006] Measurements Specialities, Inc. MSI. *Piezo Film Sensors – Technical Manual*, 2006. http://www.media.mit.edu/resenv/classes/MAS836/Readings/MSI-techman.pdf.

[Newman 1980] B. A. Newman, P. Chen, K. D. Pae and J. I. Scheinbeim. *Piezoelectricity in Nylon-11.* J. Appl. Phys., vol. 51 (10), pages 5161 – 5164, 1980.

[Nix 1986] E. L. Nix and I. M. Ward. *The measurement of the shear piezoelectric coefficients of polyvinylidene fluoride.* Ferroelectrics, vol. 67, pages 137 – 141, 1986.

[Oshiki 1976] M. Oshiki and E. Fukada. *Piezoelectric Effect in Stretched and Polarized Polyvinylidene Fluoride Film.* Jpn. J. Appl. Phys., vol. 15, pages 43 – 52, 1976.

[Parakilas 1999] J. Parakilas. Piano roles: Three hundred years of life with the piano. Yale University Press, 1999.

[Pollens 1995] S. Pollens. The early pianoforte. Cambridge University Press, 1995.

[Pu 2010] J. Pu, X. Yan, Y. Jiang, C. Chang and L. Lin. *Piezoelectric actuation of direct-write electrospun fibers.* Sensors and Actuators A, vol. 164, pages 131 – 136, 2010.

[Rabiner 1975] L. R. Rabiner and B. Gold. Theory and application of digital signal processing. Englewood Cliffs, N.J., Prentice-Hall, Inc., 1975.

[Rodgers 1988] J. L. Rodgers and W. A. Nicewander. *Thirteen ways to look at the correlation coefficient.* Am. Statist., vol. 42, pages 59–66, 1988.

[Rollik 1999] D. Rollik, S. Bauer and R. Gerhard-Multhaupt. *Separate contributions to the pyroelectricity in polyvinylidene fluoride from the amorphous and crystalline phases as well as their interfaces.* J. Appl. Phys., vol. 85, pages 3282 – 3288, 1999.

[Russell 1998] D. A. Russell, J. P. Titlow and Y.-J. Bemmen. *Acoustic monopoles, dipoles, and quadrupoles: An experiment revisited.* Am. J. Phys., vol. 67, pages 660 – 664, 1998.

[Schuck 1943] O. H. Schuck and R. W. Young. *Observations on the Vibrations of Piano Strings.* J. Acoust. Soc. Am., vol. 15, pages 1–11, 1943.

[Sessler 1981] G. M. Sessler. *Piezoelectricity in polyvinylidenefluoride*. J. Acoust. Soc. Am., vol. 70 (6), pages 1596 – 1608, 1981.

[Sessler 1999a] G. M. Sessler and R. Gerhard-Multhaupt. Electrets, Third Edition in two Volumes, 1999.

[Sessler 1999b] G. M. Sessler and R. Gerhard-Multhaupt. Electrets, third edition in two volumes, cap. Laplacian Press, Morgan Hill, CA, 1999.

[Smith 1997] S. W. Smith. *The Scientist and Engineer's Guide to Digital Signal Processing*, 1997. ISBN-10: 0966017633.

[Suzuki 1986] H. Suzuki. *Vibration and sound radiation of a piano soundboard*. J. Acoust. Soc. Am., vol. 80, pages 1573–1582, dec 1986.

[Suzuki 1987] H. Suzuki. *Model analysis of a hammer-string interaction*. J. Acoust. Soc. Am., vol. 82, pages 1145–1151, oct 1987.

[Suzuki 2007] H. Suzuki. *Spectrum analysis and tone quality evaluation of piano sounds with hard and soft touches*. Acoust. Sci. Techn., vol. 28, pages 1–6, 2007.

[Takahashi 1987] Y. Takahashi, M. Iijima, K. Inagawa and A. Itoh. *Synthesis of Aromatic Polyamide Film by Vacuum Deposition Polymerization*. J. Vac. Sci. Technol. A, vol. 5, page 2253, 1987.

[Takahashi 1989] Y. Takahashi, M. Iijima and E. Fukada. *Pyroelectricity in Poled Thin Films of Aromatic Polyurea Prepared by Vapor Deposition Polymerization*. Jpn. J. Appl. Phys., vol. 28, pages L408 – L410, 1989.

[Tanaka 1996] H. Tanaka, K. Mizutani and K. Nagai. *Two-dimensional motion of a single piano string*. J. Acoust. Soc. Am., vol. 100, page 2843, oct 1996.

[Tasaka 1981] S. Tasaka and S. Miyata. *The origin of piezoelectricity in poly(vinylidene fluoride)*. Ferroelectrics, vol. 32, pages 17–23, 1981.

[Tashiro 1981] K. Tashiro, H. Tadokoro and M. Kobayashi. *Structure and piezoelectricity of poly(vinylidene fluoride)*. Ferroelectrics, vol. 32, page 167, 1981.

[The MathWorks, Inc.] The MathWorks, Inc. *MATLAB - The Language Of Technical Computing*.

[Tufillaro 1989] N. B. Tufillaro. *Nonlinear and chaotic string vibrations*. Am. J. Phys., vol. 57, pages 408–414, may 1989.

[Tufillaro 1995] N. B. Tufillaro, P. Wyckoff, R. Brown, T. Schreiber and T. Molteno. *Topological time series analysis of a string experiment and its synchronized model*. Phys. Rev. E, vol. 51, no. 1, pages 164–174, 1995.

[v. Helmholtz 1863] H. v. Helmholtz. Die Lehre von Tonempfindungen als physiologische Grundlage für die Theorie der Musik. Friedrich Vieweg und Sohn, 1863.

[Veit 1996] I. Veit. Technische Akustik. Vogel Fachbuch; Kamprath-Reihe, 1996.

[Vinogradov 2002] A. Vinogradov and M. Schwartz. Piezoelectricity in polymers, pages 780 – 792. Encyclopedia of Smart Materials, Volumes 1-2. John Wiley and Sons, 2002.

[Vyasarayani 2009] C. P. Vyasarayani, S. Birkett and J. McPhee. *Modeling the dynamics of a compliant piano action mechanism impacting an elastic stiff string*. J. Acoust. Soc. Am., vol. 125, pages 4034–4042, 2009.

[Wada 1981] Y. Wada and R. Hayakawa. *A Model of Piezo- and Pyroelectricity of Poly(Vinylidene Fluoride) Electret*. Ferroelectrics, vol. 32, pages 115 – 118, 1981.

[Weinreich 1977] G. Weinreich. *Coupled piano strings*. J. Acoust. Soc. Am., vol. 62, pages 1474–1484, dec 1977.

[Wogram 1980] K. Wogram. *Acoustical Research on Pianos: Vibrational Characteristics of the Soundboard*. Das Musikinstrument, vol. 24, pages 694–702, 1980.

[Wong 1997] G. S. K. Wong and T. F. W. Embleton. AIP handbook of condenser microphones: Theory, calibration and measurements. AIP Series in Modern Acoustics and Signal Processing. Springer, Berlin, 1997.

[Yoshikawa 2007] S. Yoshikawa. *Acoustical classification of woods for string instruments*. J. Acoust. Soc. Am., vol. 122, pages 568–573, 2007.

[Young 1952] R. W. Young. *Inharmonicity of Plain Wire Piano Strings*. J. Acoust. Soc. Am., vol. 24, pages 267–273, 1952.

[Zhang 2002] Q. M. Zhang, V. Bharti, G. Kavarnos and M. Schwartz. Poly(vinylidene fluoride) (PVDF) and its copolymers, pages 807–825.

Encyclopedia of Smart Materials, Volumes 1-2. John Wiley and Sons, 2002.

[Ziman 1972] J. Ziman. Principles of the theory of solids. Cambridge University Press, 1972.

List of Figures

Selbstständigkeitserklärung

Hiermit erkläre ich an Eides Statt, dass ich die vorliegende Dissertation selbst und ohne unzulässige Hilfe Dritter verfasst, die benutzte Literatur sowie Hilfsmittel vollständig erwähnt habe und die Dissertation noch von keiner anderen Fakultät abgelehnt worden ist.

Marcel Kappel